UNIVERSITÀ DEGLI STUDI "ROMA TRE"

DIPARTIMENTO DI MATEMATICA E FISICA
Scuola dottorale in Matematica e Fisica - XXX Ciclo
Tesi di Dottorato in Fisica

Comptonization mechanisms in hot coronae in AGN. The *NuSTAR* view.

A thesis submitted for the degree of

Doctor of Phylosophy

Author:	Dr. Alessia Tortosa
Supervisor:	Prof. Giorgio Matt
Thesis coordinator:	Prof. Giuseppe De Grassi

A. A. 2016 - 2017

A long time ago in a galaxy far,
far away....

Introduction

> "Limitless undying love which shines around me like a million suns it calls me on and on across the universe."
>
> John Lennon

The local universe is made up mainly of galaxies. The radiation emitted by a galaxy can be considered, in first approximation, as the sum of the radiation of their stars. However, for a small percentage of galaxies, called active galaxies, or Active Galactic Nuclei (AGN for short), this is not true. AGN emit through all the electromagnetic spectrum. Much of the energy output of AGN has non-stellar origin, with many AGN being strong emitters of X-rays, radio and ultraviolet radiation, as well as optical radiation. The radiation from an AGN is believed to be a result of accretion of matter onto a supermassive black hole ($10^6 - 10^9$ solar masses) at the center of its host galaxy. The accretion of matter occurs through an accretion disc in which gravitational energy is partially transformed into radiation.

The spectral energy distribution (SED) of active galactic nuclei is very broad and ranges from the radio band up to X-rays and gamma-rays. The SED of an AGN can be decomposed into four main components: the primary emission in the optical/UV band; the infrared continuum; the high-energy continuum; the radio emission, which can be relatively strong (radio-loud AGN) or weak (radio-quiet AGN). In addition to the broad, non-stellar energy distribution, AGN also exhibit strong emission lines in their spectra.

The primary X-ray emission in AGN is believed to be produced in the so-called corona, a compact region located close to the supermassive black hole and composed by a plasma possibly in thermal equilibrium. The accretion disc produces optical/UV seed photons in a quasi-black body spectral shape; in the corona these photons are up scattered to the X-ray band due to the inverse Compton effect. Since this effect cools the corona, there must be some other mechanism that heats the corona, in order to maintain a high enough temperature. This energy source could be the dissipation of magnetic flux through reconnection.

The inverse Compton scattering by the hot electrons of the UV seed photons emitted by the accretion disc produces a X-ray power law spectrum, extending to energies determined by the coronal electrons temperature, with spectral index that typically t ranges from 1.5 to 2.0. The power law often shows a cutoff at high energies, around 100-200 keV. Both the energy of the cutoff and the photon index are related to the temperature and the optical depth of the corona. Comptonization models imply that the cutoffs energies are typically 2-3 times the temperature of the corona.

The present work fits in this complex scenario. It will be based mainly on the study of the X-ray broad-band spectrum of AGN, to constrain the coronal parameters and start to look for correlations between these parameters and other physical parameters, such as the geometry and the position, with the aim of better understanding the complex environment present in AGNs. In fact the geometry of the disc/corona system is still unknown, and we also still lack good constraints on the coronal temperature and optical depth for most sources. The size and the location of the corona is still matter of debate. There are open questions like: is the corona spherical, or a slab, or it has a more complex shape? Is it compact, as assumed in the lamp-post geometry, or is it extended? Is the corona a continuous or a patchy medium made up of several blobs?

To answer the questions raised above we need to study the broad-band X-ray spectrum and variability of AGN in details, on adequate time-scales in order to model all the spectral components and to investigate the shape of the nuclear continuum. It is very important to disentangle all the complex spectral features in this energy range, to remove all the degeneracies between the primary continuum features and other physical observables in order to constrain the coronal parameters and to have an overview of the physics and the structure of the hot corona.

In the past, several cutoff energies in nearby Seyfert galaxies have been measured with hard X-ray satellites, such as *BeppoSAX* (Dadina 2007, Perola et al. 2002) and *INTEGRAL* (Panessa et al. 2011; de Rosa et al. 2012; Molina et al. 2013). These measurements ranged between 50 and 300 keV but the lack of focusing instruments at high energies resulted in large uncertainties and degeneracies between the cutoff energies and other physical observables (in particular the slope of the primary power law and the amount of radiation Compton scattered by circumnuclear matter). *NuSTAR* (Harrison et al. 2013, see also Section 3.4) has been an observational breakthrough in X-ray astronomy with its unprecedented sensitivity at high energies, operating in the 3-79 keV energy range. Simultaneous observations with other X-ray observatories operating below 10 keV, such as *XMM-Newton, Suzaku* and *Swift* allowed to measure cutoff energies with great accuracy in a number of sources.

This work is based both on new observations of *NuSTAR, XMM-Newton* and *Swift* X-ray satellites and on archival data. The detailed analysis of single sources allows to build and constrain physical models while the analysis of a large sample gives us insights into the average properties of AGN.

The thesis is structured as follows:

- Chapter 1 describes the basic properties of Active Galactic Nuclei, their physics and their classification. The structure of AGN, the "Unification Model" and their Spectral Energy Distribution will be discussed.

- Chapter 2 describes the X-ray properties of Active Galactic Nuclei, the physical processes that generate this emission and the spectral shape of the X-ray emission. We start with the description of the different processes which lead to the production of X-rays in AGN, forming the characteristic spectral shapes, and then we describe the X-ray spectrum of Active Galactic Nuclei and the structure of the Comptonizing corona.

- In Chapter 3 we briefly discuss current hard X-ray telescopes, showing the developments in technology and giving an overview of the observatories which are used in this thesis: *XMM*-Newton, *Swift* and *NuSTAR*.

- In Chapter 4 we present the analysis of the *NuSTAR* and *XMM-Newton* spectra of GRS 1734-292, which is a Seyfert 1 galaxy located near the Galactic plane. It shows one of the lowest high energy cutoff measurements so far by *NuSTAR* (the results of this study have been reported in Tortosa et al. 2017).

- Chapter 5 reports the analysis of two bright Seyfert 1: MCG +8-11-11 and NGC 6814. They show very similar coronal properties even if they had different properties overall (black hole masses, luminosity and Eddington ratios). The result of this study will be reported in Tortosa et al. (2018).

- In Chapter 6 we discuss an ongoing project based on the analysis of a small catalog of AGN we build up choosing the unobscured nearby, non-jetted, Seyfert galaxies that have been observed by *NuSTAR* (often in coordination with *XMM-Newton*, *Suzaku* or *Swift*). We compile the literature values of the coronal parameters of this sample of AGNs to look for correlations between spectral parameters, such as the photon index and the cutoff energy, with other physical parameters, e.g. the black hole mass or the Eddington ratio. The results of this study will be reported in Tortosa et al. (2017, in prep).

- Chapter 7 draws some conclusions on the works that have been presented throughout this thesis.

- Appendix A describes the fitting package XSPEC, the tool we used in this work for the spectral analysis of *XMM-Newton*, *Swift* and *NuSTAR* spectra.

- Appendix B describes the processing procedure applied for the observatories which are used in this thesis: *XMM*-Newton, *Swift/XRT* and *NuSTAR*.

Ringraziamenti

Sono decisamente molte le persone che vanno ringraziate, senza le quali il mio percorso di dottorato probabimente non sarebbe stato lo stesso, e la mia tesi non avrebbe potuto assumere la sua forma.

Inizio con il ringraziare il mio relatore, il Prof. Giorgio Matt che mi ha accompagnata e guidata in questo lungo percorso e senza il quale questa tesi non esisterebbe. Grazie per avermi dato la possibilità di sfruttare tante opportunità di crescita, per avermi insegnato il senso della ricerca scientifica e per avermi trasmesso l'entusiasmo per qusta. Ringrazio anche il Prof. Stefano Bianchi e il Dr. Andrea Marinucci che con molta pazienza mi hanno offerto la loro guida, la loro esperienza e il loro aiuto durante questo percorso. Desidero ringraziare anche i *referees*, il Prof. Giovanni Miniutti e a Dr.ssa Barbara De Marco che hanno letto con molta attenzione la tesi e mi hanno dato molti utili consigli per migliorarla.

Un enorme ringraziamento va alla mia famiglia, che non ha mai smesso di sostenermi, di supportarmi e sopportarmi sopratutto nei periodi più difficili, e ce ne sono stati tanti. Grazie a loro ho sempre ritrovato la forza di andare avanti nella realizzazione di questo persorso, che più che un percorso per me è un sogno. Il sogno di una bambina che prima ancora di imparare a scrivere e leggere desidera conoscere l'Universo e i suoi misteri. Grazie perchè, anche se non sempre avete condiviso le mie scelte non avete mai smesso di darmi la possibilità di agire con la mia testa e mi avete permesso di arrivare fin quì. Se sono chi sono è merito vostro.

Desidero ringraziare i miei compagni di dottorato che hanno reso questo percorso pieno di momenti gioiosi, e tutte le fantastiche persone che questa esperienza mi ha portato a conoscere, e sono veramente tante, una in particolare si è insediata non solo nella mia vita ma anche nel mio cuore. Grazie per tutti i momenti più o meno brevi, condivisi insieme, li ricorderò sempre con affetto.

Grazie ai miei amici che ci sono sempre stati, e a quelli che sono usciti dalla mia vita, perchè mi hanno fatto capire l'importanza di chi resta e ti sostiene sempre. Occupate tutti una parte del mio cuore, chi più grande e chi più piccola. Alcuni di voi sono parte integrante della mia famiglia, e a loro va il ringraziamento più sincero, perchè nonostante gli impegni e la distanza, avete sempre fatto sentire la vistra presenza e il vostro sostegno, e grazie a voi sono riucita nella mia piccola grande impresa.

Ma il grazie più grande va a me stessa, per non aver mollato mai, per essermi sempre rialzata dopo ogni caduta, e ce ne sono state tante. Per il coraggio di rimettere insieme ogni volta i pezzi rotti e andare avanti, con molta paura ma anche con molta determi-

nazione, la determinazione che mi ha sempre contraddistinta e che ringrazio di non aver mai perso nonostante le difficoltà. Voglio dire alla me del futuro che si ritroverà in situazioni difficili, di ricordarsi che ne abbiamo superate di cime, e nulla può fermarci. A me stessa, e a tutti quelli come me che si trovano a inseguire un sogno tra mille difficoltà, e che a volte non si ritengono all'altezza, voglio dedicare questo pensiero:
Quando stai per mollare, fermati un attimo e pensa al motivo per il quale hai resistito fino ad allora. Pensa alla meta, non a quanto sia lungo il tragitto. Rimboccati le maniche e non aver paura della fatica. Guardati allo specchio e riconosci quel sognatore che ti sta di fronte. Lotta e combatti. E quando ciò che desideri sarà tuo, porta una mano al cuore e sentirai in ogni singolo battito, l'eco di ognuno dei passi che hai compiuto. E se avrai qualche cicatrice non preoccuparti, non c'è vittoria senza una ferita di guerra, non c'è arcobaleno senza la pioggia!
Infine, vorrei dedicare questa tesi alle persone che più di ogni altra vorrei quì vicino a me, ma che purtroppo la vita mi ha tolto. Siete parte di me, siete sempre presenti nel mio cuore.

Nonna Angela, Nonno Carlo e Elettra, questa tesi è per voi.

Contents

1

ACTIVE GALACTIC NUCLEI

> “Whoever looks into himself as into vast space and carries galaxies in himself, also knows how irregular all galaxies are; they lead into the chaos and labyrinth of existence.”
>
> Friedrich Nietzsche

The name *Active Galactic Nuclei* (AGN) derives from the observational fact that a number of galaxies possess a very high concentration of luminosity in their nucleus, which cannot be directly attributed to stellar activity. The main feature that distinguishes these objects from inactive (normal or regular) galaxies is the presence of supermassive accreting black holes (BHs) in their centers.

This chapter aims to provide a brief introduction to the physics of AGN and their classification.

A more detailed discussion can be found in Peterson 1997 and in Beckmann & Shrader 2013.

1.1. HISTORICAL BACKGROUND

In 1908, astronomers performing optical spectroscopy of nearby galaxies at Lick observatory noticed that one "spiral nebula" (Messier 77: now more commonly referred to as NGC 1068) had an atypical spectrum, showing multiple strong emission lines in addition to the continuum flux and to the absorption lines also seen in other nebulae (Fath, 1909); see Figure 1.1). This was the discovering of the first galaxy hosting an active galactic nucleus (a term which was not coined until decades later). After this first spectrum, more such *emission line galaxies* were discovered. In 1943, when already 12 galaxies of

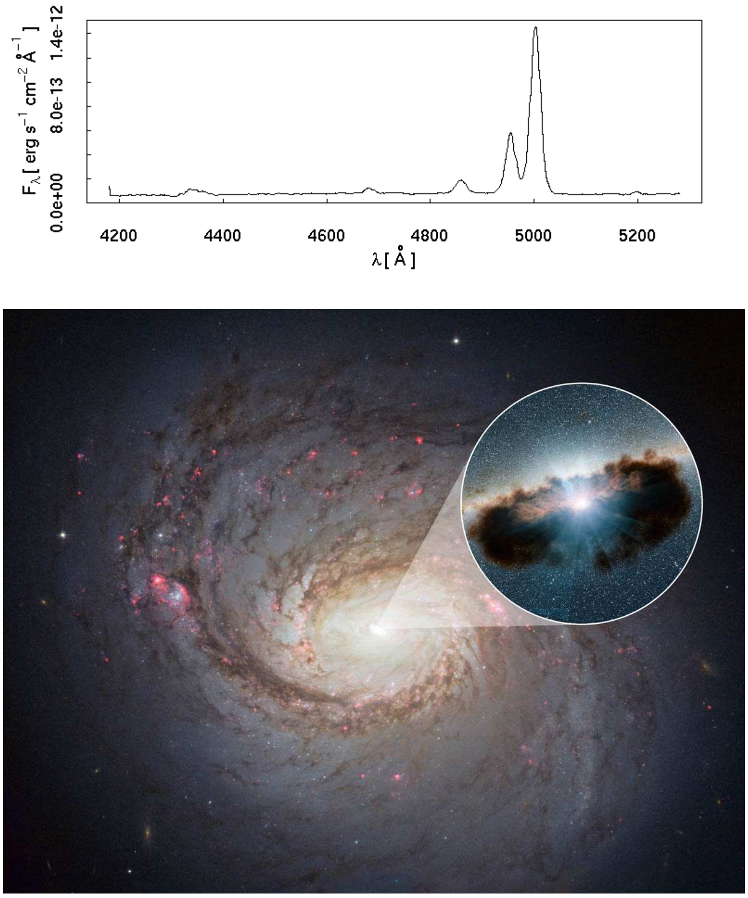

Figure 1.1: Upper panel: optical spectrum of the nuclear region of NGC 1068 (Fath, 1909). Lower panel: NGC 1068 as seen by Hubble Space Telescope (HST) with an artistic impression zoom-in on the central active galactic nucleus. Image credit: NASAESA/JPL-Caltech.

this unusual class of objects had been found, Carl K. Seyfert published his fundamental paper on emission line galaxies (Seyfert, 1943). In this paper, he described the main features of the emission lines. He was also the first to recognize that these galaxies form a special class of objects. He further noted that the emission lines are emitted from a point-like source at the center of the galaxies and that this point-like source contributes a large fraction of the total light emitted by the entire system. From the large width of the emission lines, he deduced a high velocity dispersion in the emitting medium. His work has been rewarded by the fact that we now call these objects *Seyfert galaxies*.

As time went on, many more Seyfert galaxies were identified, and their observational properties became better constrained. They all exhibited extremely bright nuclear regions, with the bright emission limited to a very compact area (within 100 pc of the galaxy center). Resolving this bright nuclear emission spectroscopically and temporally, the Seyferts all showed remarkably strong emission lines, and highly time-variable optical-

UV continua, respectively.

The advances in radio astronomy in the 1950s revealed a new universe of energetic phenomena, and inevitably led to the discovery of quasars. These discoveries demanded the attention of observers and theorists, and AGN have been a subject of intense effort ever since. Only a year after the recognition of the red-shifts of 3C 273 and 3C 48 in 1963, the idea of energy production by accretion onto a black hole was advanced. However, acceptance of this idea came slowly, encouraged by the discovery of black hole X-ray sources in our Galaxy and, more recently, supermassive black holes in the center of the Milky Way and other galaxies. Many questions remain as to the formation and fuelling of the hole, the geometry of the central regions, the detailed emission mechanisms, the production of jets, and other aspects. The study of AGN will remain a vigorous part of astronomy for the foreseeable future.

1.2. OBSERVATIONAL PROPERTIES

AGN are associated with the emission of a huge amount of radiation over the whole electromagnetic spectrum. For instance, their optical-UV luminosity can reach or even exceed that of the integrated stellar population of the host galaxy ($L > 10^{10}$–$10^{11} L_{\odot}$). The enormous power of these objects, emitted from a compact (unresolved) region at the center of the host galaxy (active galaxy), is believed to be released from material accreting onto a supermassive black hole ($M_{BH} = 10^6 - 10^9\ M_{\odot}$), as no other physical phenomenon is able to produce such large and long lasting luminosities over such a wide wavelength range.

The peculiar features usually present in AGN, not necessary at the same time, are:

- It contains a compact nuclear region emitting significantly beyond what is expected from stellar processes typical of the galaxies;
- It shows nuclear broad band emission, over a wide portion of the electromagnetic spectrum;
- Its spectrum contains strong emission lines, mainly found in the infra-red and optical/UV part f the spectrum, with line ratios that are typical of excitation by non stellar radiation field;
- It has an unresolved nucleus with small angular size;
- It shows line and/or continuum variability, especially in the X-rays;
- It has a higher degree of polarization (0.5-2%) with respect to normal galaxies.

The first notably distinct observational characteristic of AGN is the presence of emission lines with widths upwards of thousands of km s^{-1}. Also, the presence of narrow, non variable forbidden emission lines is a distinguishing observational feature of some AGN.

Another observational aspect of AGN is that the continuum spectral distribution is very distinct from an integrated stellar continuum characteristic of normal galaxies. Observationally AGN are very blue.

1.2.1. SPECTRAL ENERGY DISTRIBUTION OF AGN

The emission of AGN cover the entire electromagnetic spectrum ranging from radio emission right up to γ-rays.The *spectral energy distribution* (SED) of AGN is rather complex as the spectra are due to a combination of various physical processes that take place in different regions around the black hole. The emission produced by each process dominates at different wavebands. Although the spectra can be very different from object to object, the main characteristics observed in the SED are common for all AGN, excluding blazars. The SED of AGN can be decomposed into four main components: the primary emission in the optical/UV band; the infra-red continuum, due to thermal emission from the dust heated by the primary UV radiation; the high energy continuum, due to reprocessing of the primary optical/UV emission from hot gas; the radio emission, due to synchrotron radiation, which can be relatively strong (*radio-loud* AGN) or weak (*radio-quiet* AGN).

Figure 1.2 show a schematic representation of an AGN SED from radio frequencies to hard X-rays. Below, the main spectral properties of AGN are described, although we note that not all these properties are observed in all AGN.

RADIO OBSERVATION

It is found that some ($\sim 10\%$) AGN are strong radio sources while other have much weaker emission at radio wavelengths. The usual definition of radio-loudness is that the radio (5 GHz) to optical (B-band) flux ratio is $\gtrsim 10$. Early studies suggested a bi-modal distribution: there appear to be few 'radio-intermediate' AGN, with most being either strongly radio-loud or showing very little in the way of radio emission. This bi-modality is, however, no longer certain; although some surveys do find a definite separation between radio loud and radio quiet objects (e.g., Ivezić et al. 2002), more and more are concluding that there is a continuous transition between the two types, with the apparent dichotomy due to selection effects (Cirasuolo et al. 2003; Hewett et al. 2001; White et al. 2000). The radio spectrum takes the form of a power-law and is thought to be formed through Synchrotron radiation (Jones et al., 1974).

INFRA-RED OBSERVATION

One suggestion for the origin of the IR continuum in AGN is that the IR emission is an extension of the radio power-law, due to the Synchrotron Self-Compton process. However, there is growing evidence that the emission is almost all thermal in nature and is likely to be linked to absorption/emission from dust. There is a bump in each spectrum at wavelengths longer than $\sim 1\mu$, which would coincide with emission from dust at $\lesssim 2000$ K, around the expected temperature for grains in the nuclear regions. Also, the IR continuum seems to vary in the same manner as the optical/UV emission, but with a time delay

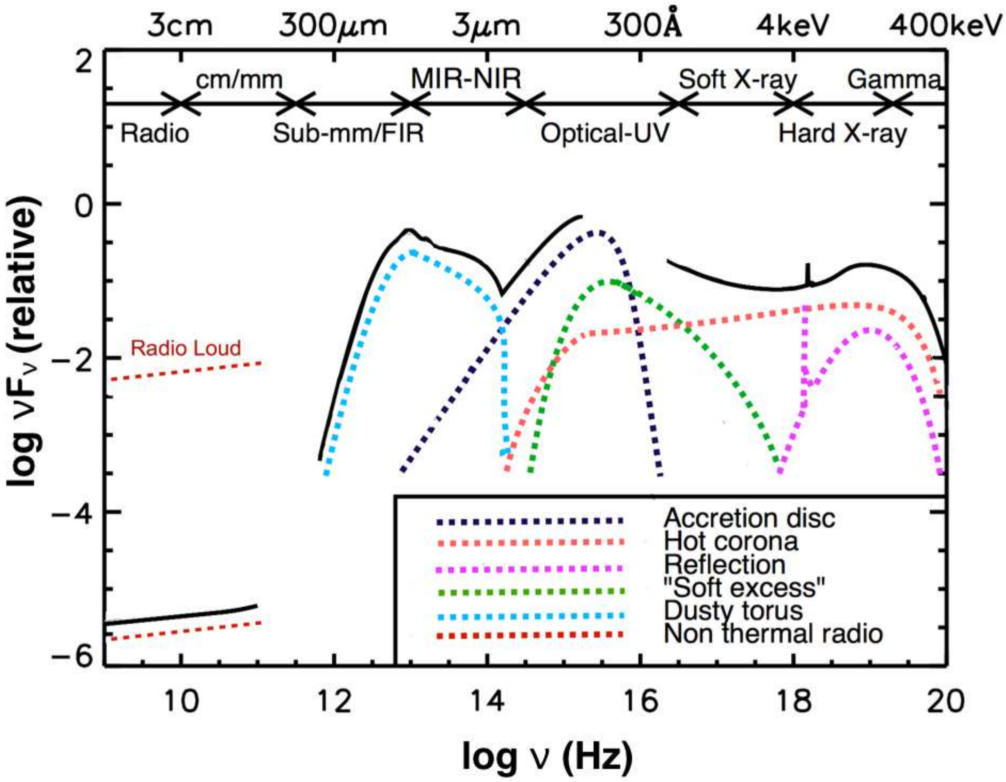

Figure 1.2: A schematic representation of an AGN SED, loosely based on the observed SEDs of radio-quiet quasars (e.g., Elvis et al. (1994)). The black solid curve represents the total SED and the various colored curves (with an arbitrary offset) represent the individual components (see Section 1.2.1). The SED of an AGN in the mm–FIR regime is uncertain; however, it is widely believed to have a minimal contribution (to an overall galaxy SED) compared to star formation, except in the most intrinsically luminous quasars and powerful radio-loud AGN. The primary emission from the AGN accretion disc peaks in the UV region. Radio-loud AGN have radio emission that can be several orders of magnitude higher than radio-quiet AGN (shown with the labeled red).

corresponding to the light travel-time between the central, compact optical/UV-emitting region and the much more distant dust grains (e.g., Clavel et al. 1989).

OPTICAL AND UV OBSERVATIONS

As already said, AGN were first identified at optical wavelengths, with Edward Fath at the Lick Observatory noting that NGC 1068 showed strong emission lines in its spectrum, in 1908. It was until 1943 that Carl Seyfert realized there was a distinct group of such objects with spectra dominated by strong nuclear emission lines. These spectra showed two different types of optical lines, with the permitted emission lines (e.g., the Balmer series of hydrogen) sometimes appearing to be broader. The narrow lines correspond to both permitted (e.g., hydrogen and helium) and forbidden (e.g., carbon, nitrogen, neon, oxygen) transitions. When considering the continuum, rather than the lines, the dominant feature in the optical/UV spectrum is a broad 'hump', known as the Big Blue Bump (BBB).

This is thought to be thermal emission, very likely from the accretion disc surrounding the black hole (e.g., Shields 1978; Malkan & Sargent 1982). The soft X-ray excess, which will be discussed later, has been suggested to be the Comptonised tail of this BBB.

X-RAY AND γ-RAY OBSERVATIONS

At the higher energy end of the EM spectrum, AGN are also observed in the X-ray and, only the radio-loud sources up to γ-ray, with all being luminous X-ray Sources (Elvis et al., 1978). The X-rays may come from the inner regions of the accretion disc, or possibly a hot corona above the accretion disc (Haardt & Maraschi 1991; see Section 2.4), while the very high-energy γ-rays are thought to be produced by inverse-Compton scattering of photons of the highly energetic electrons within the jet (Zhang & Cheng, 1997). Both X-ray and -ray spectra are, to a first approximation, power-law-like (i.e., $F(\nu) \propto \nu^{-\alpha}$; often written in terms of Γ , where $\Gamma = \alpha + 1$; Γ is the photon spectral index, while α is the energy index), although not necessarily with the same spectral index. At higher energies, around 40 MeV or so, most sources show a sharp spectral turnover.

1.2.2. AGN TAXONOMY

The complex structure of the AGN is reflected in their spectral/images, with many different emission/absorption processes acting at the same time. From an observational point of view, the classification of AGN can be rather complex and confusing. Here we report a simple taxonomy of the main types of AGN (e.g. Peterson 1997):

- **Seyfert galaxies:** originally classified by Carl Seyfert (Seyfert, 1943). They are composed of AGN with moderate bolometric luminosity ($L_{bol} \sim 10^{41} - 10^{41}$ erg s^{-1}). These are radio-quiet object and have high central surface brightness, although the host galaxy is still clearly detectable; they tend to be spirals, with massive galactic bulges and the presence of an interstellar medium. Since their original discovery, the classification has evolved such that they are also spectroscopically identifiable by the presence of high-ionisation emission lines. Seyfert galaxies are, themselves, divided into two groups: Seyfert 1s and Seyfert 2s (Sy1s and Sy2s), as was first realized by Khachikian & Weedman 1974.

  – Type-1 Seyfert galaxies: are those with highly ionized, broad permitted lines, together with narrow forbidden lines. The narrow lines come from low-density, low-ionization gas, in the so-called Narrow-Line Region (NLR, see Section 1.3.3), and have a full width at half maximum (FWHM) of a few hundred km s^{-1} (i.e., still broader than those lines observed in non-active galaxies). Because the density in the NLR is low, transitions are not collisionally de-excited, and so the radiative transitions (and, hence, the forbidden lines) are observed. The broad lines have widths Doppler-broadened up to 10^4 km s^{-1}. The Broad Line Region (BLR, see Section 1.3.3) is located closer in to the black hole, shown by both the increased width of the lines, and the higher ionisation state; since only permitted lines are seen, the BLR is thought to be the denser of the two regions, with $n_e \gtrsim 10^9 \mathrm{cm}^{-3}$, compared to $\sim 10^3 - 10^6 \mathrm{cm}^{-3}$ for the NLR. There are certain objects, known as Narrow-Line Seyfert 1 galaxies, which do show the broad lines (c.f. Type-2 galaxies; see below), but they are narrower than in the typical broad-line Seyfert 1s. NLS1s are thought to have high accretion rates and, very probably, small black hole masses; see, e.g., Bian & Zhao 2003a. This will be discussed below.

  - Type-2 Seyfert galaxies: differ from the Type-1 objects by showing only the narrow lines. They have an [O III] λ5007 to Hβ ratio of < 3 (Shuder & Osterbrock, 1981); Seyfert 2s also tend to show weaker [Fe II] (or higher ionisation iron) emission lines than their Seyfert 1 counterparts. The difference between Seyfert 1 and 2 type galaxies, as discussed in Section 1.4, it is likely to be mainly due to an orientation effect.

- **Quasars:** or QSOs (Schmidt, 1963) are the most luminous of the AGN family with a bolometric luminosity $\mathrm{L}_{bol} \sim 10^{44} - 10^{47}$ erg s^{-1}. Their spectra are similar to those of Seyferts. However they are usually found at higher red-shift ($z > 0.1$) and the host galaxy is hardly, if not at all, resolved. They can have a significant radio emission, in which case this radiation can be connected with relativistic jets or extended emission lobes.

- **Radio Galaxies:** are moderate or bright AGN ($\mathrm{L}_{bol} \sim 10^{42} - 10^{46}$ erg s^{-1}) and their peculiarity is their powerful emission in the radio-mm band. Although radio galaxies are considered, in some senses, to be radio-loud Seyferts, they typically occur in elliptical galaxies, rather than spirals. The radio lobes in these galaxies are powered by a jet of particles and emit non-thermal, synchrotron radiation (e.g., Blandford & Rees 1974). They can be classified as Broad Line radio Galaxies (BLRGs) or Narrow Line radio Galaxies (NLRGs) depending on the presence of broad or narrow emission lines in their optical-UV spectra.

- **OVV & Blazars:** the Optically Violent Variables (OVV) show the highest variability among all the AGN, from the radio up to the X-ray bans. Their optical emission is also strongly polarized. Blazars or BL Lacs (named after the first object in the class, identified in the direction of the constellation of Lacerta, the lizard) do not have visible radio lobes and do not show emission/absorption lines. Blazar spectra are purely power-law continua, with no thermal component.

- **LINERs:** Low Ionisation Nuclear Emission-Line Region galaxies are the least luminous of the classifications. They were first identified by Heckman 1980 and are, in fact, very common, possibly existing in nearly half of all spiral galaxies

(Ho et al., 1994). LINERS show only weak nuclear activity, with most of their emission coming from starlight. The emission line spectra indicate the existence of a non-stellar continuum, although this has yet to be observed directly (Netzer 1990). The observational difference, in the optical region, between LINERS and Seyfert 2-type galaxies lies in the relative strength of certain low-ionisation lines, with Heckman's definitions being that the [O II]$\lambda\lambda$ 3727, 3729 lines are stronger than the [O III]λ5007 line, O Iλ 6300/[O III]λ5007 $\lesssim$ 0.33 and [N II]λ 6584/Hα $\gtrsim$ 0.6.

As a final note to this section, Starburst galaxies should be mentioned. These are galaxies in which the star-formation rate is much higher than average. They contain many young stars and are more energetic than normal galaxies, although not as luminous as AGN. They show strong IR emission, due to the heating of dust by UV emission from the young stellar population. Starbursts may be formed through the merger of galaxies. Although there are not AGN as such, much work has been done on the connection between the groups.

1.3. THE STRUCTURE OF AGN

1.3.1. THE CENTRAL ENGINE

The AGN are compact, extremely luminous and often most of them are variable at the shortest observed wavelengths. Thus, a mechanism such as accretion that can provide highly efficient conversion of potential and kinetic energy to radiation is needed, since a large mass provides high persistent Eddington luminosities. AGN must be powered by accretion onto massive black holes at the dynamical center of their host galaxies. The accreting gas surrounding the black hole forms a thin, optically thick disc (Shakura & Sunyaev 1973; Shields 1978; Malkan & Sargent 1982): this material, loosing angular momentum, tends to fall inward and eventually onto the black hole with a mass accretion rate $\dot{M} = dM/dt$. The total energy released by this accretion is given by:

$$L_{acc} = \eta \dot{M} c^2 \tag{1.1}$$

where c is the speed of light in vacuum and η is the efficiency (i.e. mass crossing radius r per unit time). To power a typical AGN requires an accretion rate:

$$\dot{M} = \frac{L}{\eta c^2} \approx 1.8 \times 10^{-3} \left(\frac{L_{44}}{\eta}\right) M_{\odot} yr^{-1} \tag{1.2}$$

where L_{44} is the central source luminosity in unit of 10^{44} erg s^{-1}. The potential energy of a mass m at distance r from a central source of mass M is U = GMm/r, where G is the gravitational constant. The rate at which the potential energy of in-falling material can be converted to radiation is given by:

$$L \approx \frac{dU}{dt} = \frac{GM}{r}\frac{dM}{dt} = \frac{GM\dot{M}}{r} \tag{1.3}$$

The efficiency η depends on the compactness of the accreting object, namely the ratio M/R, as:

$$\eta = \frac{\mathrm{GM}}{Rc^2} = \frac{R_s}{2R} \tag{1.4}$$

where R_s is the Schwarzschild radius, which is the event horizon for a non-rotating black hole. For a black hole with mass $10^8 \mathrm{M}_\odot = \mathrm{M}_8$:

$$R_S = \frac{2\mathrm{GM}}{c^2} \approx 3 \times 10^{13} \mathrm{M}_8 \,\mathrm{cm} \approx 10^{-2} \,\text{light days} \tag{1.5}$$

In the case of a black hole, the compactness is maximized. R is the radius of the Innermost Stable Circular Orbit (ISCO), defined, for a non-spinning black hole, as:

$$r_{ISCO} = \frac{6\mathrm{GM}}{c^2} \tag{1.6}$$

The efficiency has its maximum values for rotating BHs, i.e. Kerr BHs where $r_{ISCO} \approx R_S$.

Equation 1.1 states that the luminosity of an AGN primarily depends on its accretion rate, which in turns primarily depends on the amount of fuel available and on the mass of the central BH. Assuming a spherical symmetry and a gas of fully ionized hydrogen accreting onto a black hole of mass $\mathrm{M_{BH}}$, an upper limit for the luminosity is given by the *Eddington luminosity* $\mathrm{L_{Edd}}$ (Eddington, 1925). This luminosity is reached when the radiation pressure balances he gravitational pull of the black hole:

$$\mathrm{L_{acc}} \leqslant \mathrm{L_{Edd}} = \frac{4\pi \mathrm{Gcm_p}}{\sigma_\mathrm{T}} \mathrm{M_{BH}} = 1.3 \times 10^{46} \frac{\mathrm{M_{BH}}}{10^8 \mathrm{M}_\odot} \tag{1.7}$$

where m_p is the proton mass and σ_T [1] is the Thomson cross section of the electron. In reality, the geometry is rather axially than spherically symmetric. Luminosities and accretion rates higher than the Eddington limit in so-called *Super-Eddington accretion* are possible. If the luminosity exceeds the Eddington luminosity the gas is expelled.

The ratio of the observed accretion luminosity to the Eddington luminosity (called the *Eddington ratio*: $\lambda_{edd} = \mathrm{L_{acc}}/\mathrm{L_{Edd}}$) is a useful measure for comparing BH accretion rates over a wide range of BH masses.

1.3.2. ACCRETION-DISC STRUCTURE

Dynamical arguments suggest that matter orbiting a central massive object (a black hole in the case of AGN) will settle into a flattened structure. Probably, the gas lost from tidally disrupted stars dissipate energy through shocks and radiation, but conserves angular momentum, which leads to the formation of an accretion disc. Within the accretion disc, magnetic fields and turbulence transport angular momentum outwards and mass

[1] The Thomson cross section is:

$$\sigma_T = \frac{8\pi}{3} \left(\frac{e^2}{m_e c^2} \right)^2 = 6.65 \times 10^{-25} cm^2 \tag{1.8}$$

inwards down to the innermost stable circular orbit of the black hole, beyond which the material plunges into the event horizon of the BH. Assuming that a particle at distance r from the BH dissipates energy locally, and assuming that the medium is optically thick, we can approximate the local emission as a black-body. We can estimate the luminosity:

$$L = \frac{GM\dot{M}}{2R_{disc}} = 2\pi R_{disc}^2 \sigma_{SB} T^4 \tag{1.9}$$

where σ_{SB} is the Stefan-Boltzmann constant and T is the temperature. Solving it for the temperature and r:

$$T = \left(\frac{GM\dot{M}}{4\pi R_{disc}^3 \sigma_{SB}} \right)^{\frac{1}{4}} \tag{1.10}$$

A more correct derivation takes into account how the energy is dissipated in the disc through viscosity (see Par. 1.3.2), which is a consequence of work being done by viscous torques. This yields:

$$T(r) = \left\{ \frac{3GM\dot{M}}{8\pi\sigma_{SB} r^3} \left[1 - \left(\frac{R_{in}}{r} \right)^{\frac{1}{2}} \right] \right\}^{\frac{1}{4}} \tag{1.11}$$

where R_{in} defines the inner edge of the disc. For $r \gg R_{in}$ the equation 1.11 can be simplified and put in terms of R_S (which is a lower limit to R_{in}). Assuming $L \sim L_{Edd}$ we obtain a temperature:

$$T \approx 5 \times 10^5 \left(\frac{M}{10^8 M_\odot} \right)^{\frac{1}{4}} K \tag{1.12}$$

Most of the luminosity is released in the inner part of the disc and the more massive is the black hole, the cooler is the disc. Using the Boltzmann constant k_B we can put the previous equation in terms of energy:

$$k_B T \approx 40 \left(\frac{M}{10^8 M_\odot} \right)^{\frac{1}{4}} eV \tag{1.13}$$

THE SHAKURA-SUNYAEV DISC

The models of disc accretion faced the basic problem that the orbiting material must lose angular momentum. The total angular momentum of the system must be conserved, thus, the angular momentum lost due to matter in-falling has to be offset by angular momentum gain of matter far from the center (angular momentum "transport" must occur). In the early 1970s Nikolai Shakura and Rashid Sunyaev proposed a useful approximate solution to the problem of the angular momentum transport, applicable to geometrically thin but optically thick accretion discs, with a constant rate of accretion (Shakura & Sunyaev, 1973). In the Shakura and Sunyaev α-disc model, the rotation is assumed to be Keplerian and the disc is in a steady state. They proposed turbulence in the gaseous material of the disc to be the main source of viscosity. In a turbulent medium, we have $\upsilon \approx \upsilon_{turb}\lambda_{turb}$, where υ_{turb} is the velocity of turbulent cells relative to the mean gas motion, and λ_{turb} is the size of the largest turbulent cells, which is estimated as $\Omega\lambda_{turb} \approx h = c_s/\Omega$ and $\upsilon_{turb} \approx c_s$, where $\Omega = (GM)^{1/2} r^{-3/2}$ is the Keplerian orbital angular velocity, r is the radial distance from the central object of mass M, c_s is the speed of sound in the medium and h is the half thickness of the disc. Assuming subsonic turbulence ($v_{\text{turb}} < c_s$) and assuming $\lambda_{\text{turb}} \lesssim h$, the viscosity (called *alpha viscosity prescription*, can be approximated as:

$$\nu = \alpha c_s h \tag{1.14}$$

The α is a free parameter between zero (no accretion) and approximately one (maximum rate of accretion). By using the equation of hydrostatic equilibrium, combined with conservation of angular momentum and assuming that the disc is thin, the equations of disc structure may be solved in terms of the α parameter.

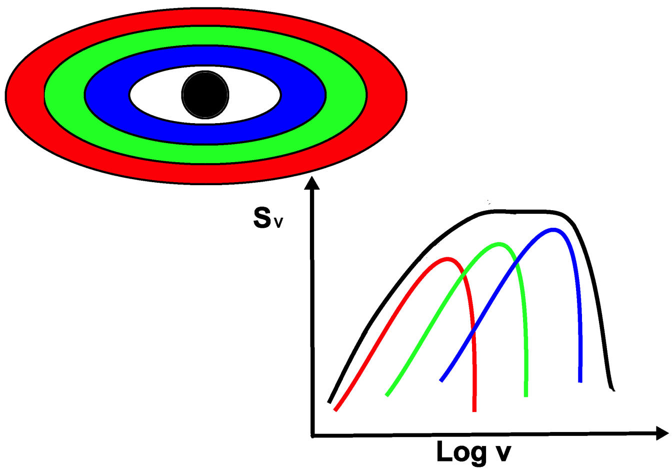

Figure 1.3: Spectral energy distribution for a geometrically thin optically thick steady-state accretion disc based on the α-disc model. The central relatively flat portion of the distribution is characterized by a $\nu^{1/3}$ slope.

The energy flux radiated from surface unit of the disc in unit of time is:

$$Q = \frac{3}{8\pi}\frac{\text{GM}\dot{\text{M}}}{r^3}\left\{1 - \left(\frac{R_{in}}{r}\right)^{\frac{1}{2}}\right\} \tag{1.15}$$

Due to the mass conservation $\dot{\text{M}}$ is constant. In the case of radiative vertical transport, in an optically thick disc ($\tau \gg 1$), each element of the disc radiates as a black-body with an effective temperature: $Q = \sigma_{SB}\text{T}^4$. From this and the equation1.15 it is possible to find equation 1.11. At large radii ($r \gg R_{in}$) we have:

$$\text{T} \simeq 3.7 \times 10^5 \left(\frac{\text{M}}{10^8\text{M}_\odot}\right)^{-\frac{1}{2}} \left(\frac{\dot{\text{M}}}{1\text{M}_{*\odot}/\text{yr}}\right)^{\frac{1}{4}} \left(\frac{\text{r}}{\text{R}_\text{S}}\right)^{-\frac{3}{4}} \text{K} \tag{1.16}$$

The characteristic temperature of the disc is then 10^5 K, in agreement with the equation 1.12; the relation $\text{T(r)} \propto \text{r}^{-\frac{3}{4}}$ can be used to find the spectrum of the disc. Using the black-body assumption the spectral energy distribution is described by the Planck function:

$$\text{B}_\nu \propto \nu^3 \left[\text{e}^{\left(\frac{\text{h}\nu}{\text{k}_\text{B}\text{T}}\right)} - 1\right]^{-1} \tag{1.17}$$

This results in the form of the spectral energy distribution reported in Figure 1.3. For AGN, the observable disc emission is primarily in the upper, relatively flat portion of the distribution. A relativistic version of the α-disc model is given by Novikov & Thorne 1973.

1.3.3. NARROW AND BROAD-LINE REGIONS

One of the first distinguished observational properties of AGN is the presence of emission lines with Doppler widths of the order of 10^3 to a few 10^4 km s^{-1} . The most prominent of these lines are the hydrogen Balmer series lines Hα λ6563, Hβ λ4861 and Hγ λ4340, the hydrogen Lyα λ1216. Also common lines of ions Mg II λ2798, [C III] λ1909 and C IV λ1549. These lines are in many cases much narrower (a few hundred kilometers per second) forbidden or semi-forbidden emission lines. The narrower widths and the lack of variability of the latter led to the conclusion that they emanated from a region that was much larger and kinematically separate from that of the broad lines. This led to their respective designation as the broad-line region (BLR) and the narrow-line region (NLR).

The typical size of the BLR is 10 – 100 light-days in Seyfert 1 galaxies, and up to a few light years in bright quasars. The electron density in the BLR is at least 10^8cm^{-3}, as judged from the absence of strong, broad forbidden lines, and the typical gas velocity is 3000–10000 km s^{-1} . The typical density of the NLR is $10^3 - 10^6$cm^{-3}, and the gas velocity 300–1000 km s^{-1} . The NLR must be much larger than the BLR, since no clear variation of the narrow emission lines is observed in objects undergoing large continuum variations. The NLR is resolved by ground-based observations in several nearby Seyferts, showing dimensions of 100 – 300 pc.

The NLR is the largest spatial scale where the ionizing radiation from the central source dominates over the stellar light; it is the only AGN component which is spatially resolved in the optical. The general properties of the NLR that should be kept in mind are that the emission comes from a spatially extended region ($\sim 10 - 10^4$pc) and that the forbidden line emission is isotropic since self-absorption in the narrow line region is negligible. Low density ($n_e \lesssim 10^6$cm^{-3}), hot (T $\sim 10^4$ K) gas in this extended region is ionized by high-energy photons from the inner AGN regions. The geometry of the central obscuring structure means that the ionized NLR gas can be anisotropically distributed (in an “ionization cone”, for instance).

1.3.4. THE DUSTY TORUS

The dusty molecular torus surrounding the central engine of AGN is expected to consist of molecular gas as well as of warm and hot (T $\sim$ 100 – 1500 K) dust. The simplest torus is made of a smooth matter distribution. More elaborated structures, made of clumps and inter-clump material, are preferred by observations. The gas at the inner radius of the torus is ionized by the central source. Deeper in, the torus contains dusty molecular gas.Its inner radius is set by the dust sublimation temperature (see e.g. Netzer & Laor 1993, Netzer 2015), and its geometry is subject to extensive research. Recently ,the torus has been proposed to be clumpy (Nenkova et al. (2008); Hönig & Kishimoto (2010); Marinucci et al. (2016)). The origin of the torus could, for example, involve matter coming off the relatively cold, outer regions, of the accretion disc. That matter could form a clumped wind structure about the disc perimeter. Alternatively, the matter could accrete from ambient matter from within the host galaxy. Also, scenarios involving outflowing clouds from the disc embedded in a hydromagnetically driven disc wind have been proposed.

1.4. UNIFIED MODEL

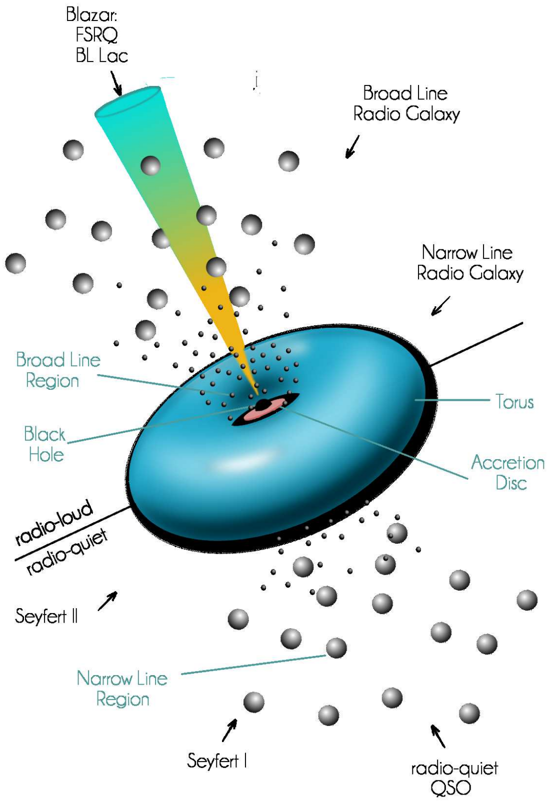

Figure 1.4: General structure of AGN according to *Unified model.* Image credit: F. Krauß after Urry & Padovani 1995

Not all the features described above are observed in all AGN. Besides all the observational diversity, it is now largely accepted that all the radio-quiet AGN classes share the same intrinsic structure and the different observed characteristics are due to the different inclination relative to the obscuring torus (see Section 1.3.4). One of the most important observational evidence of this obscuring structure was in 1985, when Antonucci and Miller (Antonucci & Miller, 1985) observed the Seyfert 2 galaxy NGC 1068 in polarized light. The scattered light in the nuclear region revealed broad lines, like those seen ubiquitously in Seyfert 1 galaxies. This suggests that Type 1 and Type 2 Seyfert galaxies are intrinsically the same, but the BLR of Seyfert 2 is hidden from view, while the NLR is visible for both since its large scale. This led to the idea which is known as AGN *Unification* (see Antonucci 1993, Urry & Padovani 1995 and Bianchi et al. 2012b for a more recent review).

According to this model, all AGN are powered by the accretion onto a central supermassive black hole (SMBH). The material approaching the SMBH forms an accretion disc and, through viscous drag, part of the gravitational potential is converted to radiation. The emission of the disc is a combination of thermal blackbodies, with the peak in the far UV. The interaction of this soft photons with a plasma of relativistic hot electrons on the top of the disc, the *corona*, is supposed to produce the observed X-ray emission (see section 2.4). In the circumnuclear environment, there are clouds of gas in Keplerian motion with respect to the SMBH. In radio-loud AGN (roughly 15-20% of the population), relativistic jets emerge from the central region along the disc axis, emitting Doppler-boosted radiation via synchrotron emission and inverse Compton scattering mechanisms. The inner part of the AGN, up to the BLR, is supposed to be enshrouded in an optically and geometrically thick ($N_H > 10^24cm^{-2}$) torus-like structure, composed of molecular clouds and dust, that is opaque to most of the electromagnetic radiation. Therefore, an observer looking at AGN edge-on (i. e. on the torus plane) can not see the innermost region of the AGN, because the view is obstructed by the intercepting material. In this case, only the narrow emission lines are directly visible. Vice-versa, an observer looking face-on (i.e. along the axis) has a direct view of the BLR, the NLR and the accretion disc emission (see Figure 1.4). The Unified Model explains the major differences between type-1 and type-2 AGN with a surprisingly small number of assumptions. Seyfert 2s galaxies have a spectra which is weaker at low energies (below 1-2 keV) with respect to Seyfert 1s spectra. This effect is caused by the photoelectric absorption of the soft X-ray photons by the dusty torus.

Although the Unified Model has allowed to explain much of the complex AGN phenomenology, an increasing set of observations appear to be in conflict with some of the key predictions of the Unified Model (Bianchi et al. 2012a; Bianchi et al. 2012b), e.g. that each Seyfert 2 has an obscured Seyfert 1 nucleus (a hidden broad-line region).

2

X-RAY PROPERTIES OF ACTIVE GALACTIC NUCLEI

"All truths are easy to understand once they are discovered; the point is to discover them."

Galileo Galilei

Electromagnetic radiation between ~ 120 eV (0.01Å) to ~ 120 keV (10Å) is referred to as X-rays. Similarly to the case of the UV range, X-rays are not able to penetrate the Earth's atmosphere, and it is thus necessary to fly detectors at high altitudes. The X-ray domain has seen an enormous evolution over recent decades, and is currently one of the key energy ranges to study AGN.

The aim of this chapter is to describe the X-ray properties of Active Galactic Nuclei, the physical processes that generate this emission and the spectral shape of the X-ray emission.

2.1. EMISSION MECHANISMS

Much of the electromagnetic radiation produced by AGN is very different from a black body emission or stellar radiation. This section addresses the various different processes which lead to the production of X-rays in AGN, forming the characteristic spectral shapes. A complete discussion of the topic can be found in B. Rybicki & P. Lightman 1979.

2.1.1. BREMSSTRAHLUNG

Bremsstrahlung, or *free-free emission*, is the radiation due to the emission of a charged particle in a Coulomb field of other charges. The word "Bremsstrahlung" is a German word meaning "braking radiation", which refers to the way in which electrons are "braked" when they hit a metal target. Both before and after the braking, the incident electrons are free, i.e. not bound to an atom. The resulting radiation spectrum is continuous and if the energy of the incident charge is high enough, they emit X-rays after they have been braked.

A full understanding of this process requires a quantum treatment, since photons of energies comparable to that of the emitting particle can be produced. However, a classical treatment is justified in some regimes, and the obtained formulas have the correct functional dependence of most of the physical parameters. Then the quantum correction could be introduced in the form of Gaunt factors.

Here we calculate the total power and the Bremsstrahlung radiation spectrum in the case of an electron, charge e^- passing close to an ion of charge Ze^+ with impact parameter b, see Figure 2.1, and velocity v. Since the mass of the ion is much larger than that of the electron, we can assume just the motion of the latter and the ion at rest. Let us assume also that the motion of the electron is along a line, that corresponds to the assumption that the motion is not violently perturbed by the interaction. The characteristic time t_c, called the *collision time*, i.e. the time during which the electron is in close interaction with the ion, is:

$$t_c = 2\frac{b}{v} \tag{2.1}$$

There is also a characteristic frequency:

$$\omega = t_c^{-1} \propto \frac{v}{b} \tag{2.2}$$

Assuming the acceleration constant during the interaction, and equal to:

$$a \approx \frac{e^2}{m_e b^2} \tag{2.3}$$

A charged particle accelerating in a vacuum radiates power, as described by the Larmor

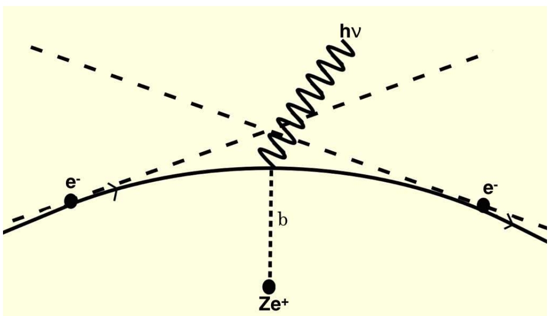

Figure 2.1: An electron of charge e^- moving past an ion of charge Ze^+ .

formula, so the formula for total radiated power is given by:

$$P = -\frac{dE}{dt} = \frac{2}{3}\frac{e^2 a^2}{c^2} = \frac{4}{3}\frac{Z^2 e^6}{c^3 m_e^2 b^3 v} \tag{2.4}$$

In the real case we can consider a cloud of ions with number density n_Z and free electron with number density n_e. Each electron experiences $2\pi n_Z v b db$ collision with impact parameter between b and $b+db$. The total number of collisions is:

$$N_{tot} = 2\pi n_e n_Z v b db \tag{2.5}$$

The total emissivity from a cloud emitting via Bremsstrahlung, in which the electrons have the same fixed velocity, is:

$$J_{br}(v,\nu) = \frac{dE}{d\nu dV dt} = 2\pi n_e n_Z v \int_{b_{min}}^{b_{max}} \frac{16}{3}\frac{Z^2 e^2}{c^3 m_e^2 b^2 v^2} b db = \frac{32\pi Z^2 e^6}{3c^3 m_e^2}\frac{n_e n_Z}{v}\ln\left(\frac{b_{max}}{b_{min}}\right) \tag{2.6}$$

Where b_{max} is some value of b beyond which the $b \ll v/\omega$ asymptotic result is inapplicable and the contribution to the integral becomes negligible. The value of b_{max} so is of the order of v/ω. The value of b_{min} could be estimated in two way. The first concerns the possibility to treat the collision process in term of classical orbits. By the Heisenberg uncertainty principle $\Delta x \Delta t \gtrsim \hbar$ and taking $\Delta x \sim b$ and $\Delta p \sim m_e v$ we have:

$$b^q_{min} = \frac{h}{2\pi m_e v} \tag{2.7}$$

The second way came from the classical physic requirement that $\Delta v \leqslant v$:

$$b^c_{min} = \frac{4Ze^2}{\pi m_e v^2} \tag{2.8}$$

When $b^c_{min} \gg b^q_{min}$ a classical description of the scattering process is valid, vice-versa the classical description cannot strictly be used.

THERMAL BREMSSTRAHLUNG

When the plasma is at equilibrium, the process is called *thermal Bremsstrahlung*. A set of particles at thermal equilibrium follow the Maxwell-Boltzmann distribution:

$$f(v)dv = 4\pi \left(\frac{m_e}{2\pi k_B T}\right)^{\frac{3}{2}} e^{-\frac{m_e v^2}{2k_B T}} v^2 dv \tag{2.9}$$

Thus the number density of electrons whose velocity is between v and $v+dv$ is $n_e(v) = n_e f(v)dv$. Replacing $n_e(v)$ in equation 2.6 and integrating over velocity distribution is possible to find the thermal Bremsstrahlung emission (for details see B. Rybicki & P. Lightman 1979):

$$J_{br}(\mathrm{T},\nu) = \frac{\mathrm{dE}}{\mathrm{d\nu dVdt}} = 6.8\times 10^{-38}\mathrm{Z^2 n_e n_Z T^{-\frac{1}{2}} e^{-\frac{h\nu}{2k_B T}} g_{ff}(T;\nu)}\ \left[\mathrm{ergs\ s^{-1}\ cm^{-3}\ Hz^{-1}}\right] \tag{2.10}$$

where $g_{ff}(\mathrm{T};\nu)$ is a *velocity averaged Gaunt factor*. The thermal Bremsstrahlung spectrum is flat up to an exponential cut-off. The cut-off frequency depends on the temperature only, and is conventionally set when the exponential is equal $1/e$, i.e. $h\nu \sim k_B\mathrm{T}$, see Figure 2.2. from the ratio between the energy density of the electrons and the power density we can estimate the cooling time:

$$t^{br}_{cool} \approx 2\times 10^{11} n_e^{-1}\mathrm{T}^{\frac{1}{2}}\ [\mathrm{s}] \tag{2.11}$$

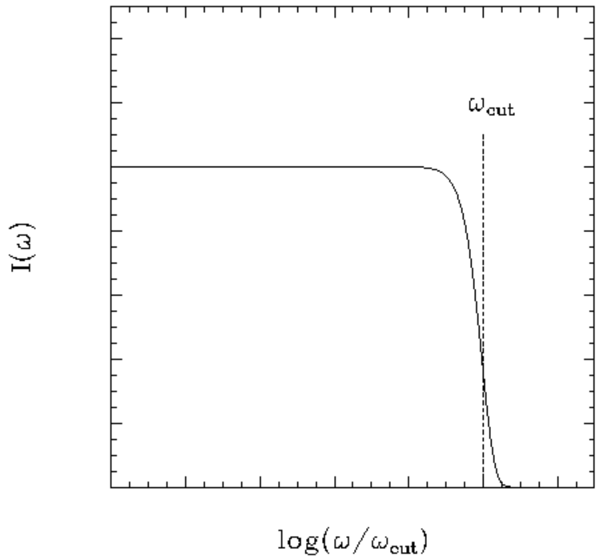

Figure 2.2: Spectrum produced in the Bremsstrahlung process. The spectrum is flat up to a cut-off frequency ω_{cut}, and falls off exponentially at higher frequencies.

FREE-FREE ABSORPTION

The spectrum shown in Figure 2.2 is correct as long as the medium producing the radiation is *optically thin*. In a medium which is optically thin, any internally generated radiation is essentially free to escape from the emitting region without further interaction with the medium. If the medium is *optically thick*, radiation generated is only moving a short distance within the medium (relative to its size) before being absorbed again. The shape of the spectrum is set by the balance of both emission and absorption processes.

Since we are considering cloud in thermal equilibrium, we can use the Kirchoff's law to find out the absorption coefficient:

$$S_\nu = \frac{j_\nu}{\alpha_\nu} = B_\nu = 2\frac{h\nu^3}{c^2}\frac{1}{e^{-\frac{h\nu}{k_B \mathrm{T}}} - 1} \tag{2.12}$$

where B_ν is the intensity of the black-body emission. From equation 2.12 we obtain the absorption coefficient:

$$\alpha_\nu^{ff} \simeq 3.7 \times 10^8 Z^2 n_Z n_e \mathrm{T}^{\frac{1}{2}} \nu^{-3} \left(1 - \mathrm{e}^{-\frac{\mathrm{h}\nu}{\mathrm{k_B T}}}\right) \left[\mathrm{cm}^{-1}\right] \tag{2.13}$$

When $h\nu \ll k_B\mathrm{T}$ (Rayleigh-Jeans regime), $\alpha_\nu^{ff} \propto \nu^{-2}$, when $h\nu \gg k_B\mathrm{T}$ (Wien regime), $\alpha_\nu^{ff} \propto \nu^{-3}$. Due to the self-absorption, the Bremsstrahlung spectrum has a cut-off also at low energy, see Figure 2.3. The net important effect is that the free-free absorption gets larger at lower frequencies, while at high photon frequencies the medium is optically thin.

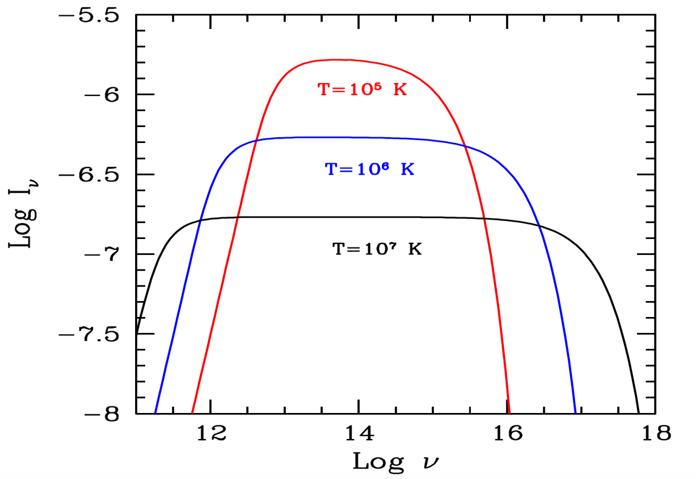

Figure 2.3: The Bremsstrahlung intensity from a source of radius R = 10^{15} cm and density $n_e = n_Z = 10^{10}$ cm^{-3} for different temperatures (from Ghisellini 2013). The Gaunt factor is set to one.

2.1.2. SYNCHROTRON RADIATION

When charged particle are forced by magnetic field to follow curved trajectories they emit electromagnetic radiation in the direction of their motion (Figure 2.4). Lorentz force is responsible for this kind of radiation. For non relativistic velocities, the radiation is called *cyclotron radiation* and the frequency of emission is simply the frequency of gyration in the magnetic field. For extreme relativistic particles, the radiation is known as *synchrotron radiation* and the frequency is much more complex. Considering a charge q of mass m in a magnetic field **B**:

$$\omega_B = \frac{q\mathbf{B}}{\gamma mc} \tag{2.14}$$

The acceleration is perpendicular to the velocity, with magnitude $a_\perp = \omega_B v_\perp$. The total emitted power is given by the Larmor formula:

$$P = \frac{2}{3}\frac{q^2}{c^3}\gamma^4 a^2 \tag{2.15}$$

Since $P \propto a^2 \propto \omega_B^2 \propto m^{-2}$, for a given velocity, heavier particles are less effective than lighter, so we can focus only on electron synchrotron emission. For electrons with isotropic velocities distribution, the emitted radiation is given by the average of the Larmor formula over all angles for a given velocity β. The result is:

$$P = \left(\frac{2}{3}\right)^2 r_0^2 c\beta^2\gamma^2\mathbf{B}^2 = \frac{4}{3}\sigma_t c\beta^2\gamma^2 U_B \simeq 1.1\times10^{-15}\beta^2\gamma^2B^2 \ \left[\text{ergs s}^{-1}\right] \tag{2.16}$$

where $r_0 = e^2/m_e c^2$ is the classical electron radius, $\sigma_t = 8\pi r_0^2/3$ is the Thomson cross section and U_B is the magnetic energy density: $U_B = \mathbf{B}^2/8\pi$.
For all $\gamma \gg 1$ the factor $\beta^2 = 1 - 1/\gamma^2 \approx 1$ can be ignored. Relativistic effects multiply the average radiation power by a factor γ^2 compared with the non relativistic ($\gamma = 1$).

Electrons in a plasma emitting synchrotron radiation cool down. The time scale for this to occur is given by the energy of the electrons divided by the rate at which they are radiating away their energy. The energy is $E = \gamma mc^2$. Assuming $\beta \simeq 1$:

$$t_{cool}^{syn} = \frac{3m^2c^3}{4\sigma_T U B^2 E_{max}} 7.75\times10^8 B^{-2}\gamma^{-1} \ [\text{s}] \tag{2.17}$$

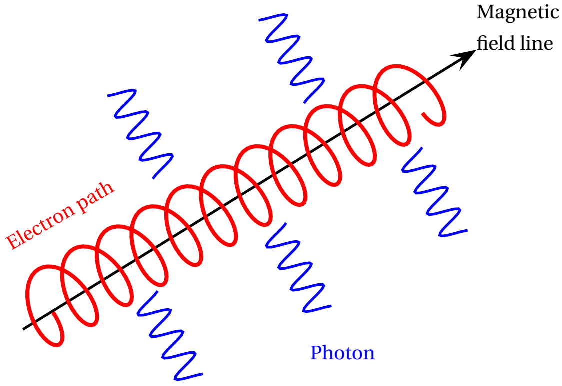

Figure 2.4: Synchrotron radiation diagram. A particle gyrates along the magnetic field lines. Its trajectory has an helicoidal shape.

Around a super massive black hole, the typical magnetic field is $B = 10^4$ [gauss], so the cooling time of an electron with $\gamma = 10^3$ is $t_{cool}^{syn} \sim 10^{-3}$ s.

Spectrum of Synchrotron Radiation

The spectrum of synchrotron radiation is related to the variation of the electric field as seen by an observer. The emitted radiation fields appears to be concentrated in a narrow cone of semi-aperture $1/\gamma$, due to the relativistic beaming effect. Thus, the observer will see a pulse of radiation confined to a time interval which is smaller than the gyration period. The observed duration of the pulse is roughly:

$$\Delta t \approx \frac{1}{\gamma^3 \omega_B} \tag{2.18}$$

Synchrotron radiation is a very spiky series of widely spaced narrow pulses, peaking at a *critical frequency*, i..e. the maximum Fourier component of the pulse:

$$\omega_c = \frac{3}{2}\gamma^3 \omega_B \sin(\theta) \tag{2.19a}$$

$$\nu_c = \frac{3}{4\pi}\gamma^3 \omega_B \sin(\theta) \tag{2.19b}$$

where θ is the angle between the velocity and the magnetic field. For electrons with $\gamma \sim 10^3$ in a magnetic field of $B \sim 10^{-5}$ [gauss], the critical frequency is $\nu_c \sim 100$ MHz, thus the synchrotron emission is at radio frequency. However for high velocities, like those achieved by charged particles in relativistic jets observed in radio-loud AGN ($\gamma \sim 10^7$), the critical synchrotron frequency is in the X-ray band.

It can be shown (see B. Rybicki & P. Lightman 1979) that the power spectrum for the synchrotron emission is:

$$P(\nu) = \frac{\sqrt{3}}{2\pi} \frac{e^3 B \sin(\theta)}{mc^2} F\left(\frac{\nu}{\nu_c}\right) \tag{2.20}$$

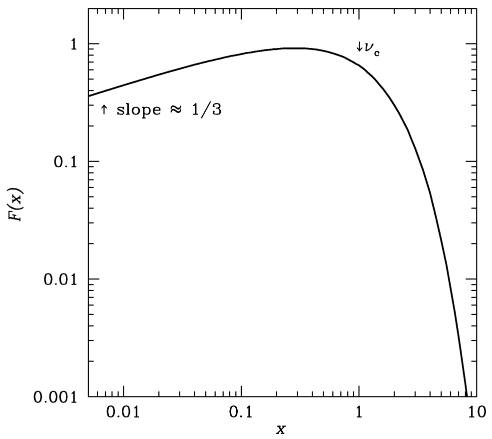

Figure 2.5: The synchrotron spectrum of a single electron plotted in terms of $F(x)$, with $x = \nu/\nu_c$.

where F is a function defined as:

$$F(x) = x\int_x^\infty K_{5/3}(z)dz \tag{2.21}$$

$K_{5/3}(z)$ is the modified Bessel function on the order of $5/3$.

$$F\left(\frac{\nu}{\nu_c}\right) \propto \begin{cases} \left(\frac{\nu}{2\nu_c}\right)^{\frac{1}{3}}, & (\nu \ll \nu_c) \\ \left(\frac{\nu}{\nu_c}\right)^{\frac{1}{2}} e^{-\frac{\nu}{\nu_c}}, & (\nu \gg \nu_c) \end{cases} \tag{2.22}$$

The F function peaks at $\nu \sim 0.29\nu_c$; at $\nu \gg \nu_c$ the function decays exponentially, while the low frequency part can be approximated by a power-law of slope $1/3$ (see Figure 2.5). Now we can compute the synchrotron spectrum for a set of relativistic electrons. The number density of particles with energy between γ and $\gamma + d\gamma$ is approximately $N(\gamma)d\gamma = C\gamma^{-p}d\gamma$. Integrating this quantity times the single particle radiation formula over all γ we obtain the total power radiated per unit volume per unit frequency:

$$P_{tot}(\nu) = C\int_{\gamma_1}^{\gamma_2} P(\nu)\gamma^{-p}d\gamma \propto \int_{\gamma_1}^{\gamma_2} F\left(\frac{\nu}{\nu_c}\right)\gamma^{-p}d\gamma \tag{2.23}$$

Changing the variable of integration to $x \equiv \nu/\nu_c$:

$$P_{tot}(\nu) \propto \nu^{-\frac{(p-1)}{2}} \int_{x_1}^{x_2} F(x)x^{\frac{p-3}{2}}dx \tag{2.24}$$

The extremes of integrations depend on $\nu \propto \gamma^2$. However, if the energy limits are sufficiently wide, we can approximate $x_1 \approx 0$ and $x_2 \approx \infty$. In this case we have:

$$P_{tot}(\nu) \propto \nu^{-\frac{(p-1)}{2}} \tag{2.25}$$

The spectrum is described by a power law $P \propto \nu^{-\alpha}$ with the spectral index:

$$\alpha = \frac{p-1}{2} \tag{2.26}$$

Typically $p \simeq 2-3$ and $\alpha \simeq 0.5-1$.

Synchrotron emission is accompanied by absorption, as for Bremsstrahlung emission. A photon interacts with a charge in the magnetic field ad it is absorbed. Another process that can occur is stimulated emission, or negative absorption, in which a particle is induced to emit more strongly into a direction and at a frequency where photons are already present. The absorption coefficient is (see B. Rybicki & P. Lightman 1979):

$$\alpha_\nu \propto \nu^{-\frac{(p+4)}{2}} \tag{2.27}$$

2.1.3. Compton Scattering

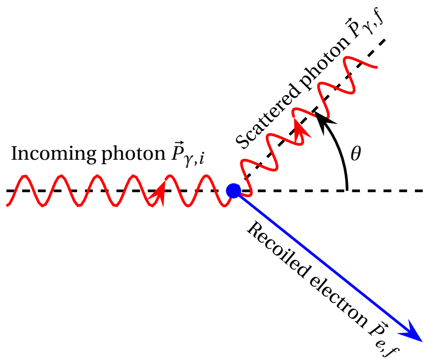

Figure 2.6: Geometry for scattering of a photon by an electron at rest.

Thomson scattering, or the scattering of a photon by an electron at rest, only strictly applies to low photon energy, i.e. when $h\nu \ll m_e c^2$.In Thomson scattering the incident photon and scattered photon have the same wavelength or energy, so this scattering is also called *coherent* or *elastic*. If the photon energy is comparable to or greater than the electron energy, non-classical effects must be taken into account, and the process is called Compton scattering. A further interesting situation develops when the electron is moving. In this case, energy can be transferred to the photon, and the process is called inverse Compton scattering. This last process is an important mechanism in high-energy astrophysics.

Considering a photon with initial four-momentum $\vec{P}_{\gamma,i} = (h\nu_i)(1, \vec{n}_i)$ colliding with an electron at rest (see Figure 2.6). After the collision the photon will have four-momentum $\vec{P}_{\gamma,f} = (h\nu_f/c)(1, \vec{n}_f)$, where $\vec{n}_i$ and $\vec{n}_f$ are the initial and final directions of the photon. The initial and final four-momenta of the electron are $\vec{P}_{e,i} = (mc, \mathbf{0})$ and $\vec{P}_{e,f} = (E/c, \mathbf{p})$. Due to the recoil of the charge, the scattering is no more elastic. From the conservation of momentum and energy, we obtain the final energy of the photon:

$$h\nu_f = \frac{h\nu_i}{1 + \frac{h\nu_i}{m_e c^2}(1 - \cos\theta)} \tag{2.28}$$

In term of wavelength, this can be written:

$$\lambda_f - \lambda_i = \lambda_C(1 - \cos\theta) \tag{2.29}$$

Where λ_C is the *Compton wavelength*, defined as:

$$\lambda_C \equiv \frac{h}{m_e c} = 0.02426\text{Å} \tag{2.30}$$

For $\lambda \gg \lambda_C$ (i.e., $h\nu \ll m_e c^2$) the scattering is close to be elastic. When this condition is satisfied, we can assume that there is no change in photon energy in the rest frame f the electron.

When the electrons are no longer considered to be at rest, there can be a transfer of energy from the electron to the photon. This process is called *Inverse Compton*. Inverse Compton scattering can produce substantial fluxes of photons in the optical to X-ray region. Analysis shows that the mean frequency of the photons after the collision increases by a factor γ^2, so that high-frequency radio photons in collisions with relativistic electrons for which $\gamma$is of order 10^3 to 10^4 can be boosted in the UV and X-ray regions.

Let us consider an electron moving with a relativistic velocity β in the observer's frame K, and a photon with initial energy E_i propagating in a direction which forms an angle ψ_i with the electron velocity. In the frame comoving with the electron, K', we have the Doppler effect:

$$E'_i = E_i\gamma(1 - \beta\cos\psi) \tag{2.31}$$

The final energy of the photon, in the rest frame of the electron, is given by equation 2.28. If the initial photon energy in K' is much less than $m_e c^2$, we can approximate $E'_f \simeq E'_i$, and transforming back in the observer's frame K:

$$E_f \simeq \gamma(1 + \beta\cos\psi'_f) \tag{2.32}$$

The net effect, as said above, is an increasing of the energy of the photon of a factor γ^2. There is a practical limit to the amount of boosting possible which can be seen from the conservation of energy:

$$h\nu_f = \gamma m_e c^e + h\nu_i \tag{2.33}$$

Thus, the scattered photon energies are limited to $\gamma m_e c^2$.

The power emitted in the case of an isotropic distribution of photons is:

$$P_{Comp} = \frac{3}{4} c\sigma_T \gamma^2 \beta^2 U_{rad} \tag{2.34}$$

where U_{rad} is the radiation energy density of the photon field (before scattering). Note how similar this is to the power due to synchrotron emission. The losses due to synchrotron and Compton process are in the ratio of the magnetic field energy density to the photon field energy density, and it is independent of γ:

$$\frac{P_{Comp}}{P_{Sync}} = \frac{U_{rad}}{U_B} \tag{2.35}$$

The scattered photons may be produced in the source through synchrotron radiation, and these are boosted then the resultant photons are called *Synchrotron Self Compton*.

From equation 2.34 we can compute the total Compton power, per unit volume, for a medium of relativistic electrons. Let $N(\gamma)d\gamma$ be the number of electrons per unit volume with γ in the range of γ and $\gamma + d\gamma$. Then, for example, the total power for a thermal plasma of non-relativistic electrons of number density n_e is:

$$P_{tot} = \left(\frac{4k_B \mathrm{T}}{m_e c^2}\right) c\sigma_T n_e U_{rad} \tag{2.36}$$

The number in the parentheses is the fractional photon energy gain per scattering. SO, if the electron temperature is high enough (i.e., $4k_B\mathrm{T} > \mathrm{E}$), for each scattering the photon gain an energy of $\frac{4k_B\mathrm{T}}{m_e c^2}$ minus the energy loss due to the electron recoil. We can estimate the cooling time of the process:

$$t^{IC}_{cool} = \frac{3m_e c}{8\sigma_T U_{rad}} \sim 1.6\times 10^7 U^{-1}_{rad}\ [\mathrm{s\ ergs\ cm^{-3}}] \tag{2.37}$$

To give a complete description we need to take into account multiple scattering.

Thermal Comptonization

The process of multiple scattering of photons by a thermal distribution of electrons is called *thermal Comptonization*. Let define the *Compton parameter y*, to determine whether a photon will significantly change its energy in traversing a finite medium. The Compton parameter is the average fractional energy change per scattering ($\frac{\Delta\epsilon}{\epsilon}$) times the mean number of scattering. If $y > 1$ the Comptonization is important because the Comptonized spectrum has more energy than the spectrum of the seed photons. For a plasma with optical depth τ, the number of scattering is of the order of $\tau^2 + \tau \simeq max(\tau;\tau^2)$. For non relativistic electrons with $E \ll 4k_B\mathrm{T}$, in thermal equilibrium:

$$y_{th,nr} = \frac{4k_B\mathrm{T}}{m_e c^2} \times max(\tau;\tau^2) \tag{2.38}$$

If $\tau \gg 1$ each photon will scatter $\sim \tau^2$ times before escape, so the final energy of the photon will be:

$$E_f = E_i e^y \tag{2.39}$$

If $E_f = 4k_B\mathrm{T}$ the process saturate since the photon stop gain energy.
For relativistic electrons, from equation 2.34, we have $\frac{\Delta\epsilon}{\epsilon} = \frac{4\gamma^2}{3}$, so:

$$y_{nt,r} = \left(\frac{4k_B\mathrm{T}}{m_e c^2}\right)^2 \times max(\tau;\tau^2) \tag{2.40}$$

$\tau < 1$

In the case of small optical depth:

$$y = \frac{\Delta\epsilon}{\epsilon}\tau \tag{2.41}$$

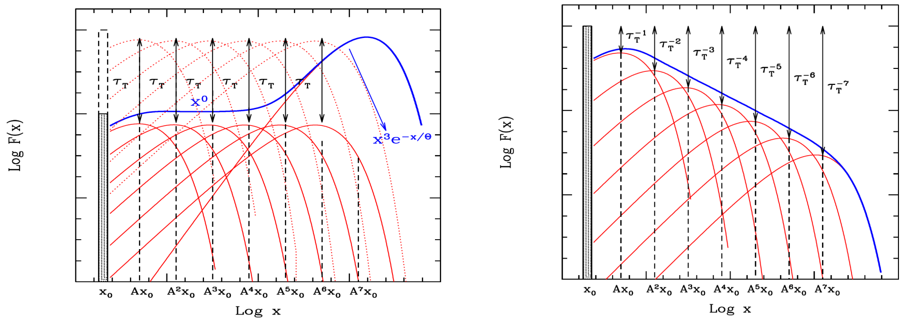

Figure 2.7: Left panel: multiple Compton scattering when $\tau > 1$ and $y \gg 1$. For the first scattering order, *nearly* all the photons are scattered. Therefore the number of photons escaping is the same at each scattering order. When the photon frequency is the order of Θ , photons and electrons are in equilibrium and, even if only a small fraction of photons can escape, they do not change frequency and therefore they form a *Wien bump*. Right panel: multiple Compton scattering for $\tau < 1$. A fraction τ of the photons of the previous scattering order undergoes another scattering and amplifying the frequency by a factor A, until the photon frequency equal the electron temperature Θ. Then further scattering leave the photon frequency unchanged.
Both plots are adapted from Ghisellini 2013.

We can define the amplification factor:

$$A \equiv \left(\frac{4k_B\mathrm{T}}{m_e c^2}\right)^2 \tag{2.42}$$

After k scatterings, the energy of the photon is increased by a factor A^k. The intensity of emergent radiation has the form of a power-law (see right panel of Figure 2.7):

$$F_\nu \propto \nu^{-\alpha} \tag{2.43}$$

with:

$$\alpha = -\frac{\ln(\tau)}{\ln(A)} = \frac{\ln(\tau)}{\ln(y) - \ln(\tau)} \tag{2.44}$$

$\tau \gg 1$

In the case of very large optical depth the interaction between photons and matter becomes so intense that they go to equilibrium, and they will have the same temperature. But instead of black-body the spectrum has a Wien shape. This is because photons are conserved. The Wien spectrum has a slope:

$$F_\nu \propto \nu^3 e^{-\nu} \tag{2.45}$$

$\tau > 1,\ y > 1$

In this case it is necessary to solve the Boltzmann equation for Compton scattering to find the intensity of the emission. It is possible to show (see B. Rybicki & P. Lightman 1979) that the emerging spectrum is a power-law (see left panel of Figure 2.7):

$$F_\nu \propto \nu^{-\alpha} \propto \nu^{3+m} \tag{2.46}$$

where:

$$m = -\frac{3}{2} \pm \sqrt{\frac{9}{4}\frac{4}{y}} \tag{2.47a}$$

$$\alpha = -\frac{3}{2} \mp \sqrt{\frac{9}{4}\frac{4}{y}} \tag{2.47b}$$

2.2. THE COMPLEX X-RAY SPECTRUM OF ACTIVE GALACTIC NUCLEI

The study of the X-ray emission from AGN is a fundamental tool to have a direct probe of their innermost regions. The X-ray emission from AGN extends from the Galactic absorption cutoff at a few tenths of keV up to a few hundreds of keV. The typical X-ray continuum can be roughly represented by a power-law with photon index Γ, defined as $F(E) \propto E^{-\Gamma}$ in units of ph cm^{-2} s^{-1} keV^{-1}; the relation with the spectral index α (equation 2.47b) is $\alpha = 1 - \Gamma$.

The X-ray continuum is ubiquitous in AGN and can be explained by thermal Comptonization of the soft UV radiation (Haardt & Maraschi, 1993). This continuum is reprocessed (Matt et al., 1991) by cold neutral circumnuclear medium (e.g. the accretion disc or the molecular torus) and gives rise to a reflection bump at around 30 keV and a broad iron, Kα line emission at around 6.4 keV. In addition to the main power-law, observations show a rise of the spectrum below 1-2 keV (Arnaud et al. 1985; Bianchi et al. 2009). This feature is called *soft excess* and its origin is still under debate (Done et al., 2007b). The main features of AGN X-ray spectra are discussed below and are shown in Figure 2.8.

2.2.1. THE PRIMARY EMISSION

The spectral shape of the X-ray emission from AGN is a a power-law, with a photon index ranging between 1.5 and 2 (Nandra & Pounds 1994, Bianchi et al. 2009 and Piconcelli et al. 2005). The power-law continuum often shows a high-energy cut-off, presumably due to the cut-off of in the energy distribution of the electrons responsible for the X-ray emission and usually located around a few hundreds keV (Perola et al. 2002, Malizia et al. 2014, Fabian et al. 2015, Marinucci et al. 2016, Fabian et al. 2017 and references therein). These features are directly related to the temperature and optical depth of the plasma of hot electrons responsible for the power-law emission.

As said before, the primary continuum in AGN is produced by a Comptonization mechanism; this process is believed to arise from the inner regions of AGN, close to the central super-massive black hole, in the corona (Section 1.2.1). In this region electrons multiple inverse-Compton scatter some of the low-energy UV and optical photons from the disc to X-ray energies (Fabian et al., 1989). The analysis of the primary X-ray continuum can give information about the parameters of this plasma of electrons, like temperature and optical depth. Geometry of the Comptonizing corona has been considered in various ways. Haardt & Maraschi (1991) suggested a simple model where a uniform

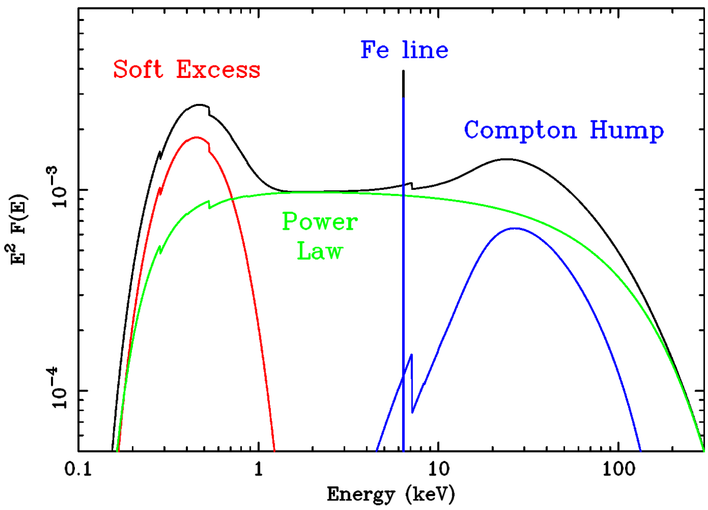

Figure 2.8: Main components of typical X-ray spectrum of an unobscured AGN, adapted from Fabian & Miniutti 2005.

plane-like corona "sandwiches" the accretion disc. However this *slab* corona can be easily cooled by Comptonization, and cannot maintain a temperature which is high enough to explain actually observed X-ray spectra. The geometry of the corona is still uncertain. Apart from the slab geometry it could be a sphere, or a *patchy* medium. In Section 2.4 the model of the hot corona are discussed in details.

2.2.2. THE COMPTON REFLECTION AND IRON Kα LINE

The illumination of neutral/ionized materials surrounding the central BH (like the accretion disc and the molecular torus) by the primary emission, gives rise to a characteristic *reflection* spectrum which is the result of Compton scattering and photoelectric absorption followed either by Auger de-excitation or by fluorescent line emission (Guilbert & Rees 1988, Matt et al. 1991). The main features of this reflection component are a continuum, due to electron scattering which peaks at around 30-40 keV (*reflection hump*) and a cut-off at around 4-5 keV due to the the decrease of photoelectric absorption cross section with respect to electron scattering (Magdziarz & Zdziarski, 1995a). The ratio between the reflected flux and the direct flux received by an observer is called *reflection fraction* $\mathscr{R}$, and represents the reflection efficiency. $\mathscr{R}$ could be considered as an estimator of the solid angle subtended by the reflector ($\mathscr{R} = \Omega/2\pi$ Magdziarz & Zdziarski 1995a). The reflection efficiency is typically a few percent of the direct emission in the 2-10 keV range because of photoelectric absorption, rising to $\sim 30\%$ at the 30 keV peak for a Compton thick reflector covering a significant fraction of the solid angle (Ghisellini et al., 1994). The efficiency drops if the reflecting medium is Compton thin (part of the incident radiation can escape).

The gas in the disc can be ionized due to the illumination from the primary X-ray

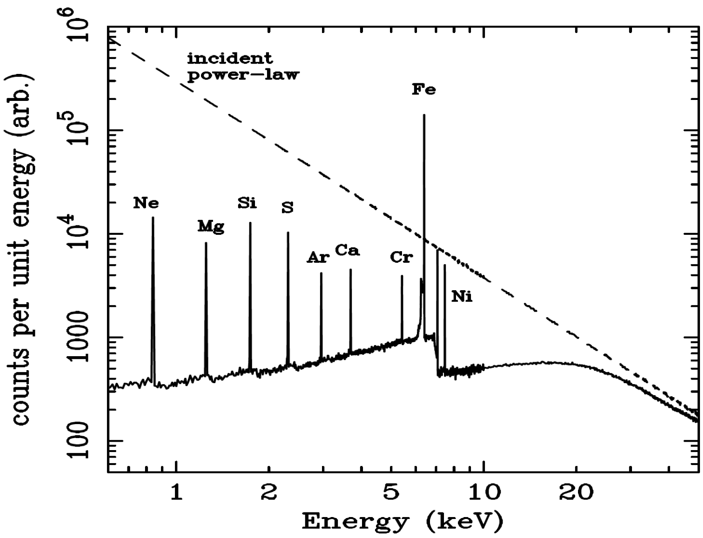

Figure 2.9: *Monte Carlo* simulations of the reflection spectrum from a neutral geometrically thin disc, with solar abundance of elements, adapted from Reynolds 1996.

emission. The degree of the ionization of the gas can be described by a quantity called *ionization parameter*, defined as:

$$\xi = \frac{L}{nr^2}\ \left[\mathrm{erg\,cm\,s^{-1}}\right] \tag{2.48}$$

where L is the illuminating luminosity, n is the gas density and r is the distance of the illuminating source from the scattering gas. As ξ gets higher, the number of electrons bound in light atoms decreases, and the photo-absorption cross section decreases at lower energies.

The absorption of photons with energies $E < 10$ keV can give rise to several fluorescence emission lines from the most abundant heavy elements. In particular, we can note the presence of neutral/ionized Fe K emission in the range of energies $6.4 \lesssim E \lesssim 7$ keV. Iron has the highest cosmic abundance among the heavy metals and it has the highest fluorescence yield, so the strongest line is the Fe Kα (see Figure 2.11, Matt et al. 1997, Fabian et al. 2000). When the X-ray photons irradiate the plasma, one of the two K-shell (i.e., the principal quantum number n equal to one) electron is ejected from the iron atom. The resulting excited state decays when an L-shell ($n = 2$) electron drops into the K-shell, either releasing an emission line at 6.4 keV (34% probability), or ejecting another electron (66%probability) (Auger effect) (Fabian et al., 2000).

The FeKα line is pretty narrow in itself, but when it originates in an accretion disc, it becomes broader due to kinematics effects, and its profile (shape) changes due to Doppler boosting and gravitational redshift. These effects are relevant when the line is produced in the disc at few gravitational radii. If the line is produced at large disc radii, it will have a symmetric profile due to the Doppler effect, with two peaks: a "red" one produced by the emitting material from the receding side of the disc and a "blue" one which

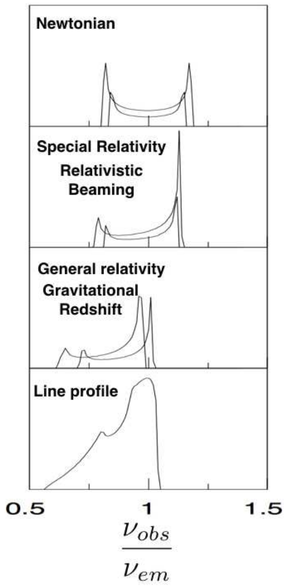

Figure 2.10: The profile of the intrinsically narrow FeKα line modified by the interplay of (from the top to the bottom) Doppler shift, relativistic beaming and gravitational redshift. In the last panel, there is the representation of the total line profile given by the overall combination of the effects above. Adapted from Fabian & Miniutti 2005.

corresponds to the emitting material from the approaching side of the disc. The broadest part of the line comes from the innermost regions of the disc, where the rotation velocity of the emitting material is higher.Close to the central black hole, orbital velocities of the disc are relativistic and the spectrum becomes affected by special and general relativistic effects causing broadening/smearing of spectral features. These effects result in the enhancement of the "blue" peak with respect to the "red" one (relativistic beaming). Figure 2.10 shows these different effects on an intrinsically narrow emission line and their overall combination. Since the strength of the relativistic effects strongly depends on the distance from the BH, the reflection spectrum can give an estimate of the innermost disc radius and an upper limit of the *Innermost Stable Circular Orbit* (ISCO) radius.

2.2.3. THE SOFT EXCESS

Many AGN show an extra emission below ~ 2 keV, away from the extrapolated 2-10 keV power-law emission. It is known as *soft-excess* and was first seen by Arnaud et al. (1985) in the Seyfert galaxy Mrk 841. It is a common feature in AGN spectra but the precise origin of this soft excess is still unknown and under debate (Bianchi et al., 2009).

Piro et al. 1997 studied the soft excess with *ROSAT* and *Ginga* finding that no model fitted satisfactorily the 17 objects they analysed, concluding that soft excess phenomenon is likely to vary from source to source.

The soft excess is a largely featureless component which can be fitted with one or more black-body components, to model the disc thermal emission. However, temperatures are too high to be simply the high energy tail of the accretion disc emission (Gierliński & Done, 2004). This temperature has a small spread, regardless of the mass or mass accretion rate of the central black hole, which requires some fine-tuning (Gierliński & Done, 2004). If the accretion disc is strongly ionized, the reflection from the disc surface can enhance the emission at low energies. Incorporating ionized disc reflection models, such as those described by Ballantyne et al. (2001) or Nayakshin et al. (2000), can not only account for the finite-width ionized iron line, but also adds to the soft emission.

The next most obvious continuum origin for the soft excess is Comptonized disc emission. The observed rollover at ~ 0.6 keV implies an electron temperature of $kT_e \sim 0.1-0.2$ keV, and the shape of the spectrum implies a large optical depth $\tau \sim 20$.

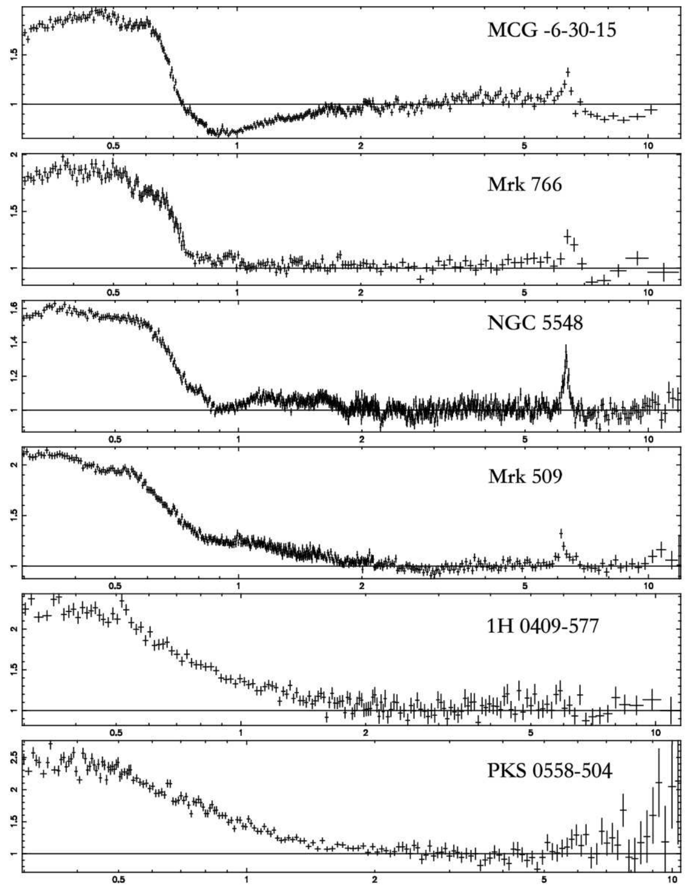

Figure 2.11: The soft excess for six Seyfert 1 galaxies measured by *XMM-Newton*. The abscissa is the photon energy in keV while ordinate shows the ratio of the data points to a power-law fitted over the 2-10 keV energy band. Taken from Pounds & Reeves (2002).

2.2.4. Absorption Features

AGN X-ray spectra may be affected by absorption from the complex structures surrounding the central black hole.

Warm Absorber

A region between the NRL and the BLR (0.1-10 pc from the center), with intermediate to large column densities ($N_H \sim 10^{21-23} cm^{-2}$) and a density larger from 10 to 100 times than the one in the BLR, is expected to produce strong absorption and emission features in the X-ray spectrum, around ~ 0.7 – 0.8 keV. This component is called *warm-absorber*. The strongest spectral features related to this component are absorption lines of the most abundant elements, strong bound-free absorption edges and several emission lines (Reynolds 1997, Crenshaw & Kraemer 1999). The main (and diagnostically most useful) manifestation of X-ray warm absorbers is narrow absorption lines (Kaastra et al., 2000), similar to those seen for many years in the UV. Absorption from layers of photo-ionised gas in the circumnuclear region of AGN is commonly observed in more than half radio-quiet object.

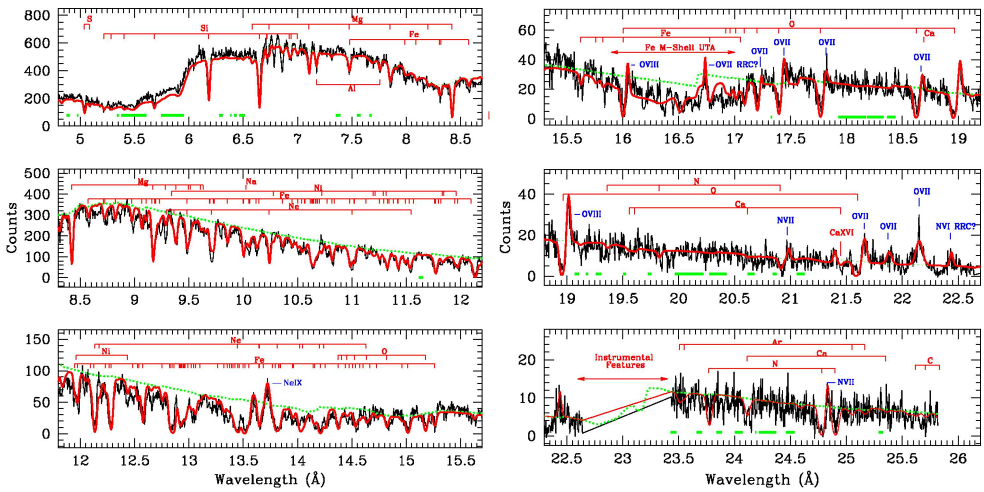

Figure 2.12: Two-phase absorber model plotted against the first-order spectrum of NGC 3783. Absorption lines predicted are marked in the top (red). Single labels stand for emission lines (blue). The line-free zones are indicated at the bottom of each panel (green). The continuum level (including edge continuum absorption) is overplotted for comparison (dotted green line). The spectrum is presented in the rest-frame system of the absorbing gas. Taken from Krongold et al. (2003)

In Figure 2.12 an example of the complex spectral features imprinted by the warm absorber in the soft spectrum of the bright Seyfert 1 galaxy NGC 3783 superimposed on a simple two-phase model fitting most of the absorption features is reported .

The absorption and emission features due to this highly ionized gas are usually blue-shifted with respect to the systemic velocity of the sources, indicating that the warm absorbers are outflowing with typical velocities around $10^2 - 10^3$km s^{-1}. There is increasing evidence of the presence of narrow blue-shifted absorption lines at rest frame energies greater than 6.4 keV (Braito et al. 2007; Cappi et al. 2009). Highly blue-shifted iron K-shell absorption lines around 7 keV have been detected in the X-ray spectra of several AGN indicating absorption from mildly relativistic outflows with velocities up to ~ 0.4c (see Tombesi et al. (2010) and references therein). These are the so-called *Ultra-Fast Outflow* (UFOs). Warm absorbers and UFOs could be part of the same, large-scale, outflow (Tombesi et al., 2013).

COLD ABSORPTION

As we have seen in Chapter 1, spectra of types 2 AGN are strongly affected by photoelectric absorption by cold neutral material along the line of sight (e.g. the obscuring torus). By measuring the energy of the photoelectric absorption it is possible to estimate the column density of the absorbing material. If $N_H > 10^{24}cm^{-2}$, the gas is thick to Compton scattering. In Compton thick sources with $N_H > 10^{25}cm^{-2}$ the primary X-ray radiation is totally absorbed at any energies. If N_H does not exceeds $\sim 10^{25}cm^{-2}$, the radiation is totally absorbed below 10 keV, but it is still transmitted and observable between 10-100 keV (Matt et al., 1997).

It should be noted that absorption of hard X-rays is due to metals, therefore what we actually compute is the column of metals. To infer the equivalent column of hydrogen, generally solar abundances are assumed. However some AGN display super-solar abundance; as a consequence hydrogen column densities are overestimated.

2.3. X-RAY VARIABILITY

Rapid and irregular variability of the observed X-ray emission in the line, as well as in the continuum, in flux and spectral shape, is a common property for most AGN. These variations can provide information on the physical conditions, the size, and the geometry of the X-ray emitting region. X-ray sources are expected to be highly variable due to their compactness (since net observed variability is governed by the source light-crossing time, see Mushotzky et al. 1993 for a review). If the variability time-scale is t, the size of a source of mass M should be roughly:

$$r \lesssim ct \simeq \frac{t}{50\mathrm{s}}\left(\frac{\mathrm{M}}{10^7\mathrm{M}_\odot}\right) \tag{2.49}$$

The X-ray emission from AGN shows the highest variability amplitudes on shortest time scale (less than ~1 day) with respect to other wavebands. This implies that enormous amount of energy are released in a very short time in flare-like events. A useful way to characterize variability is in terms of the *Power Density Spectrum* (PDS), which is the product of the Fourier transform of the light curve and its complex conjugate and represents the amount of variability power, P, as a function of Fourier frequency, f. The PDS for AGN is often parametrized as a power law: $P \propto f^{-\alpha}$, with $1 \lesssim \alpha \lesssim 2$ over time-scales from hours to month (Vaughan et al., 2003). The total power in the variations is given by integrating the PDS over all frequencies. Thus, the PDS must turn over at low frequencies (i.e., $\alpha < 1$ at low frequencies), to prevent divergence in the total power (González-Martín & Vaughan, 2012). The physical origin of the PSD break time-scale is not understood, however it could be associated with the inverse Compton cooling time (Ishibashi & Courvoisier, 2012). Since the break time scale scales with the black hole mass, it is likely to be linked to some characteristic time scale at a particular radius of the flow. For example, in black hole binaries the break is generally interpreted in terms of the viscous time scale at the outer radius of the hot flow (e.g. Done et al. 2007a).

Another estimator for the variability is the *normalized excess variance* (Nandra et al. 1997; Vaughan et al. 2003), the variance of the light curve after subtracting the contributions from measurements errors. The excess variance is found to anti-correlate with the black hole mass (Ponti et al., 2012).

The flux variability has been studied in details by dedicated X-ray satellites like *Rossi X-ray Timing Explorer* (RXTE) which made several important discoveries, including the confirmation that AGN iron fluorescence line flux variations need not correlate with the continuum variability (Reynolds, 2000). Observed variations of the FeKα line, both in shape and intensity, are less than those of the high energetic continuum which is assumed to give rise to the line emission. Also it seems that there is no correspondence between the continuum variation and the response of the line on time scales from several minutes to several days. The line and the continuum variations seem to be uncorrelated (Życki, 2004). But detection of reverberation lags in many AGN demonstrates there is some fraction of correlated variability (the line and soft band continuum respond linearly to continuum variations on short time scales). However, this is difficult to dig out, and requires refined techniques that can disentangle components varying on different time scales. This variability could be due to disc instability, reflecting in perturbations of the disc emissivity, or it could be caused by external effects such as gravitational microlensing.

Spectral variability is also commonly observed in AGN. The spectral variations observed provide valuable details of the physical conditions of the X-ray reprocessing (Miniutti et al., 2007) and/or on the physical properties of absorbing material which may exist close to the central source (see e.g. Miller et al. (2008)). The photon index is found to correlate with the characteristic frequency in the PSD and this correlation is driven by accretion rate, for a given black hole mass: objects with a higher accretion rate relative to the Eddington limit should also have a steeper spectrum and a shorter characteristic time scale when normalised to the BH mass (Papadakis et al., 2009). The spectrum is usually found to have the so-called *softer-when-brighter* behaviour, i.e. the spectrum is softer when the flux is higher (Sobolewska & Papadakis, 2009). The softer-when-brighter behaviour could be explained in the Comptonization scenario. An increase of the power of the seed photons illuminating the corona determines a more efficient cooling of the hot electrons, with a resulting drop in the coronal temperature, which causes the X-ray spectrum to steepen (Soldi et al., 2014).

Another characteristic of the spectral-timing properties of the X-ray variability is the presence of the *time-lags* between the light curves in different energy bands. The observed lags are *hard* for long time scales X-ray variability, in the sense that variations in hard photons (above 2 keV) lag those in soft photons (below 1-2 keV) (e.g. Papadakis (2011); McHardy et al. (2004) and Vaughan et al. (2003)), and *time-scale dependent*, i.e. time delay increases towards lower Fourier-frequencies (longer variability time-scales).

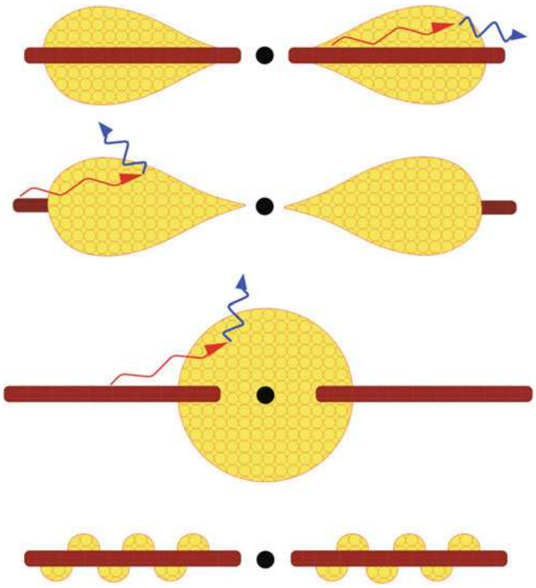

Figure 2.13: Geometries of the central black hole (black), the accretion disc (brown), and Comptonizing Corona(yellow), proposed to explain the formation of the primary X-ray component. From the top to the bottom is shown the "sandwich" geometry, two "sphere+disc" geometries and the *patchy* corona (Reynolds & Nowak, 2003).

The hard-lags are also seen in X-ray binaries and are interpreted in terms of propagation of mass accretion rate fluctuations in the disc. Different time-scales are introduced to the accretion flow at different distances from the compact object, and the propagation time-scales are comparable to the time-scales of the perturbations (Kotov et al., 2001). Soft-lags also have been observed in a number of sources, when testing the short time scale X-ray variability and have been interpreted as a signature of the relativistic reflection (Fabian et al., 2009). which responds to continuum changes after the light-crossing time from the source to the reflecting region. The characteristic time-scales of the soft lags are generally short (in the range from tens to hundreds of seconds), and correlated with the black hole mass (De Marco et al., 2013).

2.4. THE CORONA

Geometry of the Comptonizing corona generating the power-law-like primary continuum has been considered in various ways. Haardt and Maraschi, 1991 (see above, section2.4.1) suggested a simple model, where a uniform plane corona "sandwiches" the accretion disc (see upper panel of Figure 2.15). The bottom three "photon starved" geometries in Figure 2.15 are currently possible candidates for the corona in which the primary continuum is generated. In this section I present the theoretical models that have been proposed to describe the hot, Comptonizing corona.

2.4.1. DISC-CORONA MODEL

In the disc-corona scenario (or *two phases model*) originally proposed by Liang (1979), and revived by Haardt & Maraschi (1991) and Haardt & Maraschi (1993), the inner region of an AGN is essentially composed of two phases: a hot, optically thin, X-ray emitting corona located above a cold, optically thick, UV-emitting accretion disc. In this model the two phases are coupled: the emission from the disc provides the soft photon input for the Comptonization and the hard Comptonized photons contributed to the heating of the thick phase. One possible configuration that satisfies the above condition is a plane-parallel corona above an accretion disc. In this case the condition $y \simeq 1$ (see section 2.1.3) is achieved only if the entire available gravitational power is released in the hot corona. In this case the *reprocessed thermalized* radiation coincides with the UV bump, and the *reprocessed reflected* radiation forms the 30 keV Compton hump. To a first approximation, the geometry of the system can be assumed to be plane-parallel, where the two phases are two homogeneous and isothermal layers (Haardt et al., 1994). The same condition can be satisfied if there are several such smaller regions above the disc, rather than a single smooth corona. In this case the non-uniform, *patchy* corona consists of several blobs and only a fraction of the available energy needs to be released in the hot corona.

Approximating the two-phase as two uniform adjacent slab, the fraction of gravitational power, $\mathscr{P}_g$, dissipated in the hot layer with optical depth τ, will be f. The power dissipated within the optically thick phase will be $(1-f)\mathscr{P}_g$. Assuming the main cooling mechanism is the Comptonization(i.e., $\tau < 1$), the total luminosity radiated in all directions is AL_{disc}, with A an amplification factor due to Comptonization, that could be calculated with some geometrical and energetic considerations, and L_{disc} is the total soft luminosity. The luminosity added by Compton processes is $L_{Comp} = (A-1)L_{soft}$. It could be broken into the upward component, L_{uC}, and the downward component, L_{dC}:

$$L_{Comp} = (A-1)L_{disc} = L_{uC} + L_{dC} \tag{2.50}$$

The hard photons directed downward are partially absorbed and partially reflected by the optically thick layer. The reflected power, $L_{refl} = aL_{dC}$, contributed to the hard component of the emitting spectrum, the absorbed power, $Ł_{abs} = (1-a)L_{dC}$, contributed to the radiated luminosity L_{disc}.

We get the energy balance for the cold, optically thick layer, i.e. the accretion disc:

$$(1-f)\mathscr{P}_g + (1-a)L_{dC} = L_{disc} \tag{2.51}$$

and the energy balance for the hot, optically thin layer, i.e. the corona:

$$f\mathscr{P}_g + L_{disc} = AL_{disc} \tag{2.52}$$

Solving for L_{disc} and A, with the previous definitions, we get:

$$\begin{cases} L_{disc} = \{1 - f\,[1-(1-a)\eta]\}\,\mathscr{P}_g \\ A = 1 + \frac{f}{1-f[1-(1-a)\eta]} \end{cases} \tag{2.53}$$

Where η is the fraction of Compton luminosity emitted towards the disc, it quantifies the anisotropy of Compton processes: The outgoing luminosity L_{out} is then $L_{out} = \mathscr{P}_g$

In the limit $f = 1$, all the gravitational power is dissipated in the corona and the disc itself does not emit radiation, *passive disc*. In this limit, η is typically $0.5-0.6$ and $a \sim 0.1-0.2$. For an optically thin corona $A = 3$, for an optically thick corona, $A = 2$. Assuming $a = 0$ and $\eta = 0.5$, we found $A = 3$.

Since the Comptonization spectrum has a power-law spectral shape (see Section 2.1.3):

$$I(E) = I(E_0)\left(\frac{E}{E_0}\right)^{-\alpha} \tag{2.54}$$

Assuming the soft photons in a quasi-black body spectral shape (peaking at $\sim 3k_BT$), the soft luminosity will be:

$$L_{disc} \propto I(E_0)E_0 \tag{2.55}$$

and the Compton luminosity:

$$L_{Comp} = \int_{\epsilon_{min}}^{\epsilon_{max}} I(E)dE \tag{2.56}$$

with $\epsilon_{min} = E_1$ and $\epsilon_{max} = 3k_BT = E_0A_1$. We find an equation for the heating/cooling ratio, which is another expression for A (see Haardt & Maraschi 1991):

$$A - 1 \simeq \frac{1}{1-\alpha}\left[\left(\frac{3k_BT}{E_0}\right)^{1-\alpha} - (A_1)^{1-\alpha}\right] \tag{2.57}$$

The spectral index α is function of the temperature and the optical depth:

$$\alpha = -\frac{\ln\tau}{\ln A_1} \qquad \tau < 1 \tag{2.58}$$

For $f = 1$ we found $1.1 < \alpha < 1.4$ ($2.1 < \Gamma < 2.4$) for a large range of optical depth and temperature values. The physical reason is that the corona adjusts its optical depth and temperature to keep a constant value of the heating/cooling ratio (i.e., amplification factor, which is set by geometry) to satisfy the energy balance.

Haardt et al. (1994) developed the two phase model also with the assumption that the corona could have a *patchy* structure because of the formation of magnetic loops in which the energy is stored and then dissipated by reconnection. The disc is no more passive but can contribute to most of the UV luminosity as in the standard Shakura Sunyaev model (see Section 1.3.2). This model explains also the variability of the observed emission that could be do to variations of the accretion rate or to stochastic variations of the number of blobs.

2.4.2. THE LAMP-POST MODEL

According to this model (Matt et al. (1991); Martocchia & Matt (1996); Henri & Petrucci (1997); Petrucci & Henri (1997); Martocchia et al. (2000); Miniutti & Fabian (2004)) the illumination of the disc is caused by a point-like source located on the rotation axis of the BH. This kind of source can be identified, e.g. with the base of a jet. As we have seen in

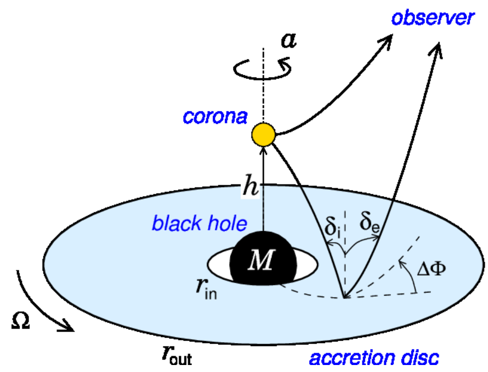

Figure 2.14: Scheme of the lamp-post geometry: the primary source is located above the black hole, on its the axis, at height h and illuminates the corotating accretion disc. The observer sees both the primary radiation and the reflection component distorted by light bending. Taken from Caballero-Garcia et al. (2017)

Section 2.3, the observed iron line and the continuum variations seem to be uncorrelated (Życki, 2004). The lamp-post scenario could explain this apparent absence of correlation between the above variations. The spectral shape of the reflection spectrum is determined also by the geometry of the illuminating and reflecting region (Martocchia et al. 2000; Martocchia et al. 2002), in addition to other factors such as the physical properties of the re-processing matter and the properties of the central gravitating body.

The strong gravitational light bending and redshift, due to the vicinity of the primary source to the black hole, allows strong variations of the flux of the observed continuum with respect to the reflection component (more than one order of magnitude) as the height of the primary sources varies (Miniutti & Fabian, 2004).

Recent detailed models for calculation of the reflection spectra use the lamp-post geometry (see e.g., García et al. 2013; Dauser et al. 2013). In this way, strong-gravity effects, due the vicinity of the primary X-ray sources to a black hole, are taken into account. In this scenario, the sources that showed a reflection dominated spectrum require a more compact corona, located near the black hole (Fabian et al., 2012). However, to produce the hard X-ray Compton spectrum, the source of the primary X-ray continuum must be large enough to intercept sufficient seeds photons (Dovciak & Done 2015; Dovčiak & Done 2016).

2.4.3. COMPACTNESS AND PAIR PRODUCTION

Let see now the role of the pair production in the hot corona. Electron-positron pair production from photon-photon collisions can be important in compact and luminous sources, when photons are energetic enough.

We have seen, (Section 2.4.2) that sources which are small and highly luminous can also be "compact" in radiative sense, meaning that interactions involving significant energy exchange between photons and particles are common in the source. The relevant parameter is the ratio of the source luminosity to size (L/R, Cavaliere & Morrison 1980). This is usually given in terms of the dimensionless *compactness* parameter (Ghisellini, 2013):

$$\ell = \frac{L}{R}\frac{\sigma_T}{m_e c^3} \tag{2.59}$$

where L is the luminosity, R is the radius of the source (assumed spherical), σ_T is the Thomson cross section and m_e is the mass of the electron. If $\ell \sim 1$, a particle loses a significant fraction of its energy crossing the region of the source.

The optical depth for the process in a source of a given luminosity, at high frequency, depends on the cross section, $\sigma_{\gamma-\gamma}$, on the density of the target, n_γ and on the size for which the process can occur, R: $\tau_{\gamma-\gamma} \sim n_\gamma \sigma_{\gamma-\gamma} R$. The density of the target is (Ghisellini, 2013):

$$n_\gamma(1\text{MeV}) \simeq \frac{L_X}{4\pi R^2 c m_e c^2} \tag{2.60}$$

Therefore $\tau_{\gamma-\gamma}$ could be written in terms of the compactness parameter ℓ:

$$\tau_{\gamma-\gamma}(1\text{MeV}) \sim \frac{\ell}{20\pi} \tag{2.61}$$

If the compactness is small an increase in the heating power leads to an increase of the temperature. But when the temperature reaches $\sim 2m_e c^2$(i.e., $\sim$ 1MeV), pair production becomes significant and the number of particles increases (Ghisellini & Haardt, 1994). Then the temperature start decreasing and the compactness and the heating power increase. At equilibrium pair production/annihilation occur at the same rate. If the source is compact (i.e., $\ell > 1$), the photon density is huge. This means that the cooling time scale for inverse Compton scattering is shorter than the light crossing time ($t_{cross} = R/2c$) and the pair production can play a major role in determining the outgoing spectrum and overall composition of the emitting source. The pair production acts as an ℓ-dependent thermostat. We have seen (Equation 2.60) that the pair density is proportional to the luminosity and the temperature and inversely proportional to the source size. Thus, the energy associated with the increased luminosity goes to increase the number of pairs rather than the temperature. Pair production becomes a runaway process, outstripping annihilation, soaking up energy and limiting any rise in temperature (Ghisellini & Haardt, 1994).

As said before, photon-photon collisions create electron-positron pairs when the temperature exceeds $\sim 2m_e c^2$ (i.e., $\sim$ 1MeV). The condition for pair production is $\tau_{\gamma-\gamma} > 1$. When $\tau_{\gamma-\gamma} > 1$ a significant fraction of the source luminosity is channelled into pair production, this corresponds to $\ell \gtrsim 60$. Since the size of the AGN coronæ is $\sim 10R_g$ the condition can be met in AGN.

Recent measure of temperature and compactness in AGN (Fabian et al. 2015, Fabian et al. 2017) suggests that these parameters follows the relations imposed by pair balance, suggesting that pair production/annihilation play an important role in determining the physics of the spectral properties of AGN.

THE COMPACTNESS-TEMPERATURE DIAGRAM

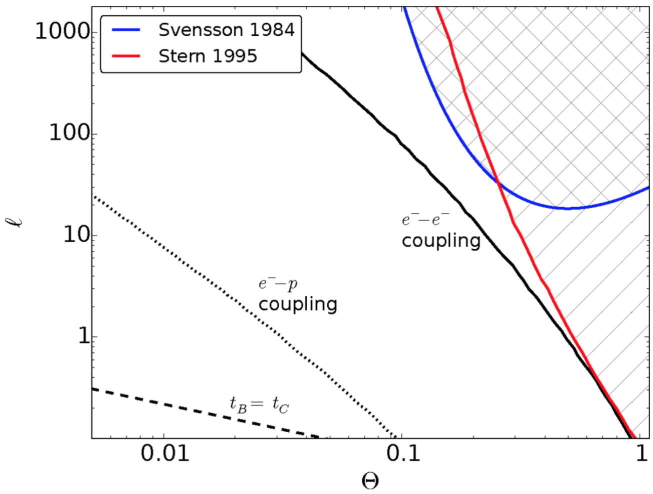

Figure 2.15: Theoretical compactness-temperature diagram, taken from Fabian et al. (2015). The red and blue curves are the pair runaway lines respectively for a disc-like or a spherical corona.

To understand the various physical properties of a physical finite, thermal plasma it could be useful to look at the compactness-temperature diagram $\Theta - \ell$ (Svensson 1984, Stern et al. 1995,Fabian et al. 2015) where Θ is the dimensionless temperature (Ghisellini & Haardt, 1994):

$$\Theta = \frac{k_B T}{m_e c^2} \tag{2.62}$$

The dominant radiation process in a plasma will be the one with the shortest cooling time. We have seen that in the hot corona the most significant processes are the Bremsstrahlung, the inverse Compton scattering and the pair production. Considering a spherical source of size R and scattering optical depth τ, which generates a luminosity L; the cooling time of the inverse Compton effect is (Equation 2.37):

$$t_C = \frac{3\pi R}{2cl(1+\tau)} \tag{2.63}$$

while the Bremsstrahlung cooling time is (see Equation 2.11:

$$t_{br} = \frac{\sqrt{\Theta} R}{\tau \alpha_f c} \tag{2.64}$$

where α_f is the fine-structure constant. Comparing the two cooling times, it is possible to see that the Comptonization dominates at high compactness ($\ell > 3\alpha_f \Theta^{-1/2}$).

When $3\alpha_f\Theta < \ell < 0.04\Theta^{-3/2}$ the dominant effect is the electron-proton coupling while for $.04\Theta^{-3/2} < \ell < 80\Theta^{-3/2}$ the electron electron coupling becomes relevant (Fabian, 1994).

As described above, beyond a certain regime the pair production becomes a run-away process. In the $\Theta - \ell$ plane this regime is identified by the, so-called, pair runaway lines. The position of these lines depends on the shape of the source and on the radiation mechanism. Stern et al. (1995) computed the pair balance curve for a slab corona (red line in Figure 2.15). Svensson (1984) estimated that the pair balance for an isolated cloud occurs where $\ell \sim 10\Theta^{5/2}e^{1/\Theta}$ (blue line in Figure 2.15).

3

THE X-RAY SATELLITES *XMM-Newton*, *Swift* AND *NuSTAR*

"We are all in the gutter, but some of us are looking at the stars."

Oscar Wilde

The aim of this chapter is to briefly discuss current hard X-ray telescopes, showing the developments in technology and to give an overview of the observatories which are used in this thesis: *XMM*-Newton, *Swift* and *NuSTAR*.

3.1. HARD X-RAY TELESCOPES

The hard X-ray band is a part of the electromagnetic spectrum which is relatively under-explored. Since X-rays are absorbed by the Earth's atmosphere, developments in X-ray astronomy lagged significantly behind those in optical or radio astronomy. Any observatory hoping to detect cosmic X-rays must be at a very high altitude (above ≈ 99-99.9999% of the atmosphere, depending on the X-ray photon energy). The other challenge in obtaining high-quality data is that X-ray photons are very difficult to focus; they are readily absorbed by the mirror materials used by UV, optical, and infra-red telescopes (rather than being reflected).

The first X-ray telescope using Wolter Type I grazing-incidence optics was employed in a rocket-borne experiment in 1965 to obtain X-ray images of the Sun (Giacconi et al., 1965). Ever since, the history of X-ray astronomy has been marked by technological breakthroughs going hand-in-hand with astronomical motivation to make better and better satellites, which are many orders of magnitude more sensitive than the pioneering experiments. The most basic elements of an X-ray telescope are the light gathering aperture and the detectors. Early X-ray experiments had very little directionality. Solar X-rays were first discovered by a crude pinhole camera payload onboard a Naval Research Laboratory rocket, with no means to collimate or focus the incoming radiation.

The next evolutionary step was to add collimators in front of the detectors. Collimators enable basic imaging of the sky in the same way a single dish radio telescope does: by pointing and imaging one field of view at a time. They are still used primarily for X-ray timing. Finer imaging is achieved by using coded aperture masks-which uses the principle of pinhole cameras.

A major breakthrough in soft X-ray astronomy came with the development of focusing optics. Unlike visible light, X-rays do not reflect near normal incidence. The index of refraction of solids for X-rays is slightly lower than unity. Hence, if X-rays are incident on a surface at incidence (or graze angles, which decreases with energy) below the critical angle, they undergo total external reflection. Based on this principle, the Einstein Observatory (HEAO 2; Giacconi et al. 1979) became the first satellite to use focusing X-ray optics. Today, focusing optics are regularly employed in soft X-ray telescopes. Most notable among them is Chandra, which attains subarcsecond angular resolution (Weisskopf et al., 2000).

Focusing telescopes concentrate light from the source onto a detector much smaller than the telescope aperture. Since sources can be extracted from smaller parts of the detector, the contributions from astrophysical and detector backgrounds are greatly reduced relative to a coded aperture mask. Hard X-rays from a point source are focused into a few square-millimeter spot. As compared to a coded aperture mask where the detector area is about a factor of two larger than the aperture, this reduces the background in the extraction region by 10^4 and improves the Signal to Noise Ratio (SNR) by a factor of 100 in background-limited observations. Compared to coded aperture masks, focusing telescopes are also more sensitive to diffuse sources.

3.2. *XMM-Newton*

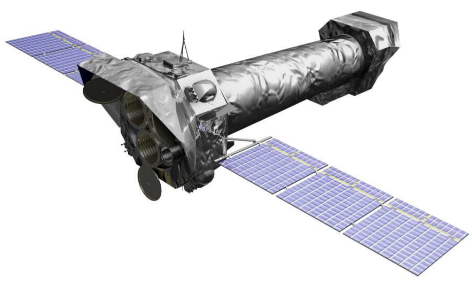

Figure 3.1: Artistic impression of the *XMM-Newton* spacecraft.

XMM-Newton is an X-ray observatory satellite named in honor of Sir Isaac Newton. XMM stands for X-ray Multi Mirror. It is a mission developed by the European Space

Agency (ESA), dedicated to exploring the Universe in the soft-X-ray part of the electromagnetic spectrum, between 0.2 and 12 keV (XMM Users Handbook, 2010). *XMM-Newton* was launched on December 10, 1999. It weighs 4 tons and is 10 m long. It is placed in a 48-hour elliptical orbit at 40 degrees. Its apogee is about 114000 km from Earth and its perigee about 7000 km (XMM Users Handbook, 2010).

XMM-Newton carries two distinct types of telescopes, an X-ray telescope, and an optical/UV telescope. Three types of instruments are on-board the satellite:

- The European Photon Imaging Camera (EPIC), for X-ray imaging, X-ray spectroscopy, and photometry (Strüder et al., 2001).
- The Reflection Grating Spectrometer (RGS), for high-resolution X-ray spectroscopy and spectro-photometry (Den Herder et al., 2001).
- The Optical Monitor (OM), for optical/UV imaging and spectroscopy (Turner et al., 2001).

The basic characteristics of *XMM-Newton* are: simultaneous operation of all science instruments; high sensitivity; good angular resolution; moderate and high spectral resolution; simultaneous optical/UV observations; and long continuous target visibility. A detailed description of the *XMM-Newton* mission can be found in XMM Users Handbook (2010).

The *XMM-Newton* observatory has three telescopes for collecting X-ray photons. The optics of each telescope consist of 58 nested mirror modules. They are designed to operate in the X-ray energy range of 0.1 keV to 12.0 keV, with a focal length of 7.5 m, and X-ray point-spread function values for the full width at half maximum (FWHM) on the order of 6 arc seconds and the half energy width (HEW) of about 15 arc seconds. Each mirror module consists of two parts. The front part has a paraboloid surface and the rear part a hyperboloid surface. This configuration allows for double reflection of the grazing X-rays, and therefore, focusing of X-rays. Behind each of the X-ray telescopes, an EPIC camera is installed, providing extremely sensitive imaging observations. As shown in Fig 3.2, *XMM-Newton* has much larger effective area than previous detectors working in the same energy band.

3.2.1. EPIC Cameras

The *XMM-Newton* telescope carries three EPIC cameras of two different types:

- MOS (Metal Oxide Semi-conductor) CCD arrays type;
- fully depleted pn CCDs

Two of the cameras are EPIC MOS CCDs, with the RGS in the light path. The third X-ray telescope has an unobstructed beam with an EPIC camera at the focus, using pn

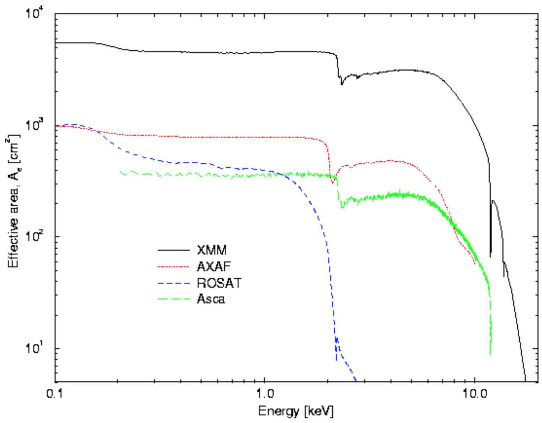

Figure 3.2: Comparison of the mirror effective areas of some X-rays observatories. Taken from XMM Users Handbook (2010).

CCDs. Each camera has a field of view (FOV) of 30 arc minutes. The cameras allow several modes of data acquisition, and different cameras may operate in different modes. The MOS and pn cameras are fundamentally different. They have different geometries and differ in others properties as well, such as their readout time.

All EPIC CCDs operate in a photon counting mode, producing so-called "event lists". An event is an X-ray hitting the detector. An event list is a table with the event's attributes, such as position, time and energy, among others. EPIC cameras are not only sensitive to X-ray photons but also to infrared, visible and ultra-violet light. The cameras include blocking filters to reduce the contamination of the X-ray signal by those photons.

3.2.2. EPIC BACKGROUND

The EPIC cameras are affected by different sources of background. The background effect in the detectors can be divided into three categories (see XMM Users Handbook 2010):

- the cosmic X-ray background;
- the particle X-ray background;
- the instrumental background.

The cosmic X-ray background consists of photons from astrophysical sources and is dominated by thermal emission at lower energies (< 1 keV) and a power law at higher energies (primarily from unresolved cosmological sources). This background varies over the sky at lower energies. Solar wind charge exchange can also contribute to the cosmic X-ray background. The particle X-ray background consists of soft proton flares from the Sun, with spectral variations from flare to flare, and internal (cosmic-ray induced) background, created directly by particles penetrating the CCDs, and indirectly by the fluorescence of satellite material to which the detectors are exposed. The instrumental background consists of electronic noise, it is a detector noise component, such as bright pixels and readout noise.

3.3. *Swift* GAMMA RAY BURST EXPLORER

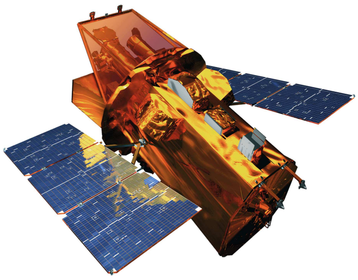

Figure 3.3: Artistic impression of the *Swift* spacecraft.

Swift is a NASA Midex (medium-class Explorer) mission. It was launched on November 20, 2004.The *Swift* Gamma Ray Burst Explorer is a three-telescope space observatory for studying gamma-ray bursts (GRBs) and monitoring the afterglow in X-ray, and UV/Visible light at the location of a burst. To maximise its scientific potential it has rapid-response capabilities and is equipped with three telescopes that cover the γ-ray, X-ray and UV/optical energy range:

- Burst Alert Telescope (BAT, Barthelmy et al. 2005).
- X-ray Telescope (XRT, Burrows et al. 2005).
- Ultraviolet/Optical Telescope (UVOT, Roming et al. 2005).

Swift is engineered to rapidly slew to a burst as soon as a GRB is detected by the BAT, and can place the GRB in the field of view (FOV) of the XRT and UVOT within 100 s.

3.3.1. *Swift*/BAT

The BAT is designed to cover the prompt emission from GRBs over the whole sky. With a large field of view (1.4 sr) and a quick slew time, it can detect the position of GRBs in the sky with an accuracy of $1-4'$ in 15 seconds. The BAT works in the energy band from 15 keV to 150 keV and it uses a coded-aperture mask composed of $\sim$ 54000 lead tiles, of dimensions $5 \times 5 \times 1$ mm, which is mounted on a 5 cm thick composite honeycomb panel and placed 1 meter above the detector plane. The 12×0.6 m sensitive area of the BAT detector plane is formed by 32768 pieces of $4 \times 4 \times 2$ mm CdZnTe (CZT). Groups of 128 detector elements are collected into 8×16 arrays, each one of which is connected to 128-channel readout Application Specific Integrated Circuits (ASICs). The detector modules, which contain each two such arrays, are further grouped in blocks of eight. The hierarchical structure, together with the coded-aperture technique, allows the possibility of losing individual pixels, individual detector modules and even whole blocks without losing the ability to detect GRBs and determine positions.

3.3.2. *Swift*/XRT

The *Swift*/XRT is composed of a grazing incidence Wolter Type I X-ray telescope with 12 nested mirrors, which are made to focus on single MOS charge-coupled device (CCD), similar to those on the XMM-Newton EPIC MOS cameras(see Section 3.2). It has an effective area of 110 cm^2, $23.6' \times 23.6'$ field of view, $18''$ resolution and a $0.2-10$ keV energy range. The X-ray telescope can acquire fluxes, perform spectral analysis and produce light curves of GRBs and their afterglow, covering a dynamic range that spans over seven orders of magnitude.

3.3.3. *Swift*/UVOT

The UVOT is a 30 cm modified Ritchey-Chrétien reflector with two microchannel plate intensified CCD detectors that are modelled on the Optical Monitor on-board *XMM-Newton* (see Section 3.2). They are photon counting devices that are capable of detecting very low signal levels, unaffected by CCD read-out noise and cosmic ray events. The UVOT contains three optical and three ultra-violet (UV) lenticular filters that cover the wavelength range 1600 Å – 6000 Å, a white band filter that has a good response ranging from 1600 Å – 8000 Å, and a blocked filter. The instrument also has a visible grism and a UV grism, which provide low-resolution spectra ($\lambda/d\lambda \sim 75$) in the 2800 Å – 5200 Å and 1600 Å – 2900 Å energy range, respectively, for sources that are brighter than 17 mag for the optical and 15 mag for the UV.

3.4. *NuSTAR*: THE NUCLEAR SPECTROSCOPIC TELESCOPE ARRAY

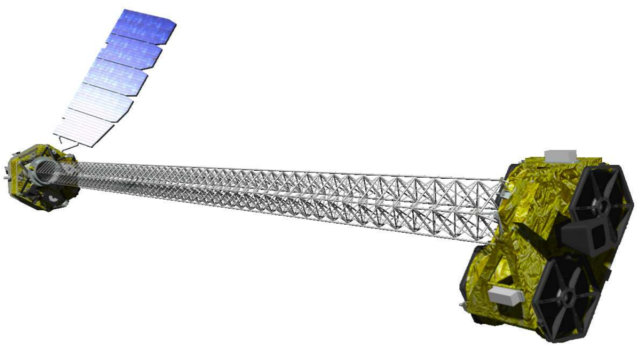

Figure 3.4: Diagram of the observatory in the deployed configuration (Harrison et al., 2013) .

The Nuclear Spectroscopic Telescope ARray (*NuSTAR*) is a NASA Small Explorer mission carrying the first focusing hard X-ray telescope (3-80 keV) to orbit. *NuSTAR* was launched on June 13, 2012 from the Reagan Test Site on the Kwajalein Atoll in the South Pacific in a compact, stowed configuration on a Pegasus XL vehicle.

NuSTAR has an order of magnitude better angular resolution, and it is two orders of magnitude more sensitive than any existing hard X-ray instrument operating in the same energy band (see Table 3.1, Figure 3.5).

NuSTAR consists of two co-aligned hard X-ray telescopes which are pointed at celestial targets by a three-axis-stabilized spacecraft. The *NuSTAR* telescope consists of three main parts:

- the optics, or mirrors, which focus the light;
- the detectors, which record the image;
- an extendible mast, which holds the optics and detectors at the required 10 meters separation distance once in orbit.

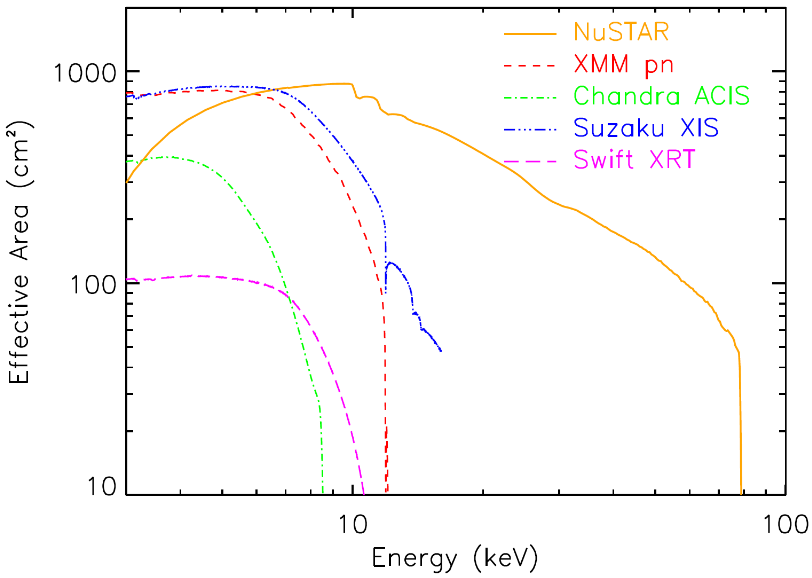

Figure 3.5: *NuSTAR* effective area in comparison with operating focusing telescopes (from Harrison et al. 2013). *NuSTAR* utilizes a low graze angle design with depth-graded multilayer coatings to extend the sensitivity to 80 keV. The sharp cutoff at 80 keV is caused by a K-shell absorption edge in platinum used in the coatings.

3.4.1. OPTICS

NuSTAR has two optics units aligned to look at the same location in the sky. The two sets of images are added together on the ground to see fainter objects. *NuSTAR* employs low grazing angle focusing optics which are conical approximations to the Wolter-I design (Hailey et al., 2010). Each of the two optics modules on board the spacecraft has 133 concentric, confocal shells with a focal length of 10.15 m. The optics have an angular resolution of ~ 12" (FWHM), and a field of view of ~ 10'. The reflectivity of optics

Table 3.1: Some currently operating X-ray telescopes compared to *NuSTAR*

Telescope	Detector	Energy range (keV)	Energy resolution (keV)[a]	Optics type	Effective area (cm^2)	Angular resolution (FWHM)	Field of view	Launch	Ref
Chandra ACIS	CCD	0.1-10	0.13	Focusing	235	1"	17'	1999	1
XMM-Newton EPIC PN	CCD	0.2-12	0.13	Focusing	851	~6"	30'	1999	1
Integral IBIS/ISGRI	CdTe	15-1000	9% (100 keV)	Coded Aperture	~2600	12'	19° [b]	2002	2
Swift BAT	CdZnTe[⋆]	15-150	7	Coded Aperture	5240	17'	14 sr[c]	2002	3
Sukaku XIS	CCD	0.2-12	0.12	Focusing	1000	<1.5"	19'	2005	1
Sukaku HXD	PIN diodes	10-60	3	Collimators	40	4'	34'	2005	4
NuSTAR	CdZnTe[⋆]	6-80	1	Focusing	920	10"	13'	2012	5

Notes. References: 1. `https://heasarc.nasa.gov/docs/heasarc/missions/comparison.html` ; 2. Ubertini et al. 2003; 3. Barthelmy et al. 2005; 4. Takahashi et al. 2007; 5. Harrison et al. 2010.

[⋆] Cadmium Zinc Telluride (CdZnTe) detectors.

[a] Energy resolution at 6 keV for soft X-ray instruments and 60 keV for hard X-ray instruments.

[b] Partially coded FOV. Fully coded field is 9°.

[c] Half coded field. 1.4 sr = 4600 sq. deg.

shells starts decreasing with increasing angle of incidence of photons. This effect is more pronounced at higher energies and the field of view drops to 6' at 60 keV.

3.4.2. DETECTORS

To register the image focused by the optics, *NuSTAR* requires high-energy X-ray detectors capable of measuring the position and energy of the incoming X-rays. in this case, the detectors are called focal-plane detectors because they reside where light from the telescope is focused. Each telescope has a corresponding Focal Plane Module (FPM) consisting of four 32×32 pixel Cadmium Zinc Telluride (CdZnTe) detectors surrounded by a Cesium Iodide (CsI) anti-coincidence shield. These detectors have energy resolution of ~1% and high quantum efficiency over the entire *NuSTAR* energy range.

3.4.3. THE MAST

Bridging the mirrors and the detectors is a mast, a little over 10 meters long. Because hard X-rays graze off the mirrors at nearly parallel angles, hard X-ray telescopes require long focal lengths (the distance between the optics and the detectors, or focal plane). The mast is of low weight, compact and provides a stiff and stable structure connecting the precisely aligned benches.

4

Broadband X-ray spectral analysis of the Seyfert 1 galaxy GRS 1734-292

> "The cosmos is within us. We are made of star-stuff. We are a way for the universe to know itself."
>
> Carl Sagan

In this chapter I will discuss the broadband X-ray spectrum of GRS 1734-292 obtained from non-simultaneous *XMM-Newton* and *NuSTAR* observations, performed in 2009 and 2014, respectively.

4.1. Introduction

As we said in previous chapter (see Sect. 2.2), the primary X-ray emission in Active Galactic Nuclei (AGN) is believed to be produced in a compact hot region, located close to the supermassive black hole, and composed of a plasma of hot electrons: the corona (see Sect. 2.4).

Pre-*NuSTAR* (*Nuclear Spectroscopic Telescope Array*: Harrison et al. 2010) measurements of cutoff energies ranged between 50 and 300 keV (e.g. Dadina 2007, Perola et al. 2002, Malizia et al. 2014). *NuSTAR*'s high sensitivity in hard X-rays, allowing for the first time source-dominated observations of Seyfert galaxies above 10 keV, has recently led to high-energy cutoff measurements from 100 keV to more than 350 keV for several nearby Seyfert galaxies (see: Brenneman et al. 2014; Marinucci et al. 2014a; Ballantyne et al. 2014, Matt et al. 2015), plus a number of significant lower limits (Fabian et al. (2015)).

The nearby (z = 0.0214, corresponding to a distance of 87 Mpc) Seyfert Galaxy GRS 1734-292 is a good candidate for such measurements. With an X-ray luminosity approaching $\sim 10^{44}$ erg s^{-1} in the 0.5-4.5 keV energy band (Marti et al. (1998)), it is one of the most luminous AGNs within 100 Mpc (Piccinotti et al. 1982; Sazonov et al. 2004).

4.2. THE BRIGHT SEYFERT 1 GALAXY: GRS 1734-292

GRS 1734-292 was originally discovered by the ART-P telescope aboard the *GRANAT* satellite (Pavlinsky et al., 1992) and is located only 1.8° from the Galactic Centre. The spectrum between 4 – 20 keV was well described by a power-law with a photon index $\Gamma \sim 2$ and a total hydrogen column density in excess of 10^{22} cm^{-2}. These characteristics, with the inferred X-ray luminosity $\sim 10^{36}$erg s^{-1} assuming the Galactic Center distance, were consistent with the source being a Galactic X-ray binary. Marti et al. (1998) revealed that the optical spectrum of GRS 1734-292 is dominated by strong and very broad emission from blended H and [N II]lines, but also other emission lines, such as O I, [O II]and [S I], all at a redshift of 0.0214. Moreover, the radio, infra-red and optical counterparts of GRS 1734-292 are all consistent with a Seyfert 1 galaxy. In particular, the radio counterpart is a double-sided synchrotron jet of 5 arcsec extent. At the distance of 87 Mpc, this corresponds to a size of 2 kpc. With a radio luminosity of $L_{\rm rad} \simeq 7\times10^{39}$erg s^{-1} in the 0.1 – 100 GHz band and an X-ray luminosity $L_X \simeq 1\times10^{44}$ erg s^{-1} in the 0.5 – 4.5 keV band, GRS 1734-292 is a radio-quiet AGN (Laor & Behar, 2008).

The hard X-ray spectrum of GRS 1734-292 was measured for the first time with the IBIS telescope onboard the *INTEGRAL* observatory (Sazonov et al., 2004). Afterwards it was also analyzed by Molina et al. (2013). The composite X-ray (2 – 200 keV) spectrum with the *ASCA*/GIS observation at 2 – 10 keV (Sakano et al., 2002) is typical of Seyfert galaxies, well described by a power-law of $\Gamma \sim 1.8$ modified by Compton reflection at 10 – 100 keV and an exponential cutoff at $E_{\rm c} > 100-200$ keV.

GRS 1734-292 was detected also in 70 months of observations by the BAT hard X-ray detector (Barthelmy et al., 2005) on the *Swift* gamma-ray burst observatory (Gehrels et al., 2004). The spectral analysis (Baumgartner et al., 2001) showed a power law with a photon index $\Gamma \sim 2.18 \pm 0.07$ and a luminosity of L$\sim 1-2\times10^{44}$ erg s^{-1} in the 14 – 195 keV band.

Guainazzi et al. (2011) analyzed the *XMM-Newton* observation in their GREDOS (General Relativity Effects Detected in Obscured Sources) sample and found that the spectrum is well described by a power-law with a rather flat spectral index $\Gamma = 1.41^{+0.01}_{-0.02}$. They found a hydrogen column density of $N_{\rm H} = 1.41 \pm 0.02 \times 10^{22}$cm^{-2}. From the spectral analysis of the simultaneous *XMM-Newton* and *INTEGRAL*/IBIS-*Swift*/BAT observations, Malizia et al. (2014) found a primary continuum with a power-law index $\Gamma = 1.55^{+0.15}_{-0.08}$ and a cutoff energy $E_c = 58^{+24}_{-7}$ keV.

This work focuses on investigating the broad band X-ray spectrum of GRS 1734-292 and in particular the physical properties of the corona. In Sect.4.3 we discuss the *XMM-Newton* and *NuSTAR* observations and data reduction. In Sect.4.4 we present a reanalysis of the 2009 *XMM-Newton* observation together with a new *NuSTAR* observation of GRS 1734-292. We discuss our results and summarize our conclusions in Sect.4.6. In Section 4.5, a measure of the width of the broad Hα λ6563 component, to infer the black hole mass via an updated virial-based, single-epoch relation, is presented.

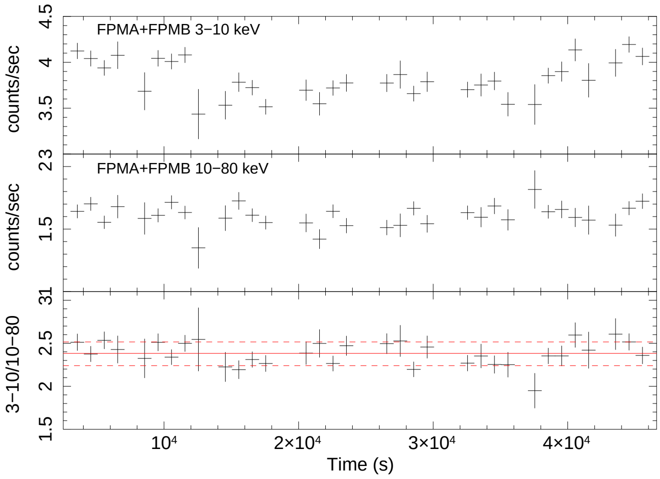

Figure 4.1: Top panel: *NuSTAR* FPMA+B light curve in the 3-10 keV energy band; middle panel: *NuSTAR* FPMA+B light curve in the 10-80 keV energy band; bottom panel: ratio between 3-10 keV and 10-80 keV *NuSTAR* light curves, the red solid and dashed lines indicate the mean and standard deviation, respectively.

4.3. OBSERVATIONS & DATA REDUCTION

GRS 1734-292 was observed by *NuSTAR* with its two coaligned X-ray telescopes Focal Plane Modules A and B (FPMA and FPMB, respectively) on 2014 September 16, for a total elapsed time of 43 ks.

GRS 1734-292 was also observed with *XMM-Newton* on 2009 February 26 with the EPIC CCD cameras, for a total exposure time of 18 ks.

4.3.1. *NuSTAR*

The Level 1 data products were processed with the *NuSTAR* Data Analysis Software (NuSTARDAS) package (v. 1.3.0). Cleaned event files (level 2 data products) were produced and calibrated using standard filtering criteria with the NUPIPELINE task and the latest calibration files available in the *NuSTAR* calibration database (CALDB 20150316). The

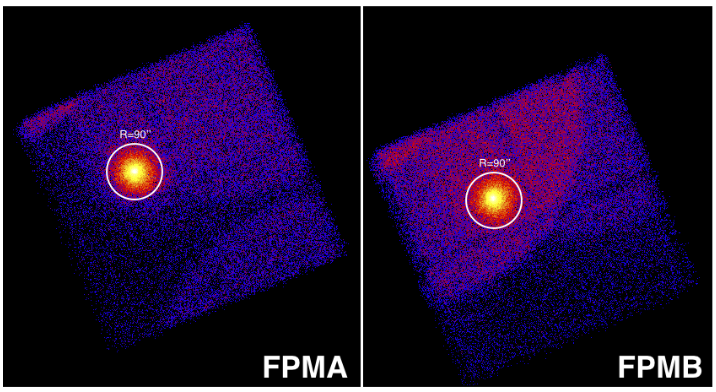

Figure 4.2: X-ray images from the *NuSTAR* FPMA (left panel) and FPMB (right panel).

extraction radii of the circular region for source and background spectra were 1.5 arcmin each; there is no other bright X-ray source within 1.5 arcmin from GRS 1734 and no other sources were present in the background region (see Figure 4.2). The net exposure times after this process were 20.3 ks for both FPMA and B. The two spectra were binned in order to over-sample the instrumental resolution by at least a factor of 2.5 and to have a Signal-to-Noise Ratio (SNR) greater than 3 in each spectral channel. Since no spectral variation (less than 10%) is found in the ratio between the $3-10$ and $10-80$ keV count rates (see Figure 4.1) we decided to use time-averaged spectra.

Since GRS 1734-292 lies very low on the galactic plane, the *NuSTAR* observation is moderately affected by stray light, due to sources off the field of view. This effect is more significant in the FPMB detector: a $50\pm2\%$ increase in the background count rate is observed below 7 keV, with respect to the FPMA. We tried to extract the background spectra from different regions and no differences are found. Since the point source fall within the stray light region in both the detectors and the background is hence properly subtracted, this effect is not relevant to our data analysis. As a last check, we verified that no spectral difference arises between the two *NuSTAR* background subtracted spectra: they perfectly agree within cross-calibration uncertainties.

4.3.2. *XMM-Newton*

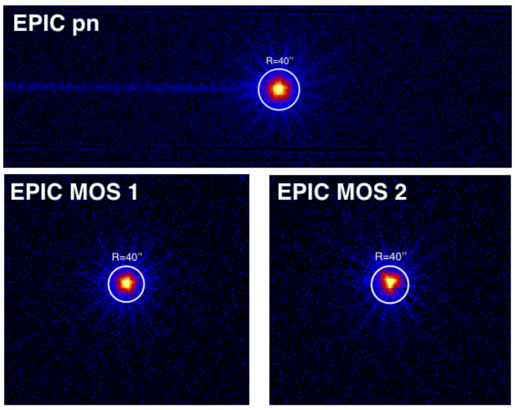

Figure 4.3: X-ray images from the *XMM-Newton* EPIC pn camera (top panel) and the two EPIC MOS cameras (bottom panel).

The *XMM-Newton* EPIC CCD cameras are comprised of the pn detector (Strüder et al. (2001)) and the two MOS units (Turner et al., 2001). During the observation of the source, the camera was operated in large window and thin filter mode, for a total elapsed time of 18 ks. The extraction radii and the optimal time cuts for flaring particle background were computed with SAS 15 (Gabriel et al., 2004) via an iterative process which maximizes the SNR, similar to the approach described in Piconcelli et al. (2004). The resulting optimal extraction radius was 40 arcsec and the background spectra were extracted from source-free circular regions with radii of ~ 50 arcsec for both the EPIC and the two MOS (see Figure 4.3). EPIC spectra had a net exposure time of 13 ks, the MOS spectra had both a net exposure time of 15 ks. EPIC and MOS spectra were binned in order to over-sample the instrumental resolution by at least a factor of three and to have no less than 30 counts in each background-subtracted spectral channel. Data from the MOS detectors are not included in our analysis unless stated otherwise due to the lower statistics of the spectra.

4.4. SPECTRAL ANALYSIS

The spectral analysis has been performed with the XSPEC 12.9.0 software package (Arnaud, 1996). The errors correspond to the 90% confidence level for one interesting parameter ($\Delta\chi^2 = 2.7$), if not stated otherwise. The cosmological parameters $H_0 = 70$ km s^{-1} Mpc^{-1}, $\Omega_\Lambda = 0.73$ and $\Omega_m = 0.27$ are adopted.

4.4.1. RE-ANALYSIS OF THE *XMM-Newton* DATA

We started our data analysis by fitting the 0.5 – 10 keV *XMM-Newton* spectrum with a model [1] composed of a power law absorbed by the Galactic column density $N_H = 7.57 \times 10^{21}$ cm^{-2}, as derived from HI maps (Kalberla et al., 2005), and an additional intrinsic absorber at the redshift of the source, found to have a column density of $0.84 \pm 0.03 \times 10^{22}$ cm^{-2}. This yielded a poor fit with $\chi^2 = 242$ for 163 degrees of freedom (d.o.f.). The data reveal a slight excess at energies < 1 keV; we assumed that the soft excess is produced by a collisional plasma (with solar abundances) and we tried to reproduce it with a thermal model (MEKAL),[2]) absorbed by the Galactic column density. The χ^2 is 209 for 161 d.o.f. for a thermal plasma temperature of $kT = 0.14^{+0.22}_{-0.05}$ keV and a 0.5-2 keV luminosity of $\sim 2.7 \pm 0.7 \times 10^{42}$ erg s^{-1}. Some residuals are however evident around 6 – 7.5 keV (see Figure 4.4).

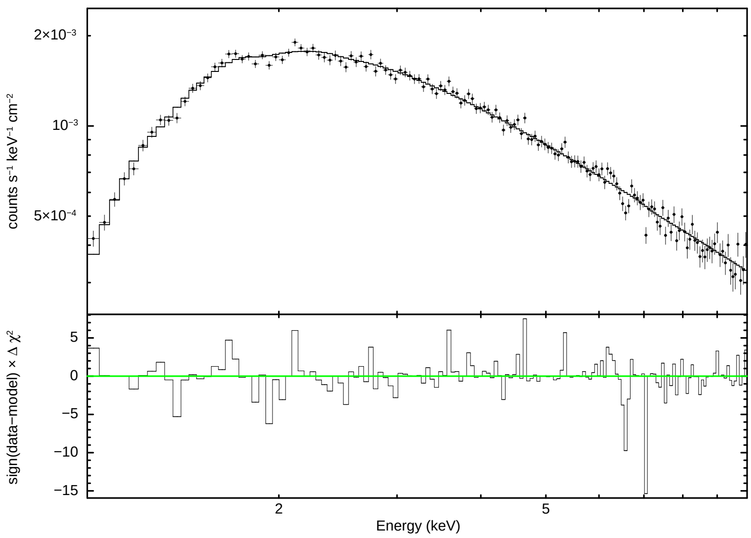

Figure 4.4: Data and residuals for the *XMM-Newton* spectrum when no Gaussian lines are included in the model.

Therefore we added a narrow Gaussian line[3] at 6.4 keV, corresponding to the neutral iron Kα emission line, which is a typical feature in Seyfert galaxies (Nandra & Pounds,

[1] XSPEC model: TBabs * zwabs * powerlaw
[2] XSPEC model: TBabs * (mekal + zwabs * powerlaw)
[3] XSPEC model: TBabs * (mekal + zwabs * (zgauss + powerlaw))

1994). We found the centroid value of the line to be 6.36 ± 0.07 keV and the fit slightly improved: $\chi^2 = 202$ for 159 d.o.f., with a null hypothesis probability of 4.7×10^{-2} according to the F-test. The iron Kα emission line shows a flux of $1.4 \pm 0.8 \times 10^{-5}$ ph cm^{-2} s^{-1} and an equivalent width of 20 ± 13 eV. We then added an absorption Gaussian line[4], suggested by the presence of negative residuals around 6.7 keV. We found a centroid value for this line of 6.69 ± 0.05 keV; the χ^2 is 187 for 157 d.o.f., with a null hypothesis probability of 1.5×10^{-3} according to the F-test [5]. The flux and the line equivalent width of this absorption line were $2.1 \pm 0.8 \times 10^{-5}$ ph cm^{-2} s^{-1} and 31 ± 12 eV, respectively. The centroid energy of this absorption line is consistent with the energy expected for the K-shell transition of FeXXV ions produced by Compton-thin material. We tried to fit this component with a warm-absorber (WA) model[6], using an ad-hoc table produced with the photo-ionization code CLOUDY C13.03 (most recently described by Ferland et al. (2013)). We found a ionization parameter of $\xi_i = 1778.3^{+2.7}_{-1.6}$ erg cm s^{-1} and a column density $N_{\rm H} = 5.01 \pm 3.2 \times 10^{22}$ cm^{-2}. The χ^2 is 186 for 157 d.o.f.. Further residuals around 7.2 keV suggested to add another Gaussian absorption line[7]. The inclusion of this component leads to a χ^2/d.o.f.= 178/155 = 1.14 (F-test null hypothesis probability 2.2×10^{-2}). The fit gives a centroid energy of $7.19^{+0.07}_{-0.09}$ keV, with a flux of $1.3 \pm 0.8 \times 10^{-5}$ ph cm^{-2} s^{-1} and a line equivalent width (EW) of 28 ± 14 eV. An absorption line with this centroid energy is possibly a blue-shifted line associated with the transition of FeXXVI ions (rest frame energy: 6.966 keV) produced by a material with a velocity of 9500 km s^{-1} $\simeq 0.03$c. This is the lower limit of the range of velocities for Ultra-Fast Outflows (Tombesi et al., 2013). To verify the presence of this line we fitted the pn and the MOS spectra simultaneously with the same model. We tied all of the MOS parameters to the pn values. The normalizations of the two Gaussian lines and the normalization of the power-law of the MOS spectra are tied together but are free to vary. The χ^2 of the fit is 461 for 427 degrees of freedom. The fit with the MOS data confirms the presence of the absorption line due to FeXXV Kα ions produced by a warm absorber, but not that at 7.2 keV. In fact, the upper limit to the flux of the latter line is 3.16×10^{-6} ph cm^{-2} s^{-1} at 90% confidence level. In the following fits, therefore, this line will not be included.

We found that the photon index of the primary X-ray continuum is $\Gamma = 1.47 \pm 0.03$. This[6] is our best fit and we will use it as the baseline model when adding the *NuSTAR* data.

4.4.2. ADDING *NuSTAR* DATA.

We started the analysis of the 3 – 80 keV *NuSTAR* (FPMA and FPMB) spectra fitting the data together with the *XMM-Newton* best fit found previously. We left all the parame-

[4] XSPEC model: TBabs*(mekal + zwabs*(zgauss + zgauss + powerlaw))

[5] In principle, the F-test is not a reliable test for the significance of emission or absorption lines, but it can be used if their normalizations are allowed to be negative and positive (Protassov et al., 2002).

[6] XSPEC model: TBabs * (mekal + mtable{cloudy.fits} * zwabs * (zgauss + powerlaw))

[7] XSPEC model: TBabs * (mekal + mtable{cloudy.fits} * zwabs * (zgauss + zgauss + powerlaw))

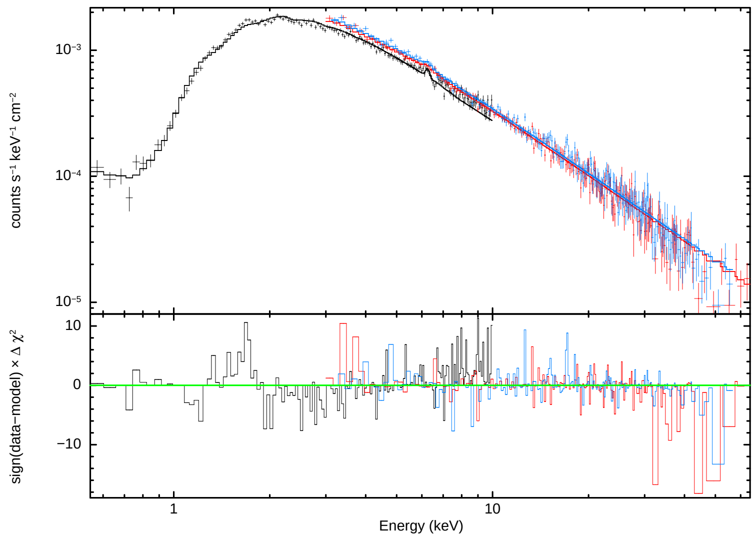

Figure 4.5: Data, fit model (top panel) and residuals (bottom panel) for *XMM-Newton* (black) and *NuSTAR* FPMA (red) and FPMB (in blue) spectra when the parameters are all tied to the best fitting parameters from the *XMM-Newton* spectral fit.

ters, apart from the normalizations of the various components, tied to the *XMM-Newton* best fitting parameters. The *XMM-Newton* and the *NuSTAR* FPMA calibration constants are fixed to 1.0 (given the non-simultaneity of the two observations, any mismatch between the two instruments cannot be separated from intrinsic variations) while we left the *NuSTAR* FPMB cross-calibration constant free to vary. The value found for the constant is 1.004. The χ^2 for this fit is 830 for 544 d.o.f.. The spectral slope shows a different trend for the power-law from the two observations (see Figure 4.5) so we left the two photon indices, which are related to two different observations, free to vary. We kept tied the emission and absorption line centroid energies to the values found by *XMM-Newton* due to the lower spectral resolution of *NuSTAR*. We found that the *NuSTAR* photon index is steeper than the *XMM-Newton* one ($\Gamma = 1.65 \pm 0.05$). The observed mismatch between the two photon indices is larger than the instrumental mismatch. The fit leads to a χ^2/d.o.f.= 662/543 = 1.22. Re-analyzing *Swift* /BAT observation from the *Swift* BAT 70-Month Hard X-ray Survey (NASA's Archive of Data on Energetic Phenomena[8]), we found a photon index $\Gamma = 2.18 \pm 0.07$ consistent with Baumgartner et al. (2001). Adding a high energy cutoff, however, we found a flatter photon index $\Gamma = 1.8 \pm 0.3$ and an high energy cutoff value of $E_c = 110^{+300}_{-50}$ keV. The average *Swift*/BAT flux is higher than the *NuSTAR* one, which in turn is higher than *XMM-Newton*'s one. The source therefore show the softer-when-brighter behaviour (**?**, Sobolewska & Papadakis 2009) which is typical for Seyfert Galaxies.

Back to *NuSTAR* data, looking at the residuals above ~ 40 keV (see Figure 4.6) the presence of a high-energy cutoff is suggested, so we replaced the power law component with

[8] https://swift.gsfc.nasa.gov/results/bs70mon/

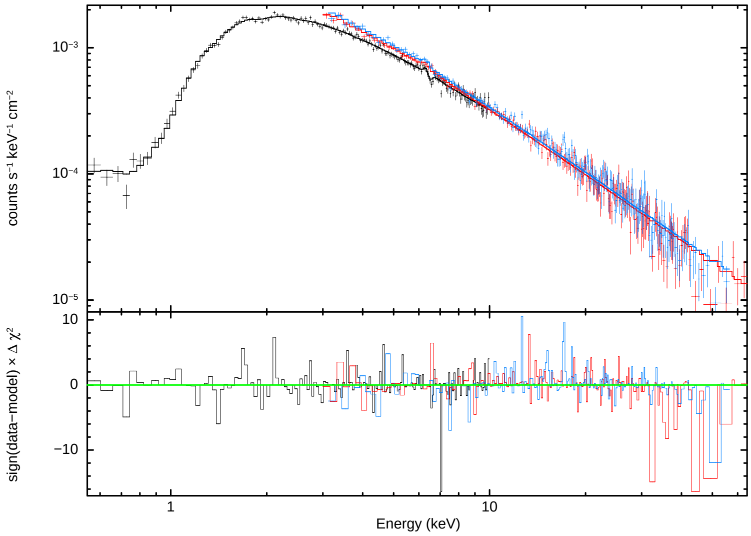

Figure 4.6: Data, fit model (top panel) and residuals (bottom panel) for *XMM-Newton* (black) and *NuSTAR* FPMA (red) and FPMB (blue) spectra when the power law in the model is not corrected by a high energy cutoff. The photon indices of *XMM* and *NuSTAR* are left free to vary.

a power law corrected by a high energy exponential rolloff (CUTOFFPL model in XSPEC)[9]. The fit improved significantly (χ^2/d.o.f.= 556/541 = 1.1); we found for the *NuSTAR* spectra $\Gamma = 1.58 \pm 0.04$ with the cutoff energy $E_c = 60^{+17}_{-9}$ keV and $\Gamma = 1.40^{+0.06}_{-0.09}$ for the *XMM-Newton* spectrum with a lower limit for the cutoff energy at 90 keV.

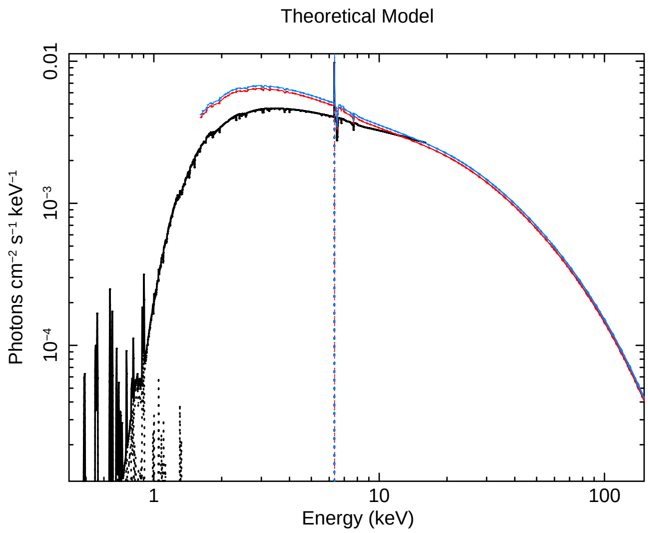

Figure 4.7: Best fitting phenomenological model including the soft excess component, two narrow Gaussian lines, the WA and a cutoff power law reflected from neutral material (PEXRAV model), all absorbed by the Galactic column density and an intrinsic absorber.

We then included a cold reflection component in both the data sets, using the PEXRAV model (Magdziarz & Zdziarski, 1995b) in XSPEC, to test for the presence of a Compton reflection continuum. We fixed all element abundances to solar values and fixed the

[9]XSPEC model: constant * TBabs * (mekal + mtable{cloudy.fits} * zwabs * (zgauss + cutoffpl))

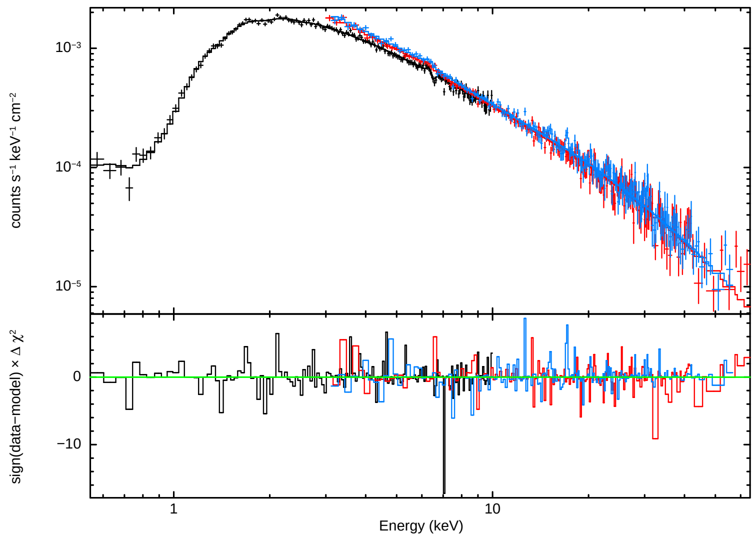

Figure 4.8: Data and best fit model extrapolated from *XMM-Newton* (black) and *NuSTAR* FPMA (red) and FPMB (blue) spectra when model in Figure 4.7 is used; see text for more details. Residuals are shown in lower panel

inclination angle to the default value ($\cos i = 0.45$, $i \sim 60°$). Because in the previous fit we found only a lower limit to the high-energy cutoff in the *XMM-Newton* spectrum, for the sake of simplicity we fixed it to 1 MeV. The model used in the fit is shown in Figure 4.7. Data and residuals are shown in Figure 4.8, while the best fitting parameters are shown in Table 4.1. The photon index and high energy cutoff are now $\Gamma = 1.65 \pm 0.05$ and $E_c = 53^{+11}_{-8}$ keV. The reflection fraction R is 0.48 ± 0.22. In the left panel of Figure 4.9 the contour plot of the cutoff energy versus the photon index of the power law for the *NuSTAR* observation is shown, while in the right panel we show the contour plot of the high energy cutoff versus the reflection fraction.

The fit shows a weaker iron line with respect to what we expected from the Compton hump. Replacing the PEXRAV model with a self-consistent model that includes the Fe Kα line, such as the PEXMON model[10] (Nandra et al., 2007), with the relative iron abundance left free to vary, a value of 0.6 ± 0.3 is found for this parameter (χ^2=585 for 542 d.o.f.)

In order to test for the presence of a relativistic component, we fitted the data with the RELXILL model[11] (García et al., 2014). Since the black hole spin parameter was not constrained, we assumed $a = 0.998$. We fixed the reflection fraction parameter to the best fit values found with the previous best fit model (see Table 4.1). Including the relativistic effects provides no improvement in the fit, implying that no relativistic component is required by the data.

[10] XSPEC model: constant * TBabs * (mekal + mtable{cloudy.fits} * zwabs * pexmon)
[11] XSPEC model: constant * TBabs * (mekal + mtable{cloudy.fits} * zwabs * relxill)

Table 4.1: Best fitting parameters for the phenomenological model including PEXRAV and two Gaussian lines (line 1 at 6.4 keV and line 2 at 6.68 keV, obtained from the *XMM-Newton* spectrum). Errors are at 90% confidence levels. The χ^2 / d.o.f. value is 580/540 = 1.07.

Parameter	*XMM-Newton*	*NuSTAR*
$N_H (10^{22} cm^{-2})$	0.88 ± 0.05	0.88^{**}
Γ	$1.47^{+0.07}_{-0.03}$	1.65 ± 0.05
E_c (keV)	1000^*	53^{+11}_{-8}
R	< 0.6	0.48 ± 0.22
F_{2-10} (10^{-11} erg cm^{-2} s^{-1})	$5.12^{+0.15}_{-0.08}$	$6.62^{+0.02}_{-0.08}$
L_{2-10} (10^{43} erg s^{-1})	5.23 ± 0.03	6.67 ± 0.04
F_{10-80} (10^{-10} erg cm^{-2} s^{-1})	-	1.25 ± 0.01
L_{10-80} (10^{44} erg s^{-1})	-	1.29 ± 0.05
$F_1 (10^{-5}$ ph/cm^2/s)	1.37 ± 0.84	3.93 ± 1.91
EW$_1$ (eV)	20 ± 13	50 ± 31
$F_2 (10^{-5}$ ph/cm^2/s)	-2.06 ± 0.77	0.75 ± 1.86
EW$_2$ (eV)	-31 ± 12	-28 EW$_2 < 0$

* fixed parameter.
** tied parameter.

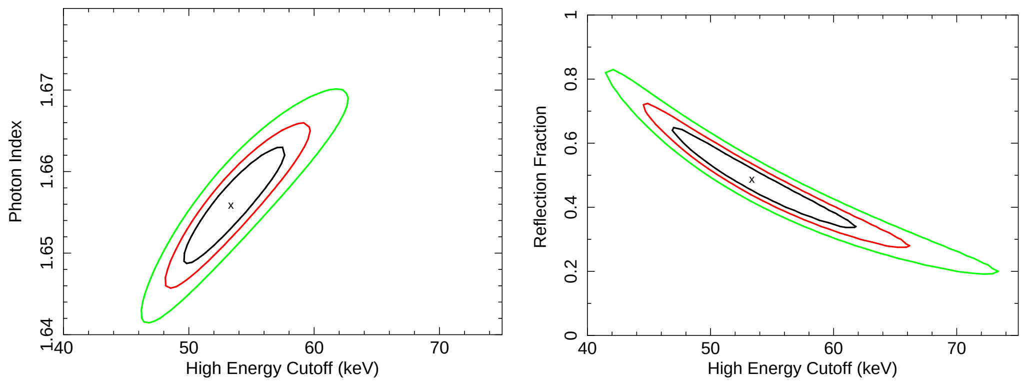

Figure 4.9: E_c-Γ contour plot (left panel) and E_c-R contour plot (right panel) for the *NuSTAR* observation. The solid black, red and green curves refer to the 68, 90 and 99% confidence levels, respectively. The X represents the best fit value of the parameters.

4.4.3. COMPTONIZATION FEATURES

Finally, assuming that the primary emission is due to Comptonization of thermal disc photons in a hot corona, we estimated the coronal parameters using an analytical Comptonization model. The temperature is expected to be related to the cutoff energy by $E_c = 2-3 \times kT_e$ (Petrucci et al. 2000, Petrucci et al. 2001), so, for such a low value of the cutoff energy (53^{+11}_{-8} keV), we expect a low value for the coronal temperature, and a high value for the optical depth to account for the flat spectrum. We fitted the *NuSTAR* spectra with the COMPTT model (Titarchuk, 1994), adding the reflection component computed by PEXRAV with two Gaussian lines[12](the iron Kαemission line and the absorption line due to FeXXV Kα ions). Because of the low *NuSTAR* spectral resolution we fixed the centroid energies of the lines to the values found in the best fit of the *XMM-Newton* data. In this model the seed photon spectrum is a Wien law; we fixed the temperature to the

[12] XSPEC model: constant * TBabs * zwabs * (COMPTT + zgauss + zgauss + pexrav)

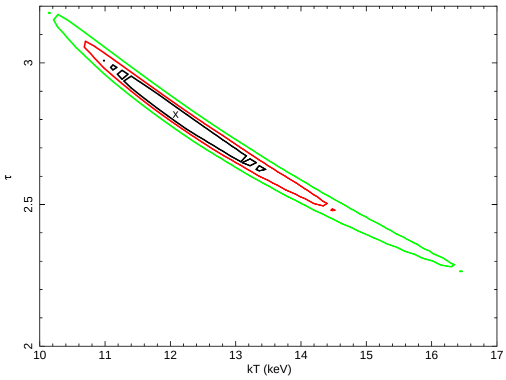

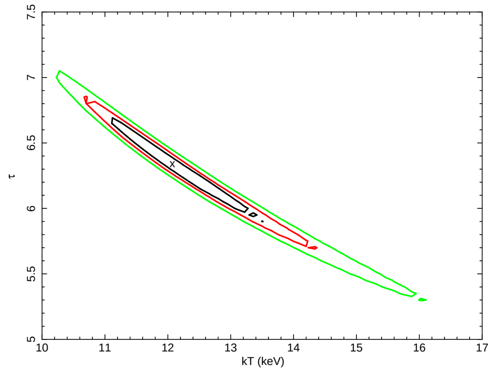

Figure 4.10: Coronal temperature vs optical depth contour plot in the case of slab geometry (left panel) and spherical geometry (right panel) for the *NuSTAR* observation when the COMPTT model is used to fit the data. The solid black, red and green curves refer to the 68, 90 and 99% confidence levels respectively. The X represents the best fit value of the parameters.

maximum temperature of the accretion disc, which in this case, for Shakura & Sunyaev (1973) disc is 4 eV, given the black hole mass of $\sim 3\times10^8$ solar masses (see Sec. 4.5). In the case of a slab geometry of the corona, we found a coronal temperature $kT_e = 12.1^{+1.8}_{-1.2}$ keV and an optical depth $\tau = 2.8^{+0.2}_{-0.3}$. The fit is good, with a χ^2 of 411 for 383 d.o.f.. For the case of a spherical geometry, we found a statistically equivalent fit. The value of the coronal temperature is about the same, while the optical depth is higher by almost a factor of two: $\tau = 6.3^{+0.4}_{-0.5}$. The difference is primarily due to the different meaning of this parameter in the two geometries: the optical depth for a slab geometry is the average of optical depth values along the different directions, so it is lower than the effective value, while that for a sphere is the radial one (see Titarchuk 1994 for a more detailed description). The contour plots of the coronal temperature versus the optical depth obtained with the two different geometries are shown in Figure 4.10.

We did not try to fit the Comptonization with the COMPPS model because the optical depth values obtained with the COMPTT model are too high and they do not fall within the region of parameter space where the numerical COMPPS method produces reasonable results (see Poutanen & Svensson 1996a for more details).

4.5. THE BLACK HOLE MASS ESTIMATE

The spectroscopic observation of the optical counterpart of GRS 1734-292 was carried out with the EFOSC2 instrument mounted on the 3.6m ESO-NTT telescope at La Silla, on 2010-07-08 (program ID:085.D-0441(C), PI: Jonker), using GRISM 13 and a 1” slit. The pointing is 500 s long and we used IRAF (version 2.16) and MIDAS (release 15SEPpl1.0) for data reduction and calibration, using standard procedures.

The aim of our analysis was to measure the width of the broad H$\alpha\lambda$6563 component, to infer the black hole mass via a virial-based, single-epoch relation (La Franca et al. 2015 and Ricci et al. 2017). In Fig. 4.11 and 4.12 the 4700-7500 Å and 6500-7500 Å spectra of GRS 1734-292, respectively, are shown: several emission lines of H, O, N and S elements

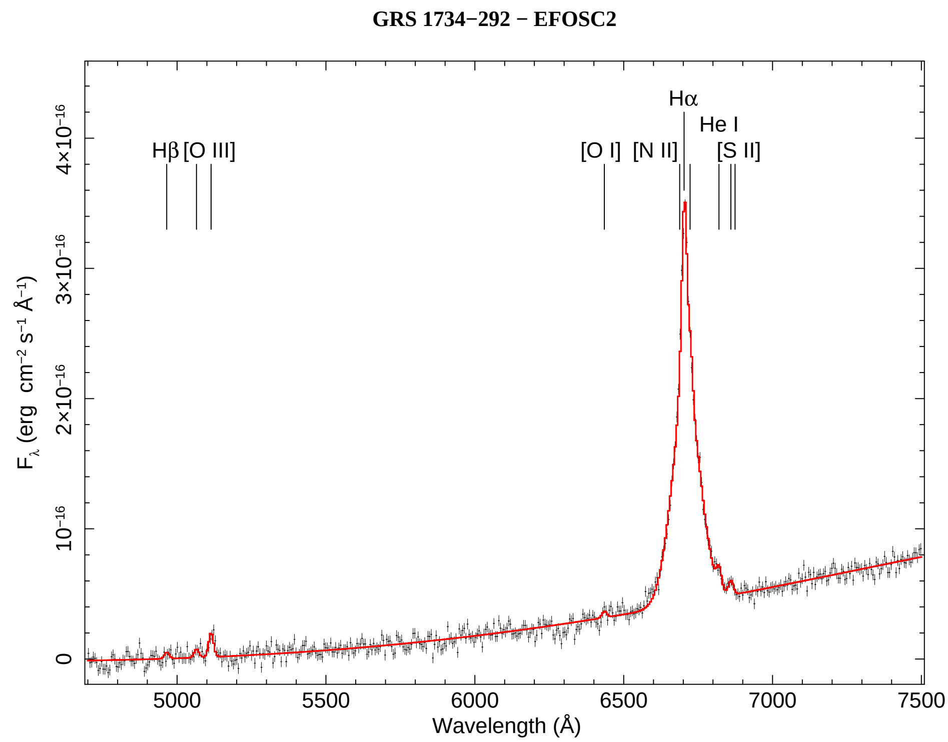

Figure 4.11: ESO-NTT optical spectrum of the source, in the 4700-7500 Å range. Emission lines from several elements such as H, O, N and S are clearly detected.

can be clearly seen. Throughout our analysis we assumed that F([N II] λ6583)/F([N II] λ6548)=3, as required by the ratio of the respective Einstein coefficients. Spectra are fitted with XSPEC, via χ^2 minimization, by modelling the continuum as a power law convolved with a SPLINE function, and each line component as a Gaussian. The width of the narrow lines was fixed to the instrumental one, inferred from fitting the He-Ar calibration lines. We assumed a redshift z=0.0214 (Marti et al., 1998) and all reported wavelenghts in Table 4.2 are rest-frame The inferred fluxes for the Hα (broad component) and Hβ emission lines lead to an observed Hα/Hβ> 12.6. Assuming an average Balmer-line intensity relative to HHβ of 2.86 (case B recombination) we calculate a Galactic extinction in the V band of $A_V > 4.6$ mag. Adopting the standard Galactic gas-to-dust ratio, the optical reddening may be rewritten using the relation $A_V = 5.27 N_H^{22}$ mag, where the absorbing column density is expressed in units of 10^{22} cm^{-2} (see e.g. Maiolino et al. 2001, and references therein). The lower limit obtained with the optical data analysis is in agreement with the absorbing column density measured from the X-ray spectrum.

We measured a FWHM=4940 ± 50 km s^{-1} for the broad component of the Hα line. This value and the 2-10 keV luminosity measured with XMM-*Newton*, which is the closest observation in time ($L_X = 5.23 \pm 0.03 \times 10^{43}$ erg s^{-1}), allow us to use the updated calibrations of the virial black hole mass estimators (Ricci et al., 2017). The inferred mass is $\log(M_{bh}/M_\odot) = 8.5$, with an intrinsic spread of the relation of ~ 0.5 dex.

Table 4.2: Optical emission lines in the ESO-NTT spectrum of GRS 1734-292.

Line (1)	λ (2)	Flux (3)	FWHM (4)
Hβ	4861.33	< 1.5	-
[O III]	4958.92	0.13 ± 0.08	-
[O III]	5006.85	0.38 ± 0.08	-
[O I]	6300.32	0.10 ± 0.08	-
[N II]	6548.06	0.30 ± 0.03	-
Hα Nr.	6562.79	$3.02^{+0.06}_{-0.13}$	-
Hα Br.	6562.79	$19.03^{+0.26}_{-0.20}$	4940 ± 50
[N II]	6583.39	0.90 ± 0.09	-
He I	6678.11	0.3 ± 0.1	-
[S II]	6716.42	0.20 ± 0.07	-
[S II]	6730.78	0.15 ± 0.05	-

Notes. Col. (1) Identification. (2) Laboratory wavelength (Å) (air: Bowen 1960). (3)FWHM in km s^{-1} units. Dashes indicate a fixed FWHM=18 Å. Col (4) Fluxes in 10^{-15} erg cm^{-2} s^{-1} units.

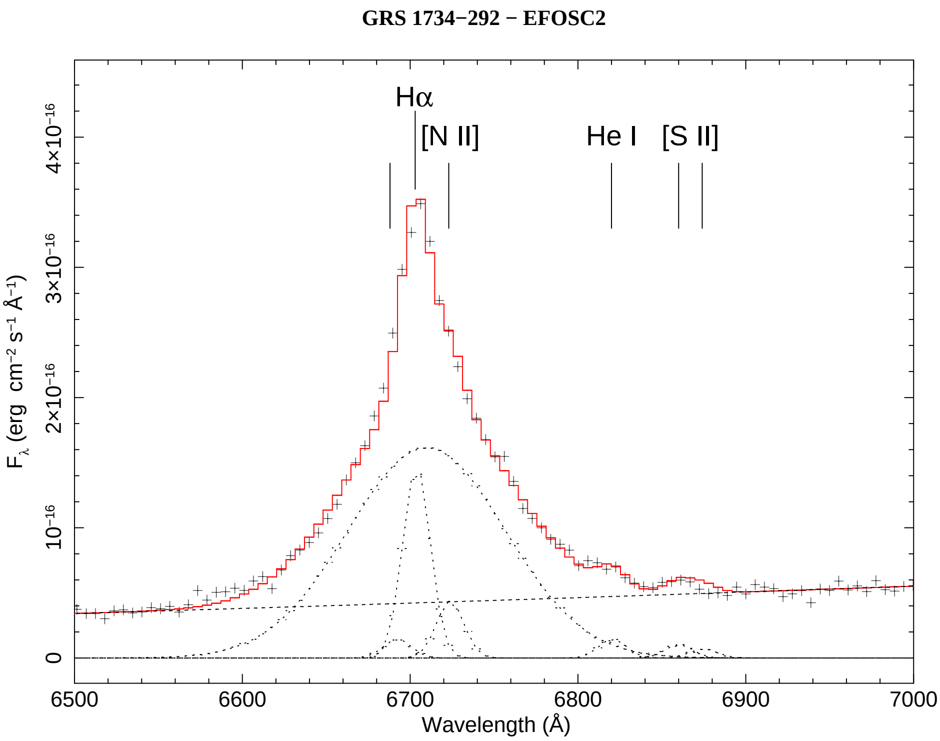

Figure 4.12: ESO-NTT optical spectrum of the source, in the 6500-7500 Årange.

4.6. DISCUSSION AND CONCLUSIONS

We have presented an analysis of non-simultaneous *XMM-Newton* and *NuSTAR* observations of the Seyfert 1 galaxy GRS 1734-292. The spectral slope of the primary power law is different between the two observations, being very flat in the *XMM-Newton* observation ($\Gamma \sim$1.47, consistent with the values found by Guainazzi et al. (2011)) while it is more typical of a Seyfert galaxy in the *NuSTAR* observation ($\Gamma \sim$1.65), when the source was a factor of ~ 1.3 brighter.

The 2 – 10 keV absorption-corrected luminosity from the *XMM-Newton* observation is $L_{2-10keV} = 5.23 \pm 0.03 \times 10^{43}$ erg s^{-1}. Using the 2 – 10 keV bolometric correction of Marconi et al. (2004), we estimate the bolometric luminosity to be $L_{\rm bol} = 1.45 \times 10^{45}$erg s^{-1}. From the bolometric luminosity, with the black hole mass as in Section 4.5, we estimate the $L_{\rm bol}/L_{\rm Edd}$ ratio to be 0.033.

The presence of an iron Kα emission line at 6.4 keV, albeit weak, is confirmed. We found also one absorption line, with a centroid energy at around 6.69 keV, which is consistent with the energy expected for the K-shell transition of FeXXV ions. The cutoff energy is 53^{+11}_{-8} keV, fully consistent with that found by Malizia et al. (2014). This is the lowest value found so far by *NuSTAR* in a Seyfert galaxy together with Mrk 335 (Keek & Ballantyne, 2016); comparable or even lower values are found in stellar-mass accreting black holes (Miller et al. 2013; Miller et al. 2015). We estimated the coronal parameters by fitting the *NuSTAR* data with the COMPTT Comptonization model, finding a coronal temperature of $kT_e = 12.1^{+1.8}_{-1.28}$ keV and an optical depth $\tau = 2.8^{+0.2}_{-0.3}$ assuming a slab geometry or a similar temperature and $\tau = 6.38^{+0.4}_{-0.5}$ assuming a spherical geometry. Of course, we are implicitly assuming a simple picture in which the corona is a single temperature zone, which may not be the case if the heating is localized, as e.g. in the case of magnetic reconnection.

We used these values to put GRS 1734-292 in the compactness-temperature (Θ_e - ℓ) diagram (Fabian et al. (2015), and Sec. 2.4.3). We obtain $\Theta_e = 0.023^{+0.004}_{-0.002}$. To compute the compactness parameter, following Fabian et al. (2015) we adopted the luminosity of the power-law component extrapolated to the 0.1 – 200 keV band; since no measurement exists for the radius, we assume a value of 10 gravitational radii R_g. We found $\ell = 13.3 \pm 0.3(R_{10})^{-1}$ were R_{10} is the ratio between the radius and $10R_g$.

As obvious, given the low coronal temperature, GRS 1734-292 is located far away from the region of pair production in the Θ_e - ℓ plane (see Fig 2.15), and is also located well below the $e^- - e^-$ coupling line (i.e. the line below which the electron-electron coupling time scale is shorter than the Compton cooling time scale). This should ensure that the electron population is thermalized. It is instead located close to the $e^- - p$ coupling line, below which the electron-proton coupling time scale is shorter than the Compton cooling time scale. It is interesting to note that no sources among those analyzed by Fabian et al. (2015) lie definitely below the $e^- - p$ line, while a number of them lie around or just above (see Fig. 4 in their paper). This line therefore seems to set a physical boundary, which may be understood, at least qualitatively. If the electron population cools by

Compton scattering and its temperature decreases until the electron-proton coupling becomes important, the transfer of energy from protons to electrons becomes effective. This is not a completely self-consistent picture, as the electron-proton coupling line was calculated assuming that the electron and proton temperatures (normalized to their mass), Θ_e and Θ_p, are the same (Fabian, 1994), which is unlikely when Compton cooling dominates. Moreover, the dependence of the coupling time on Θ_e is small as soon as the two temperatures are decoupled and the proton temperature is the largest. Time-dependent, detailed calculations with realistic heating and energy redistribution mechanisms are required to assess how effective this feedback may be.

Only a few AGN in the Fabian et al. (2015) compilation have temperatures as low as that of GRS 1734-292, and none among those observed by *NuSTAR*. We note that the accretion rate of GRS 1734-292 is only a few percent of the Eddington limit, so the effectiveness of the cooling mechanism cannot be related to a particularly strong radiation field. It may, however, be at least partly related to the high value of the optical depth τ. A seed photon coming from the disc, in fact, will undergo more than one scattering before leaving the corona, thereby reducing the electron temperature. Indeed, models predict an anti correlation between coronal temperature and optical depth (see e.g. Petrucci et al. 2001 for a calculation based on the two-phase model of Haardt & Maraschi (1993): note that values not too different from ours are predicted). The reason for the unusually large value of the optical depth is unclear (but see Keek & Ballantyne (2016) for evidence of an increase of the optical depth with decreasing Eddington ratio in Mrk 335), and difficult to assess given our poor knowledge of the processes which originate the corona and of the mechanisms which transfer the energy there. But with the increasing amount of high quality spectra from *NuSTAR*, progressively populating this parameter space, it is at least possible to start seriously pondering these questions.

5

NuSTAR spectral analysis of MCG +8-11-11 and NGC 6814

> "Look up at the stars and not down at your feet. Try to make sense of what you see, and wonder about what makes the universe exist. Be curious."
>
> Stephen Hawking

In this chapter I will present the *NuSTAR* observations of MGC +8-11-11 (100 ks) and of NGC 6814 (150 ks), taken almost simultaneously with short *Swift* observations (20 ks each). The main goal of these observations was to investigate the Comptonization mechanisms acting in the innermost regions of AGN which are believed to be responsible for the UV/X-ray emission. The spectroscopic analysis of the *NuSTAR* spectra of these two sources revealed that although they had different properties overall (black hole masses, luminosity and Eddington ratios) they had very similar coronal properties.

In Sect.5.2 the observations and data reduction are presented. In Sect.5.3 we report on the spectral analysis of the two sources. The results are discussed and summarized in Sect.5.4.

5.1. Introduction

The primary X-ray emission of Active Galactic Nuclei (AGN), according to the standard paradigm, is due to thermal Comptonization of the soft disc photons in a hot, optically thin plasma (the so-called corona) located above the accretion disc (see Sect. 2.4). The spectral shape of this component is, in the first approximation, a power law with a cutoff at high energy (see Sect. 2.2.1). The primary emission is reprocessed by circumnuclear material giving rise to a complex spectral shape, that we already described in previous chapters (e.g. Sect.s 2.2.2, 2.2.3).

With the superior sensitivity of *NuSTAR* (*Nuclear Spectroscopic Telescope Array*: Harrison et al. 2013) above 10 keV it is possible to separate the primary and reflected continua and measure the coronal parameters, breaking the degeneracy occurring when the high energy cutoff can not be measured. Indeed, a number of high-energy cutoff measurements in local Seyfert galaxies, on a wide range of Eddington ratios, have been already obtained (Fabian et al. 2015, 2017, Marinucci et al. 2016 and references therein), to investigate the Comptonization mechanisms acting in the innermost regions of AGN and which are believed to be responsible for the X-ray emission. However more and more precise measurements are needed in order to put these studies on a more firm statistical ground and constrain the coronal parameters. NGC 6814 and MCG +8-11-11 are two bright radio quiet unobscured Seyfert 1 galaxies; they are ideal sources for this goal.

MCG +8-11-11 (z = 0.0204) is a very X-ray bright AGN with a black hole mass of $\log \frac{M_{BH}}{M_\odot} = 7.19 \pm 0.02$ (Bian & Zhao, 2003b) (Winter et al., 2010) and X-ray fluxes. measured by *INTEGRAL*, of $F_{20-100\mathrm{keV}} = 8.46 \times 10^{-11}$ erg cm^{-2} s^{-1} and $F_{2-10\mathrm{keV}} = 5.62 \times 10^{-11}$ erg cm^{-2} s^{-1} (Malizia et al., 2012). The $2-10$ keV absorption-corrected luminosity of the source is $6.45 \pm 0.04 \times 10^{43}$ erg s^{-1} (Bianchi et al., 2010). *ASCA* (Grandi et al., 1998) and BeppoSAX (Perola et al., 2000) showed that the spectrum is well fitted by a model composed by a power law, a warm absorber, a Compton reflection component and an FeKα line. The best fit of the *ASCA* and OSSE data was an absorbed power law with spectral index $\Gamma = 1.73 \pm 0.06$ and an exponential cutoff at ~250 keV, plus a reflection component and a cold iron line. Also BeppoSAX data showed the presence of a cutoff at high energy (~ 170 keV). The XMM-*Newton* spectrum (Matt et al., 2006) revealed the lack of a soft excess, a large reflection component and a narrow iron line with a low equivalent width (EW) and no relativistic features. Bianchi et al. (2010) found in the *Suzaku* observation a relativistic Fe Kα line, plus a narrow component with no associated reflection continuum.

NGC 6814 (z = 0.0052, Molina et al. 2009) is a Seyfert 1 Galaxy with black hole mass of $\log \frac{M_{BH}}{M_\odot} = 6.99^{+0.32}_{-0.25}$ (Pancoast et al., 2014, 2015) known to show X-ray variability by at least a factor of 10 over time scales of years (Mukai et al., 2003). It is part of the reverberation mapping campaign "the LAMP project" (Lick AGN Monitoring Project Bentz et al. 2009). The hard and soft X-ray flux of this source is $F_{20-100\mathrm{keV}} = 5.66 \times 10^{-11}$ erg cm^{-2} s^{-1} and $F_{2-10\mathrm{keV}} = 0.17 \times 10^{-11}$ erg cm^{-2} s^{-1} (Malizia et al., 2012).The INTEGRAL spectrum (Malizia et al., 2014) showed that the source has a quite flat spectrum ($\Gamma = 1.68 \pm 0.02$) with an exponential cutoff at $E_c = 190^{+185}_{-66}$ keV. From the XMM-*Newton* observation it is possible to see the presence of a narrow FeKα line (Ricci et al., 2014) with EW=82^{+17}_{-15} eV. The *Suzaku* observation shows significant variability, a primary continuum with a photon index of 1.53 ± 0.02 and no evidence of soft excess. It shows also the emission of the Fe Kα and Fe XXVI lines with centroid energy and EW respectively $E_{\mathrm{FeK}\alpha} = 6.40 \pm 0.03$ keV, $EW_{\mathrm{FeK}\alpha} = 170^{+30}_{-40}$ eV and $E_{\mathrm{FeXXVI}} = 6.94 \pm 0.07$ keV, $EW_{\mathrm{FeXXVI}} = 90^{+30}_{-40}$ eV (Walton et al., 2013).

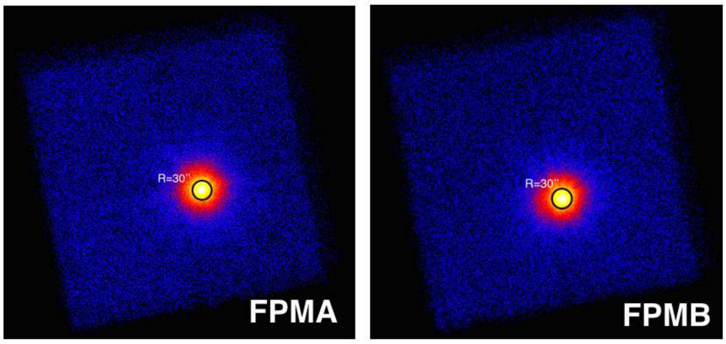

Figure 5.1: X-ray images from the *NuSTAR* FPMA (left panel) and FPMB (right panel) of MCG +8-11-11.

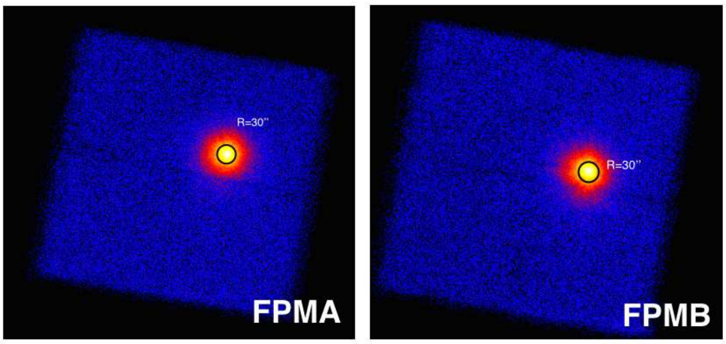

Figure 5.2: X-ray images from the *NuSTAR* FPMA (left panel) and FPMB (right panel) of NGC 6814.

5.2. OBSERVATIONS & DATA REDUCTION

5.2.1. NUSTAR

MCG +8-11-11 and NGC 6814 were observed by *NuSTAR* with its two coaligned X-ray telescopes (Focal Plane Modules A and B) respectively on 2016, August 19, and on 2016, July, 04. No other sources apart from the targets are apparent in the images.The *NuSTAR* data were reduced with the *NuSTAR* Data Analysis Software (NuSTARDAS) package (v. 1.6.0). Cleaned event files (level 2 data products) were produced and calibrated using standard filtering criteria with the NUPIPELINE task using the last calibration files available from the *NuSTAR* calibration database (CALDB 20170120). The extraction radii of the circular region were 0.5 arcmin for source and 1.5 arcmin for background spectra; there are no other bright X-ray sources within 1.5 arcmin from MGC 8-11-11 and NGC 6814 and no other sources were present in the background region (see Figures 5.1 and 5.2). Net exposure time, after this process, is 98 ks for MGC 8-11-11 and 148 ks for NGC 6814 for both FPMA and B. The spectra were binned in order to over-sample the instrumental resolution by at least a factor of 2.5 and to have a Signal-to-Noise Ratio (SNR) greater than 5 for both sources in each spectral channel.

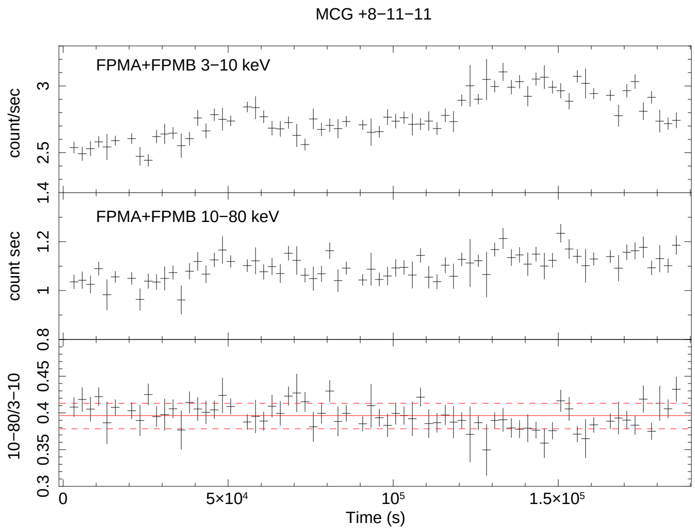

Figure 5.3: The *NuSTAR* FPMA+B light curves in the 3-10 keV (top panels), and in the 10-80 keV energy band (middle panels) are shown, for MCG +8-11-11. The ratio between 3-10 keV and 10-80 keV *NuSTAR* light curves is shown in the bottom panels for bottom sources; the red solid and dashed lines indicate the mean and standard deviation, respectively.

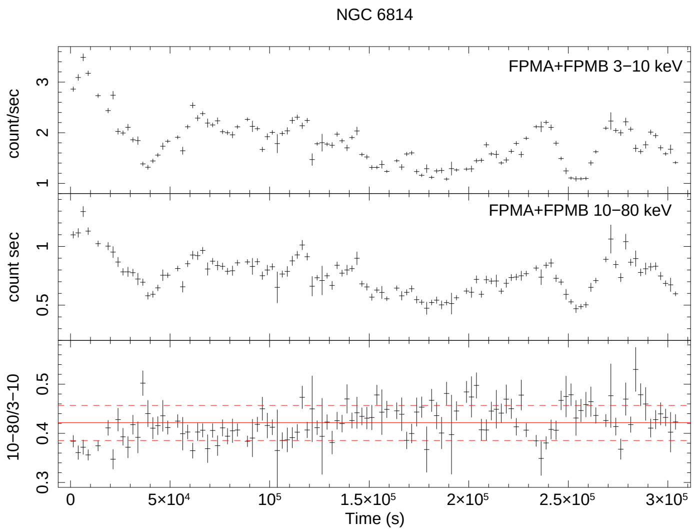

Figure 5.4: The *NuSTAR* FPMA+B light curves in the 3-10 keV (top panels), and in the 10-80 keV energy band (middle panels) are shown, for NGC 6814. The ratio between 3-10 keV and 10-80 keV *NuSTAR* light curves is shown in the bottom panels for bottom sources; the red solid and dashed lines indicate the mean and standard deviation, respectively.

5.2.2. SWIFT-XRT

MCG +8-11-11 and NGC 6814 were observed by *Swift* UVOT+XRT almost simultaneously with *NuSTAR* for a total exposure time of 20 ks each. *Swift* XRT spectra were extracted using the XSELECT (v2.4c) command line interface to the FTOOLS (Blackburn, 1995).

If there is pile-up the measured rate of the source is high (above about 0.6 counts s^{-1} in the Photon-Counting Mode). The easiest way to avoid problems related to pile-up is to extract spectra using an annular region, thus eliminating the counts in the bright core, where pile-up will occur (see Appendix B, Section B.2).

The *Swift* XRT spectra resulted to have an high pile-up degree. We tested different annular extraction regions for the source, gradually increasing the inner radius. Even with large inner extraction radii the pile-up was not removed and, moreover, the signal-to-noise ratio became very low. We therefore decided not to use the *Swift* XRT data for the spectroscopic analysis.

5.3. DATA ANALYSIS

The spectral analysis has been performed with the XSPEC 12.9.0 software package (Arnaud, 1996). Throughout the paper, errors correspond to 90% confidence level for one interesting parameter ($\Delta\chi^2 = 2.7$), if not stated otherwise. The cosmological parameters $H_0 = 70$ km s^{-1} Mpc^{-1}, $\Omega_\Lambda = 0.73$ and $\Omega_m = 0.27$, are adopted.

Both sources show variability in their light curves (especially NCG 6814, well known to be a variable source: Mukai et al. 2003, Walton et al. 2013). The variability of NGC 6814 was consistent with the softer-when-brighter behaviour and with the fact that its black hole mass is 1/10 times the black hole mass of MCG +8-11-11 but since no strong spectral variations were found in the ratio between the 10 − 80 and 3 − 10 keV count rates (see Figures 5.3 and 5.4) we decided to use time-averaged spectra for both sources.

We performed our data analysis by fitting the 3−80 keV *NuSTAR* spectra with different models, each of them including Galactic absorption with column densities $N_H = 1.84 \times 10^{21}$ cm^{-2} for MCG +8-11-11 and $N_H = 9.11 \times 10^{20}$ cm^{-2} for NGC 6814, as derived from HI maps (Kalberla et al., 2005). We tested the presence of additional intrinsic absorbers at the redshift of the sources, which in both cases resulted to be negligible in the *NuSTAR* band. The *NuSTAR* FPMA calibration constants are fixed to 1.0 while we left the *NuSTAR* FPMB cross-calibration constants free to vary. The values found for the constant for MGC +8-11-11 and NGC 6814 are respectively 1.034 ± 0.009 and 0.988 ± 0.008. These values are consistent with the expectation (Madsen et al., 2015).

5.3.1. X-RAY/OPTICAL RATIO

We used *Swift* data to compute the optical to X-ray spectral index (α_{ox}), defined as:

$$\alpha_{ox} = -\frac{\log\left[L_{2keV}/L_{2500Å}\right]}{2.607} \tag{5.1}$$

The α_{ox} index is the slope of a hypothetical power law between 2500Å and 2 keV rest-frame frequencies. The optical to X-ray ratio provides information about the balance between the accretion disc and the corona. The α_{ox} is found to be strongly anti-correlated with the ultraviolet luminosity density per unit frequency (see Lusso et al. 2010, Vagnetti et al. 2013 and references therein). The observed $\alpha_{ox} - L_{2500Å}$ correlation implies that AGN re-distribute their energy in the UV and X-ray bands depending on the overall luminosity; more optical luminous AGN emit less X-ray per unit UV luminosity than less luminous AGNs (Strateva et al., 2005).

The *Swift*/UVOT observations were analysed taking advantage of the on-line tool multi-mission archive at the Asi Science Data Center (ASDC) website[1]. Using this tool we performed an on-line interactive analysis for all the available observations for the sources MCG+8-11-11 and NGC 6814, 3 and 4 respectively. This on-line tool runs the standard UVOT pipeline and generates a sky map of the observation in the selected available filter. When the source is detected it is possible to select it and run the UVOT aperture photometry. Using this tool it is possible to compute the monochromatic flux in the selected filter. For all the observations we extract a circular region for the source with a radius of 5 arcsec and a properly selected annular region for the background. We obtain monochromatic and extinction-corrected fluxes for MCG+8-11-11 at 3465Å (U), 2246Å (UVM2), 1928Å (UVW2) and for NGC 6814 for the same filters and UVW1 (2600Å). Flux at 2500Å was then computed interpolating the monochromatic flux measures for both the sources. We obtained $F_{2500Å} = 3.98 \times 10^{-26}$ erg cm^{-2} s^{-1} Hz^{-1} and $F_{2500Å} = 4.36 \times 10^{-26}$ erg cm^{-2} s^{-1} Hz^{-1} respectively for MCG +8-11-11 and NGC 6814.

The 2 keV fluxes are extrapolated from the NuSTAR data. We found $F_{2keV} = 5.25 \pm 0.05 \times 10^{-28}$ erg cm^{-2} s^{-1} Hz^{-1} for MCG +8-11-11 and $F_{2keV} = 3.42 \pm 0.05 \times 10^{-29}$ erg cm^{-2} s^{-1} Hz^{-1} for NGC 6814.

With these values we computed the α_{ox} using the equation (5.1) obtaining 1.11 for MCG +8-11-11 and 1.36 for NGC 6814.

We use the values of $L_{2500Å}$, obtained from the previous values of the fluxes, to compute the X-ray/optical ratio with the relation found by Lusso et al. (2010):

$$\alpha_{ox}(L_{2500Å}) = (0.154 \pm 0.0010) \log L_{2500Å} - (3.176 \pm 0.233) \tag{5.2}$$

to check that the analysed sources follow the trend of the sources analysed by Lusso et al. (2010). We found $\alpha_{ox} = 1.23 \pm 0.32$ and $\alpha_{ox} = 1.51 \pm 0.25$ respectively for MCG +8-11-11 and NGC 6814. These values are consistent, with the values of α_{ox} we found before. Moreover the sources follow also the trend of the L_X−L_{UV} of Lusso & Risaliti (2017).

5.3.2. MCG +8-11-11

We started the spectral analysis by fitting the 3 − 80 keV *NuSTAR* spectrum with a phenomenological baseline model composed of a power law with an exponential cutoff for the primary continuum (CUTOFFPL), a Gaussian line to reproduce the narrow Fe Kα emission line at 6.4 keV, and a cold reflection component (PEXRAV. Magdziarz & Zdziarski 1995b). We fixed all element abundances to Solar values and the inclination angle to $\cos i = 0.86$, $i\,(\sim 30°)$. Since we know from the literature the presence of an emission line from H-like Fe Kα (Bianchi et al., 2010), we added another narrow Gaussian line, with the centroid energy fixed to 6.966 keV. We found a $\chi^2 = 467$ for 427 degrees of freedom (d.o.f.).The residuals around the narrow Fe Kα line suggest the presence of a broad line component. We therefore added a broad Gaussian line (hereafter model A1) to the previous model. The fit slightly improved, χ^2/d.o.f. = 446/424. We found a resolved Fe Kα

[1] http://www.asdc.asi.it

Table 5.1: Fit parameters for the emission features of MCG +8-11-11. Errors are at 90% confidence levels.

Parameter	Fe Kα NL	Fe Kα BL	Fe XXVI
E (keV)	$6.40^{+0.03}_{-0.06}$	$6.21^{+0.18}_{-0.28}$	$6.966^{\star}$
σ(keV)	$0.0^{\star}$	$0.31^{+0.15}_{-0.20}$	$0.0^{\star}$
EW (eV)	40 ± 15	90 ± 7	28^{+3}_{-7}
Flux (10^{-5} ph/cm^2/s)	$2.56^{+2.5}_{-3.7}$	5.78 ± 0.9	1.4 ± 0.3

$\star$ fixed parameter.

line with $\sigma = 0.31^{+0.15}_{-0.20}$ keV and the centroid energy at $6.21^{+0.18}_{-0.28}$keV. The fitting parameters for the three lines are shown in Table 5.1. We found a 3-80 keV flux of $1.45 \pm 0.03 \times 10^{-10}$ erg cm^{-2} s^{-1} Regarding the continuum, we found a power law index of 1.77 ± 0.02 and a cutoff energy of 260^{+190}_{-80} keV. The reflection fraction R was 0.15 ± 0.06 (Table 5.2, model A1).

The following step of the analysis was to replace the PEXRAV model plus the broad line with the RELXILL model (García et al., 2014), in order to test for the presence of a relativistic component (hereafter model B1). The inclination angle was fixed to a value of 30° and we fixed the ionization parameter to $\log\left(\frac{\xi_i}{\text{erg cm s}^{-1}}\right) = 0.0$ to test reflection from neutral material. Leaving the iron abundance free to vary we found a value of iron abundance of $A_{\rm Fe} = 3.1^{+1.7}_{-1.4}$, a reflection fraction R= $0.24^{+0.12}_{-0.07}$ and a lower limit on the spin of the central black hole of $a > 0.6$. The χ^2/d.o.f. for this fit was 452/425. Other fitting parameters are shown in Table 5.2.

Leaving the ionization parameter free to vary the fit did not improve, the χ^2/d.o.f. remained the same, and we found an upper limit value for the ionization parameter of $\log\left(\frac{\xi_i}{\text{erg cm s}^{-1}}\right) < 0.05$.

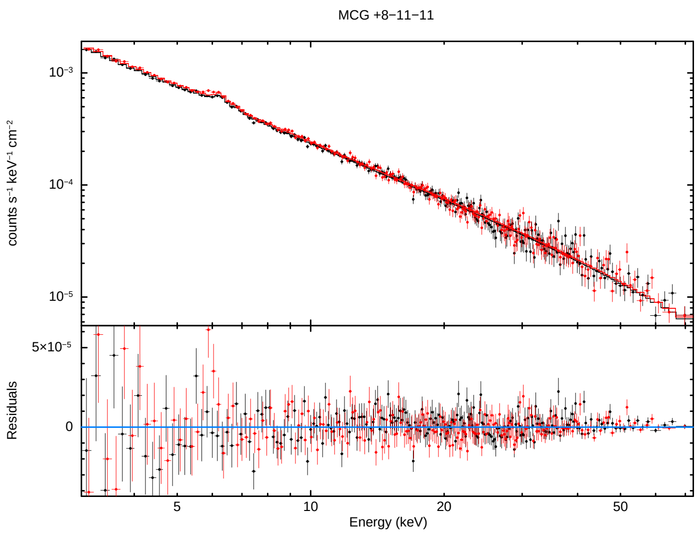

Figure 5.5: Data and best fit model of MCG +8-11-11 extrapolated from *NuSTAR* FPMA (black) and FPMB (red) spectra when model C1 (Figure 5.6) was used.

We then substituted the Gaussian narrow line in the B1 model with the XILLVER model

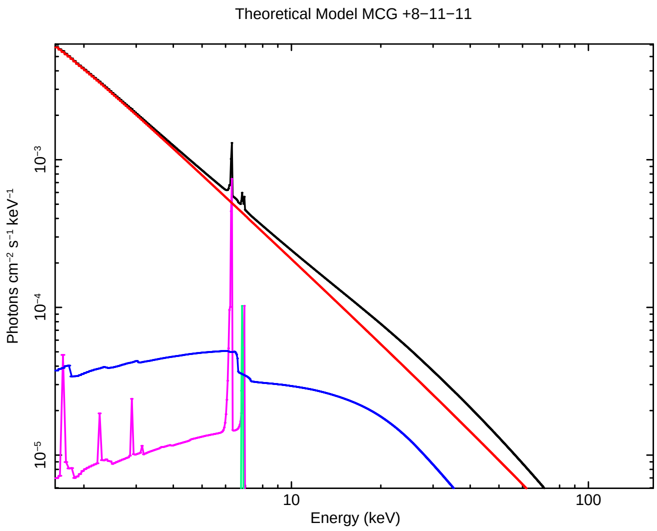

Figure 5.6: Best fitting model (black); the blue line is the RELXILL component, the red line represent the primary continuum, the green line represent the Fe XXVI emission line and the magenta line is the XILLVER component. See text for more details.

(García & Kallman 2010; García et al. 2013) (hereafter model C1, see right panel of Figure 5.5), to test if the reprocessed spectrum could originate in distant material, like a Compton-thick torus. The photon indices and the cutoff energy of the XILLVER and RELXILL models were tied together. The reflection fraction of XILLVER was free to vary. The fit gave a χ^2/d.o.f.= 457/425. We found a value for the high energy cutoff of 175^{+110}_{-50} keV (see Table 5.2). With this model the observed reflection component appeared to be mostly associated with the accretion disc and with the broad part of the Fe Kα. The narrow part of the Fe Kα line had an emission which was relatively strong compared to the Compton hump, and the reflection fraction of the XILLVER component was found to be quite low: $R^{xill} = 0.25 \pm 0.12$. This may be due to emission from a material with high iron abundance, and indeed we found an iron overabundance in the XILLVER model of $A_{Fe} > 8.5$. The other fit parameters are reported in Table 5.2. Contour plots are shown in Figure 5.9.

If we tried to keep tied the iron abundances between the XILLVER and the RELXILL model we found a value of 3.2 ± 0.7 but the fit worsened significantly with a resulting χ^2/d.o.f.= 514/425.

Finally, we tested if the large ratio between the line flux and the Compton hump may be due to reflection from a distant material with $N_H < 10^{24}$cm^{-2} using the MYTORUS model (Murphy & Yaqoob, 2009). This is a more physical model with respect to the phenomenological model C1, that we used to have a measure of the cutoff. We used the MYTORUS model to fit the cold reflection and the Fe Kα and Fe Kβ emission lines (and the associated Compton shoulders) adding the MYTORUS Compton-scattered continuum and fluorescent line tables to the RELXILL component (hereafter model D1). In the fit, we kept tied the photon indices of the MYTORUS table to the RELXILL one. The iron abundance for the RELXILL model was fixed to the values of the model C1, while for MY-

Table 5.2: Fitting parameters for MCG +8-11-11 for the models A1, B1, C1, D1. Errors are at 90% confidence levels. In the range of 3-0 keV we found a flux of $1.45 \pm 0.03 \times 10^{-10}$ erg cm^{-2} s^{-1} and an absorption corrected luminosity of $1.37 \pm 0.05 \times 10^{44}$ erg s^{-1}.

Model:	**A1**	**B1**	**C1**	**D1**
Γ	1.77 ± 0.02	1.77 ± 0.03	1.77 ± 0.04	1.83 ± 0.03
E_c (keV)	260^{+190}_{-80}	224^{+140}_{-70}	175^{+110}_{-50}	> 250
R^{PEXRAV}	0.15 ± 0.06	-	-	-
$R^{RELXILL}$	-	$0.24^{+0.12}_{-0.07}$	0.25 ± 0.12	0.23 ± 0.08
$R^{XILLVER}$	-	-	0.17 ± 0.04	-
a	-	> 0.6	> 0.5	< 0.72
$A_{Fe}^{RELXILL}$	-	$3.1^{+1.7}_{-1.4}$	< 2.5	$2.5^{\star}$
$A_{Fe}^{XILLVER}$	-	-	> 8.5	-
$N_H^{MYT}(10^{23}cm^{-2})$	-	-	-	5.0 ± 3.0
$\frac{\chi^2}{d.o.f}$	1.05	1.06	1.07	1.05

$\star$ fixed parameter.
Abundances are in Solar Units.

TORUS it is not a variable parameter being the Solar value. In the standard "coupled" configuration the inclination angle for the torus was fixed to $\theta = 30°$. We obtained a χ^2/d.o.f.= 445/435. The best-fit parameters are given in Table 5.2. We found a column density of $N_H = 5.0 \pm 3.0 \times 10^{23}$cm^{-2}, and only a lower limit to the cutoff energy of $E_c > 250$ keV. It must be remarked that the model is not fully self-consistent in this respect because in MYTORUS the illuminating continuum must be a straight power law, with a sharp terminal energy of ~ 500 keV. However, the lower limit of the cutoff energy is consistent with the values found with the previous models. Moreover, the reflection from distant, Compton thin material is in agreement with what we found in model C1, where the relativistic reflection dominates the spectral shape above 10 keV, with respect to the non-relativistic one.

Finally, we tried to see if the two components, modelled by XILLVER and RELXILL, are not two different physical components (one arising from the accretion disk and one from a distant material: a Compton-thin gas or a gas with a super-solar abundance of iron) but two different reflection components arising from different parts of the same region, in this case the accretion disk which is in different configuration. We modeled the spectrum with two relativistic components (two RELXILL models). Keeping all the parameters tied between the two model, except for the normalization, the resulting chi-square of the fit is χ^2/d.o.f.= 486/426 = 1.13 . We found a lower limit on the iron abundance of $A_{Fe} > 5.88$ and there are also clear residuals around 6.4 keV which indicate the presence of the narrow component of the Fe Kα line. Adding this component and allowing to vary the iron abundance parameter, the reflection fraction parameter, and the black hole spin parameter, we found a fit which is statistically equivalent to our best fit model, with a chi-square of χ^2/d.o.f.= 452/424 = 1.07. We found one RELXILL component with an upper limit on the iron abundance of $A_{Fe} < 1.48$ an upper limit on the spin parameter of $a < 0.48$ and a reflection fraction R= 0.16 ± 0.05. The second relxill component showed a lower limit on the iron abundance of $A_{Fe} > 6.35$, a spin value of $a = 0.07 \pm 0.01$ and a reflection fraction R< 0.07. This suggested us that the latter is not a relativistic component and it could not be produced by a Compton thick material since it had a very low associated reflection component and high iron abundance, similarly to the XILLVER component of our best fit (model C1). This scenario is consistent with what Bianchi et al. (2010) and Mantovani et al. (2016) found for this source.

Fluxes and centroid energies of the broad and narrow Fe Kα lines and of the Fe XXVI line resulted to be the same, within the errors, among the various models previously described.

CORONAL PARAMETERS

Assuming that the primary emission is due to Comptonization of thermal disc photons in a hot corona, we estimated the coronal parameters substituting the cut-off power law with a Comptonization model. We modelled the relativistic reflection and the non-relativistic reflection using respectively RELXILLCP and XILLVER-COMP models (García & Kallman 2010; García et al. 2014 and Dauser et al. 2014). These models use the NTHCOMP model (Zdziarski et al. 1996 and Życki et al. 1999) for the incident continuum. In RELXILLCP and XILLVER-COMP models, the maximum temperature of disc blackbody photons (which serve as seeds for Comptonization) is 0.1 keV, and it is not allowed to vary. The fit gave a χ^2/d.o.f.= 465/426 = 1.09. We found a photon index value of $1.84^{+0.03}_{-0.05}$; we found also a lower limit for the iron abundance of the non-relativistic reflection component: $A_{Fe} >$ 8.01 Solar Unit, and an upper limit for the iron abundance of the relativistic reflection component: $A_{Fe} <$ 0.5 Solar Unit, in agreement with the values reported in Table 5.2. We found a coronal temperature of 60^{+110}_{-30} keV, roughly in agreement with the expected relation$E_c = 2-3\times kT_e$ (Petrucci et al. 2000, 2001).

5.3.3. NGC 6814

The fitting procedure for NGC 6814 was very similar to that adopted for MCG +8-11-11. We started the analysis by fitting the 3 – 80 keV *NuSTAR* spectrum with the phenomenological baseline model, previously described in subsection 5.3.2 and composed by a cut-off power law, a PEXRAV plus a narrow Gaussian line around 6.4 keV. Also in this case we fixed all element abundances to Solar values and the inclination angle to $\cos i = 0.86$ ($i \sim 30°$). Since Walton et al. (2013) found the presence of an emission line from H-like Fe Kα with an EW of 90^{+30}_{-40} eV, we added also a narrow Gaussian line with the centroid energy fixed to 6.966 keV. However, only an upper limit to the EW of < 15 eV was found, which was more than four times lower than the value found by Walton et al. (2013). We found also an upper limit for the line flux of $< 2.1 \times 10^{-6}$ ph/cm^2. This was probably due to the fact that the line was diluted by a continuum which was about four times higher than that found by Walton et al. (2013) (see below). We therefore did not include this line in this and in the following fits. We found a χ^2/d.o.f.= 398/348. The residuals around the narrow Fe Kα line suggested the presence of a broad line. Adding a broad Gaussian line

Table 5.3: Fitting parameters for NGC 6814 using the models A2, B2, C2, D2, as described in the text. Errors are at 90% confidence levels. In the range of 3-0 keV we found a flux of $1.04 \pm 0.04 \times 10^{-10}$ erg cm^{-2} s^{-1} and an absorption corrected luminosity of $6.21 \pm 0.12 \times 10^{42}$ erg s^{-1}.

Model:	**A2**	**A2**	**C2**	**D2**
Γ	1.72 ± 0.02	1.74 ± 0.02	$1.71^{+0.04}_{-0.03}$	1.80 ± 0.02
E_c (keV)	260^{+220}_{-80}	210^{+80}_{-50}	155^{+70}_{-35}	> 260
R^{PEXRAV}	0.15 ± 0.07	-	-	-
R^{RELXILL}	-	0.26 ± 0.1	$0.27^{+0.10}_{-0.12}$	$0.26^{+0.18}_{-0.11}$
R^{XILLVER}	-	-	0.17 ± 0.03	-
a	-	> 0.2	> 0.03	> 0.4
$A_{\mathrm{Fe}}^{\mathrm{RELXILL}}$	-	< 1.4	$1.8^{+0.8}_{-1.3}$	$1.8^{\star}$
$A_{\mathrm{Fe}}^{\mathrm{XILLVER}}$	-	-	> 7.00	-
$N_{\mathrm{H}}^{\mathrm{MYT}}(10^{23}\mathrm{cm}^{-2})$	-	-	-	$3.5^{+3.0}_{-2.0}$
$\frac{\chi^2}{\mathrm{d.o.f}}$	1.08	1.06	1.08	1.06

$\star$ fixed parameter.
Abundances are in Solar Units.

at the PEXRAV plus the narrow Fe Kα line model (model A2) around 6.4 keV we found a resolved Fe Kα line with $\sigma = 0.59^{+0.37}_{-0.21}$ keV, EW of 102 ± 15 eV and flux of $4.2 \pm 1.4 \times 10^{-5}$ ph/cm^2/s. The centroid energy of the Fe Kα line was found to be at $6.43^{+0.03}_{-0.06}$ keV. The line had an EW of 70 ± 7 eV, consistent with what Walton et al. (2013) found. The flux of the line was $2.7 \pm 0.7 \times 10^{-5}$ ph/cm^2/s. The chi square for the fit with the model A2 was χ^2/d.o.f.= 373/345. The high energy cutoff was 260^{+220}_{-80}keV and the reflection fraction R= 0.15 ± 0.07. The $3-80$ keV flux was $1.04 \pm 0.04 \times 10^{-10}$ erg cm^{-2} s^{-1}. Other parameters are reported in Table 5.3.

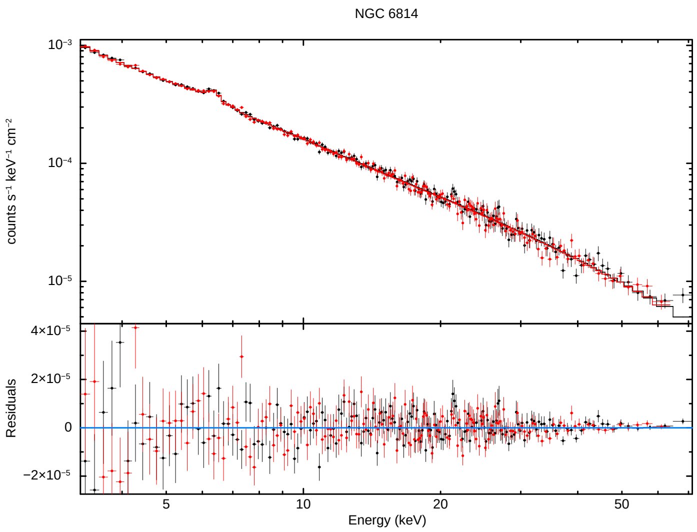

Figure 5.7: Data and best fit model of NGC 6814 extrapolated from *NuSTAR* FPMA (black) and FPMB (red) spectra when model C2 (see Figure 5.8) is used.

The following step in the analysis was to replace the PEXRAV model plus the broad line with the RELXILL model, as for the previous source but without the Fe XXVI line (hereafter model B2) in order to test for the presence of a relativistic component. The inclination

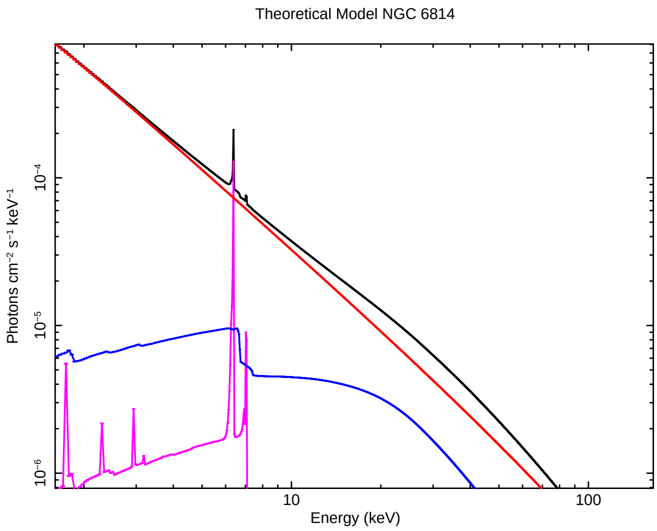

Figure 5.8: Best fitting model (black); the blue line is the RELXILL component, the red line represent the primary continuum and the magenta line is the XILLVER component. See text for more details.

angle was fixed to 30° and the ionization parameter was fixed to $\log\left(\frac{\xi_i}{\mathrm{erg\,cm\,s^{-1}}}\right) = 0.0$. Leaving the iron abundance free to vary we found a value of $A_{Fe} < 1.4$ in Solar Units, a reflection fraction R= 0.26 ± 0.1 and a lower limit on the spin of the central black hole of $a > 0.2$. The χ^2 values in this case was χ^2/d.o.f.= 366/343. Leaving the ionization parameter free to vary the fit did not improve, the χ^2 remained the same, and we found an upper limit value for the ionization parameter of $\log\left(\frac{\xi_i}{\mathrm{erg\,cm\,s^{-1}}}\right) < 0.34$. Other fitting parameters are shown in Table 5.3.

We then replaced the Gaussian narrow line in the model B2 with the XILLVER model (hereafter model C2; see Figure 5.8), to test if the reprocessed spectrum could originate in a distant material, as it was done for the other source in the previous section. The photon indices the cutoff energy of the XILLVER and RELXILL models are tied together. The reflection fraction of XILLVER was free to vary. The fit gave a χ^2/d.o.f.= 375/346. We found a value for the high energy cutoff of 155^{+70}_{-35} keV (see Table 5.3). The other fit parameters are reported in Table 5.3. Contour plots are shown in Figure 5.9. Also for NGC 6814, as for MCG +8-11-11, we found an iron overabundance in the XILLVER model, $A_{\rm Fe} > 7.0$ due to an emission of the narrow part of the Fe Kα line which was relatively strong compared to the Compton hump. If we tried to keep tied the iron abundances between the XILLVER and the RELXILL model we found a lower limit value of $\mathrm{A_{Fe}} > 4.$ and the fit worsened significantly with a resulting χ^2/d.o.f.= 379/347.

Similarly to the case of MCG +8-11-11, we tested the alternative model in which XILLVER was replaced by reflection from distant material with $\mathrm{N}_H < 10^{24}\mathrm{cm}^{-2}$ that could reproduce the narrow part of the fluorescence emission line from the iron K-shell with a small Compton hump. We used the MYTORUS model as described in subsection 5.3.2 (hereafter model D2). We obtained a χ^2/d.o.f.= 368/347. The best fit parameters are given in Table 5.3. We found a column density of $\mathrm{N_H} = 3.5^{+3.0}_{-2.0} \times 10^{23}\mathrm{cm}^{-2}$. Again, we found only a lower limit to the cutoff energy, $E_c > 260$ keV, which was consistent with the values found with the previous models.

Yamauchi et al. (1992) found an iron overabundance in the *Ginga* spectrum of the source. They justified the fact with the presence of a partially ionized state that may give an "apparent" overabundance because the partially ionized gas is transparent for the soft X-rays but absorbs X-rays above the Fe K-edge energy. In our fit, we considered neutral reflection material, so the super-solar value for the iron abundance could not be an effect of the ionization. Even in this case, we tested if the two reflection components could arise from two different parts of the accretion disk if it is in a different configuration. We modeled the spectrum with two RELXILL models. First, we kept all the parameters tied tighter between the two model, except for the normalization, the resulting chi-square of the fit is χ^2/d.o.f.= 409/347 = 1.17. We found a lower limit on the iron abundance of $A_{Fe} > 5.88$ and there are also clear residuals around 6.4 keV which indicate the presence of the narrow component of the Fe Kα line. Adding this component and allowing to vary the iron abundance parameter, the reflection fraction parameter, and the black hole spin parameter, we found a fit with a chi-square of χ^2/d.o.f.= 373/343 = 1.09. We found one RELXILL component with an upper limit on the iron abundance of $A_{Fe} < 2.09$ an upper limit on the spin parameter of $a < 0.48$and a reflection fraction R= 0.27 ± 0.12. The second relxill component showed a lower limit on the iron abundance of $A_{Fe} > 6.35$, an upper limit on the spin value $a < 0.15$ and a lower limit on the reflection fraction R< 0.12. Also NGC 6814 shows one of the RELXILL component which is not a relativistic component and it could not be produced by a Compton thick material since it had a very low associated reflection component and high iron abundance, similarly to the XILLVER component of our best fit (model C2).

Fluxes of the broad and narrow Fe Kα lines and of the Fe XXVI line were the same, within the errors, among the various models previously described.

CORONAL PARAMETERS

The final step was to use Comptonization models to estimate the coronal parameters as in section 5.3.2. We used RELXILLCP and XILLVER-COMP to model both the relativistic and non-relativistic reflection spectrum, see Section 5.3.2. The fit gave a χ^2/d.o.f.= 387/347 = 1.11. We found a photon index value of 1.79 ± 0.03 and a coronal temperature of 45^{+100}_{-17} keV, again in agreement with the $E_c = 2-3 \times kT_e$ relation (Petrucci et al. 2000, 2001). We found also a lower limit for the iron abundance of the non-relativistic reflection component: $A_{Fe} > 7.89$ Solar Unit, and an upper limit for the iron abundance of the relativistic reflection component: $A_{Fe} < 0.73$ Solar Unit, in agreement with the values reported in Table 5.3.

5.4. DISCUSSION AND CONCLUSIONS

We have presented the analysis of the *NuSTAR* observations of the Seyfert 1 galaxies NGC 6814 and MCG +8-11-11.

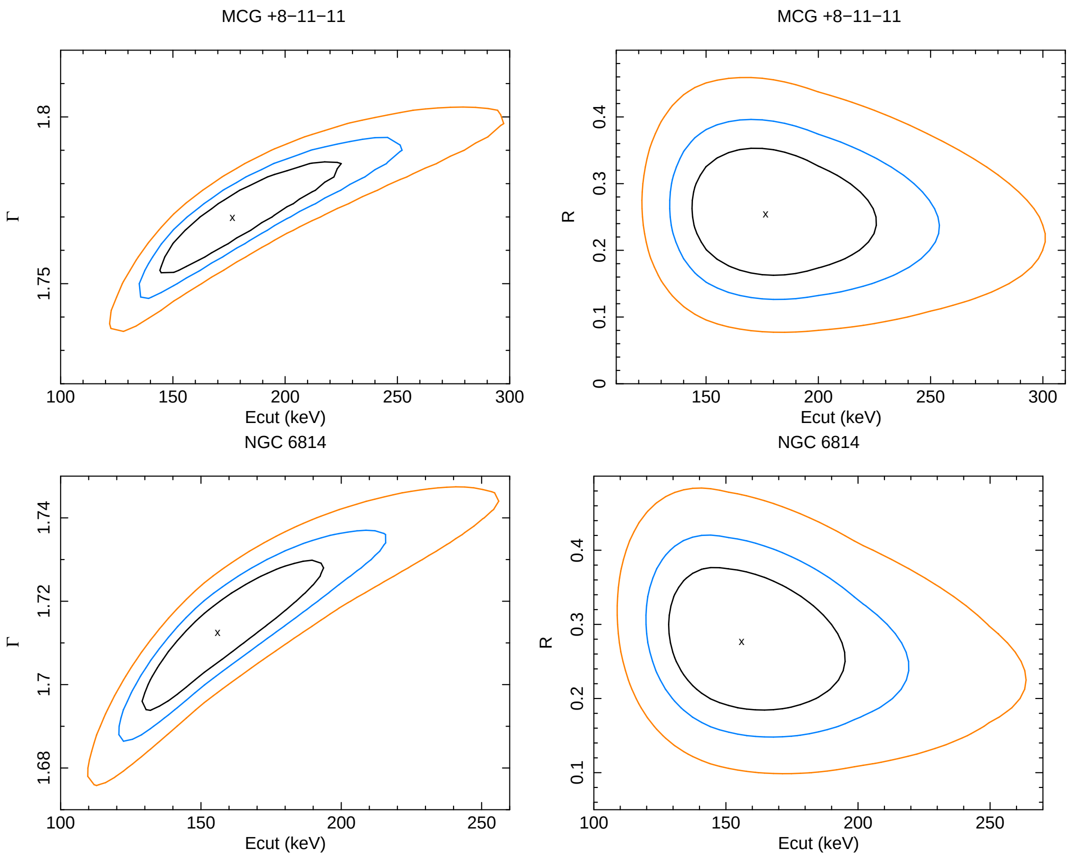

Figure 5.9: E_c-Γ contour plot (left panel) and E_c-R contour plot (right panel)for MCG +8-11-11 (top panel) and NGC 6814 (lower panel). The solid black, blue and orange curves refer to the 68, 90 and 99% confidence levels respectively. The X represents the best fit value of the parameters.

The $2-10$ keV absorption-corrected luminosities from the *NuSTAR* observations of the two sources are $L_{2-10} = 2.04 \times 10^{42}$ erg s^{-1} for NGC 6814 and $L_{2-10} = 5.13 \times 10^{43}$ erg s^{-1} for MCG +8-11-11. Using the 2−10 keV bolometric correction of Marconi et al. (2004), we estimated the bolometric luminosity to be $L_{bol} = 0.24 \times 10^{44}$erg s^{-1} (NGC 6814) and $L_{bol} = 14.2 \times 10^{44}$erg s^{-1}(MCG +8-11-11). From these bolometric luminosity, with the black hole masses of $\log \frac{M_{BH}}{M_\odot} = 7.19 \pm 0.02$ (Bian & Zhao, 2003b) (MCG +8-11-11) and $\log \frac{M_{BH}}{M_\odot} = 6.99^{+0.32}_{-0.25}$ (Pancoast et al., 2014, 2015) (NGC 6814), we estimated the Eddington ratio to be 2.46×10^{-3} for NGC 6814 and 7.54×10^{-1} for MGC +8-11-11.

Thanks to the *NuSTAR* sensitivity at high energies, it was possible to measure the

Table 5.4: Coronal parameters for MCG +8-11-11 and NGC 6814 when the self-consistent model XILLVER-COMP + RELXILLCP is used to fit the data. The optical depths are extrapolated from Beloborodov (1999). Errors are at 90% confidence levels.

Parameter	**MCG +8-11-11**	**NGC 6814**
kT_e (keV)	60^{+110}_{-30}	45^{+100}_{-17}
τ	1.8 ± 0.2	2.5 ± 0.2
Γ	$1.84^{+0.03}_{-0.05}$	1.79 ± 0.03
$A_{Fe}^{RELXILL}$(Solar Units)	< 0.5	< 0.73
$A_{Fe}^{XILLVER}$(Solar Units)	> 8.01	> 7.89
$\frac{\chi^2}{d.o.f}$	1.09	1.11

high energy cutoff value for both sources; we found 175^{+110}_{-50} keV and 155^{+70}_{-35} respectively for MCG +8-11-11 and NGC 6814. We found also a disk reflection component and we constrained the reflection fraction finding 0.25 ± 12 for MCG +8-11-11 and of $0.27^{+0.10}_{-0.12}$ for NGC 6814.

Both sources showed a slightly broadened relativistic Fe Kα line plus a narrow component. The reflection component was modest, and mostly associated with the broad line component. The low reflection fraction found in MCG +8-11-11 was consistent with the value found by Mantovani et al. (2016). Past observations of NGC 6814 did not show broad line (Bentz et al. 2009, Malizia et al. 2014, Ricci et al. 2014) . The Compton hump associated with the narrow line was very small, similarly to what found in another Seyfert galaxy, NGC 7213 (**?**).

We found in our analysis a slightly broadened relativistic Fe Kα line plus a narrow component. The former is modelled by the relativistic model RELXILL while the latter by the non-relativistic model XILLVER. The iron abundance measured with the RELXILL model is considerably lower with respect to the super-Solar abundance measured with the XILLVER model. Since there was no Compton reflection hump associated with the narrow component of the iron Kα line, it could not be produced by a Compton-thick material, like the accretion disc or the Compton-thick torus, thus almost all the reflection should be associated with the accretion disk.
The interaction of X-rays with a material with super-Solar abundance of iron, gives rise to a reflection component with small Compton hump associated with the narrow iron Kα emission line. This is because the iron atoms interact with the X-rays, causing photoelectric absorption and the spectrum shows an iron Kα line with a drop at ~ 7 keV, due to the photoelectric absorption edge. The depth of the edge increases with the iron abundance and saturates around $A_{Fe} \sim 10$ (Matt et al., 1997). The curvature of the continuum above ~ 10 becomes weaker, resulting in a very small Compton reflection.
A reflection component with small Compton hump associated with the narrow iron Kα emission line could be produced also by the interaction of X-rays with a Compton thin material. To confirm this scenario we fitted the cold reflection component with the MYTORUS model and we found a values of $N_H < 10^{24}$cm^{-2}. This could implies that there would be no evidence of the classical Compton-thick torus in these sources, as already suggested by Bianchi et al. (2010) for MCG +8-11-11.

Ultimately we tested also if the two different reflection components should be part of the emission by the same material, such as an accretion disk which is in different configuration. But this attempt has further strengthened the scenario described above.

Regarding the relativistic component, for both sources we derived only lower or upper limits to the spin of the black hole of the two sources, depending on the adopted model. The relativistic line was fairly broad, so there are degeneracies in the parameters of the models which prevent us from determining a good measurement of the spin. We conclude that this parameter is basically unconstrained, not surprisingly given the relative weakness of the relativistic reflection.

We estimated the coronal parameters by fitting the *NuSTAR* data with a model which takes into account both the relativistic and non-relativistic reflection when illuminated by a thermally Comptonized continuum. We found a coronal temperature of 60^{+110}_{-30} keV for MCG +8-11-11 and 45^{+100}_{-17} keV for NGC 6814. It is interesting to note that the coronal temperature of the two sources are very similar despite an order of magnitude difference in mass and Eddington ratio.

We estimated the optical depth using the relation from Beloborodov (1999):

$$\Gamma \approx \frac{9}{4} y^{-2/9} \tag{5.3}$$

where Γ is the photon index of the spectrum between 2 and 10 keV. The dependence from the optical depth is in the relativistic y-parameter:

$$y = 4\left(\Theta_e + 4\Theta_e^2\right)\tau(\tau+1) \tag{5.4}$$

where Θ_e is the electron temperature normalized to the electron rest energy:

$$\Theta_e = \frac{kT_e}{m_e c^2} \tag{5.5}$$

We found $\tau = 1.79 \pm 0.2$ for MCG +8-11-11 and $\tau = 2.5 \pm 0.2$ for NGC 6814.

We used the values of the coronal temperature reported in Table 5.4 to put MCG +8-11-11 and NGC 6814 in the compactness-temperature (Θ_e - ℓ) diagram (Fabian et al. 2015, and references therein). Here Θ_e is the electron temperature normalized to the electron rest energy, defined above in equation 6.5, and ℓ is the dimensionless compactness parameter (Fabian et al., 2015):

$$\ell = \frac{L}{\mathrm{R}} \frac{\sigma_T}{m_e c^3} \tag{5.6}$$

where L is the luminosity and R is the radius of the corona (assumed spherical). To compute the compactness parameter, following Fabian et al. (2015) we adopted the luminosity of the power-law component extrapolated to the 0.1 – 200 keV band; since no measurement exists for the corona radius, we assume a value of 10 gravitational radii R_g. For MCG +8-11-11 we found $\ell = 27 \pm 12(\mathrm{R}_{10})^{-1}$ and $\Theta_e = 0.11^{+0.15}_{-0.10}$; for NGC 6814 $\ell = 14.5 \pm 4.5(\mathrm{R}_{10})^{-1}$ and $\Theta_e = 0.08^{+0.1}_{-0.05}$. Here R_{10} is the ratio between the corona radius and $10\mathrm{R}_g$.

With these values of Θ_e and ℓ both sources are positioned under the Svensson pair runaway line for a spherical geometry (Svensson, 1984), above the $e^- - e^-$coupling line, like most of the sources among those analysed by Fabian et al. (2017). The pair runaway line in the Θ_e - ℓ diagram is a curve which determine a forbidden region in which the pair production exceeds the annihilation. The detailed shape of this line depends on the source of soft photons and on the radiation mechanism. Above the $e^- - e^-$coupling line the $e^- - e^-$ coupling time scale is longer than the Compton cooling time scale. The location of these sources within the Θ_e - ℓ plane fits well in the scenario in which the AGN spectral shape is controlled by pair production and annihilation.

6

A *NuSTAR* census of coronal parameters in Seyfert galaxies

"To raise new questions, new possibilities, to regard old problems from a new angle, requires creative imagination and marks real advance in science."

Albert Einstein

In this chapter we present and discuss the results on the hot corona parameters of Active Galactic Nuclei that have been recently measured with *NuSTAR*. The literature values of a sample of nineteen bright Seyfert galaxies are analysed.
The aim of this work is to look for correlations between spectral and coronal parameters, such as the photon index and the cutoff energy, with other physical parameters, e.g. the black hole mass or the Eddington ratio.
We analysed the literature coronal parameters of nineteen unobscured nearby bright Seyfert galaxies that are present in the *Swift-BAT* 70 months catalogue and that have been observed simultaneously by *NuSTAR* and others X-rays observatories such as *Swift*, *Suzaku* or *XMM-Newton*.
We found an anti-correlation with a significance level > 98% between the coronal optical depth and the coronal temperature of our sample. Moreover, our analysis excludes the existence of any further correlation between the other spectral and physical parameters.

6.1. Sample selection and Goals

We have seen in previous chapters (Chapter 1 and 2) that the primary X-ray emission is characterized by a power-law spectral shape extending to energies determined by the electrons temperature. The power-law often shows a cutoff at high energies. Both the energy of the cutoff and the photon index are related to the temperature and the optical depth of the corona. Comptonization models imply that the cutoff energies are 2-3 times the temperature of the corona (Petrucci et al. 2000, 2001).. To investigate the shape of the spectrum is important to take into account the reprocessed emission of circumnuclear environment in this energy range, such as reflection from accretion disc and distant material. Typical X-ray features of the cold circumnuclear material include intense iron K alpha line at 6.4 keV and the associated Compton reflection peaking at 30 keV.

Before the coming of *NuSTAR*, several cutoff energies have been measured in nearby Seyfert galaxies by X-ray satellites like *Beppo-SAX* (Perola et al., 2002) and *INTEGRAL* (Malizia et al., 2014). The measurements ranged between 50 to 300 keV but the lack of focusing instruments at high energies resulted in large uncertainties and degeneracies between cutoff and other physical observables (in particular the slope of the primary power-law and the amount of the radiation Compton scattered by circumnuclear material, see Figure 6.1).

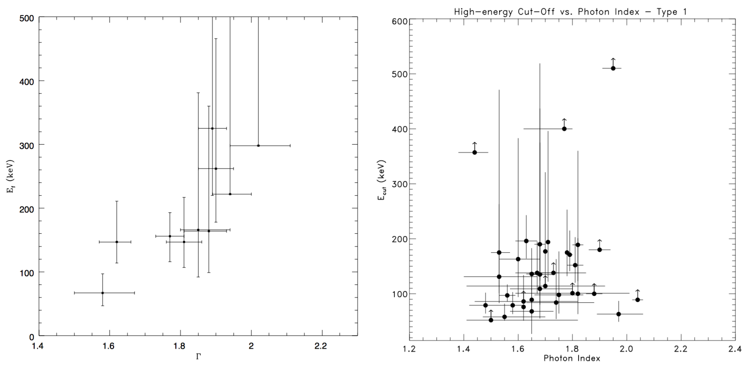

Figure 6.1: The plot of the cutoff energy vs the photon index from *Beppo-SAX* observations (left panel, Perola et al. (2002)) and from *INTEGRAL* observations (right panel, Malizia et al. (2014)). Both sample appears to confirm the existence of correlation with the cutoff energy increasing with Γ.

Unlike the previous hard X-ray observatories, which are background dominated for almost all AGN, *NuSTAR* (Harrison et al., 2010) is the first focusing hard X-ray telescope on orbit, 100 times more sensitive in the 10-79 keV band compared to previous observatories working in the same energy band. The focusing capability implies a very low background, and the observation of bright AGN, are source-dominated. *NuSTAR* data can therefore provide strong and robust constraints on the high energy cutoff, allowing to study ANG at high energies with high precision and with unprecedented accuracy. Thanks to *NuSTAR* observations in collaborations with other X-ray satellites such as *XMM-Newton* and *Swift*, in the last few years several cutoff energies have been measured with very high precision.

We build a small catalogue to look for correlations between coronal temperature and other physical parameters, choosing the unobscured ($N_H < 5 \times 10^{22}\mathrm{cm}^{-2}$) nearby, most bright, non-jetted (following the distinction made by Padovani et al. 2017), Seyfert galaxies that are present in the *Swift-BAT* 70 months catalogue and that have been observed simultaneously by *NuSTAR*

First we took data from the literature; the next step of the analysis, (which is not reported in this thesis) will be to built a model based on Monte Carlo simulations and to analyse all the sources with this model.

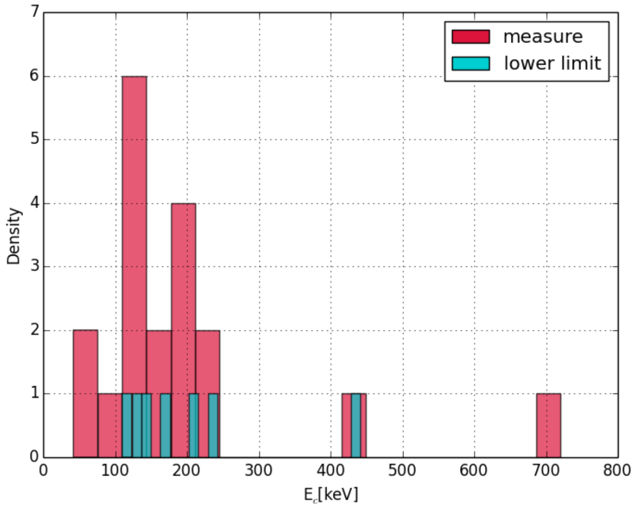

Figure 6.2: The histogram of the distribution of the high-energy cutoff of the sample when both measures (red) and lower limits (blue) are considered.

6.1.1. THE SAMPLE

The primary X-ray emission is characterized by a power-law spectral shape extending to energies determined by the electron temperature. The power-law often shows a cutoff at high energies. Both the energy of the cutoff and the photon index are related to the temperature and the optical depth of the corona. Comptonization models imply that the cutoff energies are 2-3 times the temperature of the corona ((Petrucci et al., 2000, 2001)). To investigate the shape of the spectrum it is important to take into account the reprocessed emission of the circumnuclear environment in this energy range, such as reflection from accretion disc and distant material. Typical X-ray features of the cold circumnuclear material include intense iron K alpha line at 6.4 keV and the associated Compton reflection peaking at 30 keV.

Unlike the previous hard X-ray observatories, which are background dominated for almost all AGN, *NuSTAR* is the first focusing hard X-ray telescope on orbit, 100 times more sensitive in the 10-79 keV band compared to previous observatories working in the same energy band. The focusing capability implies a very low background, and the observation of bright AGN, are source-dominated. *NuSTAR* data can, therefore, provide strong and robust constraints on the high-energy cutoff, allowing to study AGN at high energies with high precision and with unprecedented accuracy. Thanks to *NuSTAR* observations in collaborations with other X-ray satellites such as *XMM-Newton* and *Swift*, in the last few years several cutoff energies have been measured with very high precision.

We built the catalogue by choosing the unobscured ($N_H \le 6\times10^{22}\mathrm{cm}^{-2}$) nearby brightest Seyfert galaxies that are present in the *Swift-BAT* 70 months catalogue and that have been observed simultenously by *NuSTAR* and other X-rays observatories, such as *Swift*, *Suzaku* or *XMM-Newton*. We selected only unobscured, or moderately obscured AGN to have a clear view of the primary emission component. Other objects for which the cut-off energy had been left fixed in the spectral analysis are not included (1H0707-495 for instance), since they need a more intensive study on this issue.The list and the characteristics of all the sources can be found in Table 6.1.

The final sample comprises nineteen objects, twelve of which having a precise measurement of the cutoff energy and seven having only a lower limit. The distribution of high-energy cutoff measurements from the sample is shown in Figure 6.2. Some sources show clear evidence of both cold and relativistic reflection and others in which only distant neutral reflection contributes to the Compton hump at high energies.

6.1.2. LIST OF THE SOURCES

- **NGC 5506** is a bright, nearby($z = 0.006181$) Compton-thin (Wang et al., 1999), narrow-line Seyfert 1 galaxy (Nagar et al., 2002). Its spectrum is well described by a power-law with $\Gamma = 1.9 \pm .03$ with an high energy exponential cutoff at 720^{+130}_{-190} keV (Matt et al., 2015). NGC 5506 has a galactic absorption with a column density of 3.8×10^{20} cm^{-2} (Kalberla et al., 2005). The observed 2-10 keV flux corrected for absorption is 6.2×10^{-11} erg cm^{-2}s^{-1} corresponding to a luminosity of 5.26×10^{42} erg s^{-1} (Matt et al., 2015).

- **MCG -05-23-16** is a nearby ($z = 0.0085$, 36Mpc)Seyfert 1.9 galaxy (Veron et al. 1980; Wegner et al. 2003). This source has a complex structure of the fluorescent line emission, including both broad and narrow components produced by the disc and the torus reflection, respectively (Baloković et al., 2015). It has an absorption with column density of 2.5×10^{22}cm^{-2}. The photon index of the primary power-law results to be 2.00 ± 0.01. It shows also an high energy cutoff at 116^{+6}_{-5}keV (Baloković et al., 2015)

- **SWIFT J2127.4+5654** ($z = 0.0144$) is a narrow-line Seyfert 1. It was observed by *NuSTAR* and *XMM-Newton* in an observational campaign performed in November 2012. This source is affected only by the the Galactic column density absorption (7.65×10^{21} cm^{-2}, Kalberla et al. 2005). The primary emission of this source has a power-law spectral shape with a photon index of 2.08 ± 0.01 and a cutoff energy $E_c = 108^{+11}_{-10}$ (Marinucci et al., 2014a).

- **IC4329A** is a nearby bright Seyfert galaxy ($z = 0.0161$ Willmer et al. 1991; Galactic $N_H = 4.61 \times 10^{20}$ cm^{-2}, Kalberla et al. 2005). It has been observed by *NuSTAR* quasi-continuously from 2012 August 12-16. The photon index of the primary power-law of IC4329A is 1.73 ± 0.01. The spectrum shows a cutoff at 184 ± 14 keV (Brenneman et al., 2014).

- **3C 390.3** ($z = 0.056$) is a radio-loud Seyfert 1 galaxy with a weak reflection and a flat photon index. The timing properties of 3C390.3 do not differ from those of radio-quiet Seyferts (Gliozzi et al., 2009) and that there is no noticeable contribution from the jet to the X-ray emission (Sambruna et al., 2009). It has a Galactic column density of $4 \times 10^{20}\mathrm{cm}^{-2}$ (Kalberla et al., 2005), a photon index of the primary power-law of 1.70 ± 0.01 and a cutoff at energy of 116^{+24}_{-8} keV (Lohfink et al., 2015).

- **3C 382** ($z = 0.057870$) is a broad-line radio galaxy but its X-ray continuum is dominated by the Comptonizing corona similarly to radio-quiet Seyfert galaxies (Ballantyne et al., 2014). It has a Galactic absorption with a column density of $N_H = 6.98 \times 10^{20}\mathrm{cm}^{-2}$ (Kalberla et al., 2005) and a weak, highly ionized warm absorber with $N_H \approx 1.4 \times 10^{21}\mathrm{cm}^{-2}$ and $\log\xi = .5$, it has also a $\Gamma = 1.68^{+0.03}_{-0.02}$ and a high energy cutoff at 214^{+147}_{-63} keV (Ballantyne et al., 2014).

- **GRS 1734-292** ($z = 0.0214$, corresponding to a distance of 87 Mpc) is a Seyfert Galaxy originally discovered by the ART-P telescope aboard the *GRANAT* satellite (Pavlinsky et al., 1992). It has a total hydrogen column density in excess of 10^{22} cm^{-2}. The 2-10 keV flux for this source is $F_{2-10} = 5.12^{+0.15}_{-0.08} \times 10^{-11}$ erg cm^{-2} s^{-1}. GRS 1734-292 has the spectral slope of the primary power-law typical of a Seyfert galaxy in the *NuSTAR* observation ($\Gamma \sim$1.65), with one of the lowest high energy cutoff (53^{+11}_{-8} keV) measured so far by *NuSTAR* (Tortosa et al., 2017).

- **NGC 6814** ($z = 0.0052$, Molina et al. 2009) is a Seyfert 1 Galaxy known to show X-ray variability by at least a factor of 10 over time scales of years (Mukai et al., 2003). The $2-10$ keV absorption-corrected luminosities from the *NuSTAR* observation is $\mathrm{L}_{2-10} = 2.04 \times 10^{42}$ erg s^{-1}. It has a primary power-law with a photon index of $1.71^{+0.04}_{-0.03}$ and an exponential cutoff at 135^{+70}_{-35} keV (Tortosa et al., 2018).

- **MCG 8-11-11** ($z = 0.0204$) is a very X-ray bright AGN. The $2-10$ keV absorption-corrected luminosities from the *NuSTAR* observation is $\mathrm{L}_{2-10} = 5.13 \times 10^{43}$ erg s^{-1}. It has a primary power-law with a photon index of 1.77 ± 0.04 and an exponential cutoff at 175^{+110}_{-50} keV (Tortosa et al., 2018).

- **Ark 564** ($z = 0.02468$) is a narrow line Seyfert 1 galaxy. It has a steep X-ray spectrum, strong soft excess, and rapid variability. It is also extremely bright in the soft X-ray band ($F_{0.3-10keV} = 1.4 \times 10^{-10}$ erg $\mathrm{cm}^{-2}\mathrm{s}^{-1}$ (Kara et al., 2017). Ark 564 has a photon index of 2.27 ± 0.08 and a very low cutoff energy value: $E_c = 42 \pm 3$ (Kara et al., 2017).

- **PG 1247+267** is one of the most luminous known quasars at $z \sim 2$ and is a strongly super-Eddington accreting supermassive black hole (SMBH) candidate. It was observed by *NuSTAR* in December 2014 for a total of 94 ks. From this observation it results that Pg 1247+267 has a primary power-law with a cutoff energy at 89^{+134}_{-34} keV and photon index of $2.35^{+0.09}_{-0.08}$ (Lanzuisi et al., 2016).

- **Ark 120** ($z = 0.033$) is a 'bare' Seyfert 1 galaxy, a system in which ionized, displaying neither intrinsic reddening in its IR continuum nor evidence for absorption in UV and X-rays absorption is absent (Matt et al. 2014, Porquet et al. 2017). The spectrum of the source has a measure of the high energy cutoff value of 183^{+83}_{-43} keV Porquet et al. (2017). The photon index of the primary power-law is 1.87 ± 0.02 (Porquet et al., 2017).

- **NGC 7213** ($z = 0.005839$) is a low-luminosity active galactic nucleus that hosts a supermassive black hole of $\sim 10^8$ solar masses. It has also been classified as a low-ionization nuclear emission region galaxy (LINER) because of the low excitation observed in the narrow-line spectrum (Filippenko & Halpern, 1984). The photon index of the primary power-law of the spectrum of NGC 7213 is 1.84 ± 0.03. The sources does not have a cutoff measurements but shows only a lower limits on the cutoff energy of $E_c > 140$keV (Ursini et al., 2015).

- **MCG 6-30-15** ($z = 0.008$), is a Seyfert 1 galaxy with an extreme X-rays variability and a very broad Fe kα line emission, with an iron abundance significantly higher than solar (Fabian et al., 2002). Its primary power-law show a photon index of 2.06 ± 0.01 and a lower limit on the high enery cutoff which results to be > 110 keV (Marinucci et al., 2014b).

- **NGC 2110** ($z = 0.008$) is a bright Seyfert 2 galaxy. it shows a prominent Fe kα line with a variable intrinsic emission and shows a cutoff energy $E_c > 210$ keV, with no detectable contribution from Compton reflection (Marinucci et al., 2015). The source has several layers of absorbing material with column densities in the range $2 - 6 \times 10^{22}$cm^{-2} (Rivers et al., 2014).

- **Mrk 335** ($z = 0.0257$) is a arrow-line Seyfert 1 galaxy that show narrower broad emission-line components than typical Type 1 AGN (Grier et al., 2012). It has been observed by *NuSTAR* in June and July 2013. The Galactic absorption for this source is of 3.56×10^2 cm^{-2} (Kalberla et al., 2005). Its primary power-law spectrum shows a photon index of $2.14^{+0.02}_{-0.04}$ and a cutoff energy $E_c > 174$ (Parker et al., 2014).

- **Fairall 9** ($z = 0.047016$) is a Seyfert 1 galaxy. It has been observed by *NuSTAR* in May, 2014 and does not show any significant absorption other than Galactic (Lohfink et al., 2016). The photon index of its primary power-law is $1.96^{+0.01}_{-0.02}$, which shows a cutoff $E_c > 242$ (Lohfink et al., 2016).

- **Mrk 766** ($z = 0.012929$) is a narrow line Seyfert 1 galaxy which shows spectral variability in the X-rays (Risaliti et al., 2011). Its X-ray spectrum is well fitted by a power-law with photon index $2.22^{+0.02}_{-0.03}$ and an exponential cutoff with a lower limit of > 441keV (Buisson et al., 2017).

- **PG 1211+143** (z = 0.080900) is a bright radio-quiet quasar which belongs to the class of Narrow Line Seyfert 1 galaxies and presents an archetypical case for the ultra-fast outflows. The amount of Galactic neutral absorption along the line of sight is 2.7×10^{20} cm^{-2} (Kalberla et al., 2005). The photon index of the primary power-law of the spectrum of this source is 2.51 ± 0.2 with a lower limit on the exponential cutoff of > 124 keV (Zoghbi et al., 2015).

6.1.3. BLACK HOLE MASS MEASUREMENTS

Some of the selected sources had more than one literature value for the mass of the central black hole. One of the most reliable and direct way to measure the mass of a super massive black hole residing in the nucleus of an active galaxy is reverberation mapping (RM, Blandford & McKee 1982; Peterson 1993). We decided to use the RM mass values, for the sources that have one (IC4329A, 3C390.3, Ark 564, Ark 120, Mrk 335, Fairall 9, Mrk 766, PG 1211+143 Peterson et al. 2004; NGC 6814 Pancoast et al. 2014, 2015). For the sources without a RM measurement we used mass values coming from virial mass method, such as single-epoch method (SE). This method starts from the relation between the size and the luminosity of the broad line region (R-L relation), to derive the brad line region size through a single measure of the optical continuum luminosity and, combining this information with the width of a broad line,it is possible to build a relation for the black hole mass estimate (Vestergaard, 2002; Vestergaard & Peterson, 2006). One of the most used R-L relations based on Hβ RM measurements is (Bentz et al., 2009):

$$\log \frac{R}{lightdays} = -2.13 + 0.519 \log \frac{\lambda L_{\lambda}(5100\text{Å})}{\text{ergs}^{-1}} \tag{6.1}$$

In the case of NGC 5506 the central stellar velocity dispersion ($\approx$ 180km s^{-1}) (Oliva et al. 1999, Papadakis 2004) and the width of the [OIII] line (Boroson, 2003) give a black hole mass $\sim 10^8 M_{\odot}$, and we decided to use this value.

We assumed a 20% uncertainty for black hole mass estimates not inferred from reverberation.

6.2. THE FITTING PROCESS

The aim of this work is, as said before, to look for the correlation between the spectral parameters, such as the cutoff value and physical parameters.

The goodness of the correlation is given by the Spearman's rank correlation coefficient or Spearman's ρ.The Spearman correlation coefficient is defined as the Pearson correlation coefficient between the ranked variables. The sign of the Spearman correlation indicates the direction of the association between X (the independent variable) and Y (the dependent variable). A Spearman correlation of zero indicates that there is no tendency for Y to either increase or decrease when X increases. When X and Y are perfectly monotonically related, the Spearman correlation coefficient becomes 1.0 (or -1.0

Table 6.1: Spectral parameters, masses, luminosity and accretion rates of the sources of the selected sample. Accretion rates are computed using the L_x in the 2-10 keV energy band using the bolometric correction of Marconi et al. (2004). Luminosity is in unit of 10^{44} erg s^{-1}. Flux is in unit of 10^{-11} erg cm^{-2}s^{-1}. The bottom part of the table is for objects with lower values of the high energy cutoff.

Source	Ref.	Γ	E_c	$\log(M_{bh}/M_\odot)$	Ref.	L_{bol}/L_{Edd}	$L_{2-10keV}$	$F_{2-10keV}$	kT_e	τ	geom.	model
			[keV]				erg s^{-1}	erg cm^{-2}s^{-1}	[keV]			
NGC 5506	1	1.91 ± 0.03	720^{+130}_{-190}	8.0 ± 0.2	(A)	0.006	0.053	6.2	440^{+230}_{-250}	$0.02^{+0.2}_{-0.01}$	slab	COMPTT
									440^{+230}_{-250}	$0.09^{+0.2}_{-0.01}$	sphere	COMPTT
MCG -05-23-16	2	1.85 ± 0.01	170 ± 5	7.7 ± 0.2	(B)	0.058	0.18	10.4	30 ± 2	1.2 ± 0.1	slab	COMPTT
									25 ± 2	3.5 ± 0.02	sphere	COMPTT
SWIFT J2127.4	3-4	2.08 ± 0.01	180^{+75}_{-40}	7.2 ± 0.2	(J)	0.136	0.14	2.9	70^{+40}_{-30}	$0.5^{+0.3}_{-0.2}$	slab	COMPTT
									50^{+30}_{-25}	$1.4^{+1.0}_{-0.7}$	sphere	COMPTT
IC4329A	5-6	1.73 ± 0.01	185 ± 15	8.08 ± 0.3	(N)	0.125	0.56	12.0	37 ± 7	1.3 ± 0.1	slab	COMPTT
									33 ± 6	3.4 ± 0.5	sphere	COMPTT
3C390.3	7	1.70 ± 0.01	120 ± 20	8.4 ± 0.4	(H)	0.241	1.81	4.03	40 ± 20	$3.3^{+1.3}_{-2.8}$	sphere	COMPTT
3C382	8	1.68 ± 0.03	215^{+150}_{-60}	9.2 ± 0.5	(D)	0.072	2.34	2.9	330 ± 30	0.2 ± 0.02	slab	COMPTT
GRS 1734-292	9	1.65 ± 0.05	53 ± 10	8.5 ± 0.1	(L)	0.036	0.056	2.9	12 ± 1	2.9 ± 0.2	slab	COMPTT
									$12^{+1.7}_{-1.2}$	6.3 ± 0.3	sphere	COMPTT
NGC 6814	10	1.71 ± 0.04	135^{+70}_{-35}	7.0 ± 0.1	(C)	0.003	0.021	0.2	45^{+100}_{-20}	$2.5^{\dagger} \pm 0.5$	sphere	NTHCOMP
MCG +8-11-11	10	1.77 ± 0.04	175^{+110}_{-50}	7.2 ± 0.2	(E)	0.754	0.51	5.6	60^{+110}_{-30}	$1.9^{\dagger} \pm 0.4$	sphere	NTHCOMP
Ark 564	11	2.27 ± 0.08	42 ± 3	6.8 ± 0.5	(H)	1.313	0.39	-	15 ± 2	$2.7^{\dagger} \pm 0.2$	sphere	NTHCOMP
PG 1247+267	12-13	2.35 ± 0.09	90^{+130}_{-35}	8.9 ± 0.2	(M)	0.024	0.79	0.05	46^{+60}_{-20}	$1.4^{\dagger} \pm 0.3$	sphere	NTHCOMP
Ark 120	14-15	1.87 ± 0.02	180^{+80}_{-40}	8.2 ± 0.1	(H)	0.085	0.92	2.3	-	-	-	-
NGC 7213	16	1.84 ± 0.03	> 140	8.0 ± 0.2	(G)	0.001	0.012	1.3	230^{+70}_{-250}	0.2 ± 0.1	sphere	COMPPS
MCG 6-30-15	17-18	2.06 ± 0.01	> 110	6.4 ± 0.1	(E)	0.238	0.056	5.5	-	-	-	-
NGC 2110	19	1.65 ± 0.03	> 210	8.3 ± 0.2	(K)	0.016	0.35	12.5	190 ± 130	0.2 ± 0.1	slab	COMPTT
Mrk 335	21-22	2.14 ± 0.03	> 174	7.2 ± 0.1	(H)	0.284	0.18	1.9	-	-	-	-
Fairall 9	20	1.95 ± 0.02	> 242	8.1 ± 0.7	(H)	0.054	0.60	2.9	-	-	-	-
Mrk 766	17-23-24	2.22 ± 0.03	> 441	6.3 ± 0.1	(I)	1.254	0.046	1.4	-	-	-	-
PG 1211+143	26	2.51 ± 0.2	> 124	8.2 ± 0.2	(H)	0.047	0.35	1.0	-	-	-	-

Notes. References: 1. Matt et al. (2015), 2. Baloković et al. (2015), 3.Marinucci et al. (2014a), 4.Malizia et al. (2008), 5. Bianchi et al. (2009), 6. Brenneman et al. (2014), 7. Lohfink et al. (2015), 8. Ballantyne et al. (2014), 9. Tortosa et al. (2017), 10. Tortosa et al. (2018), 11. Kara et al. (2017), 12. Lanzuisi et al. (2016), 13. Trevese et al. (2014), 14. Matt et al. (2014), 15. Porquet et al. (2017), 16. Ursini et al. (2015), 17. Marinucci et al. (2014b), 18. Emmanoulopoulos et al. (2014), 19. Marinucci et al. (2015), 20. Lohfink et al. (2016), 21. Parker et al. (2014), 22. Bianchi et al. (2001), 23. Buisson et al. (2017), 24. Risaliti et al. (2011), 25. Zoghbi et al. (2015), 26. Lawson & Turner (1997).

Mass References:A. Papadakis (2004), B. Onori et al. (2017), C. Pancoast et al. (2014, 2015),D. Winter et al. (2009), E.Bian & Zhao (2003b), F. Zhang & Wang (2006), G. Woo & Urry (2002), H. Peterson et al. (2004), I. Bentz et al. (2010), JHalpern (2006), K. Moran et al. (2007), L. Tortosa et al. (2017), M. Trevese et al. (2014), N de La Calle Pérez et al. (2010).

† Estimated parameter;

Table 6.2: Correlations factor, ρ and Null hypothesis probability, h_0.

X	Y	ρ	h_0	geometry
Γ	E_c	0.18	0.47	-
$\log(M_{bh}/M_\odot)$	E_c	-0.11	0.61	-
L_{bol}/L_{Edd}	E_c	-0.14	0.56	-
τ	kT_e	-0.88	0.004	slab
τ	kT_e	-0.63	0.02	sphere
$\log(M_{bh}/M_\odot)$	τ	-0.22	0.63	slab
$\log(M_{bh}/M_\odot)$	τ	-0.26	0.46	sphere
L_{bol}/L_{Edd}	τ	0.49	0.27	slab
L_{bol}/L_{Edd}	τ	0.38	0.28	sphere
$\log(M_{bh}/M_\odot)$	kT_e	0.20	0.64	slab
$\log(M_{bh}/M_\odot)$	kT_e	0.18	0.47	sphere
L_{bol}/L_{Edd}	kT_e	-0.37	0.41	slab
L_{bol}/L_{Edd}	kT_e	-0.36	0.32	sphere

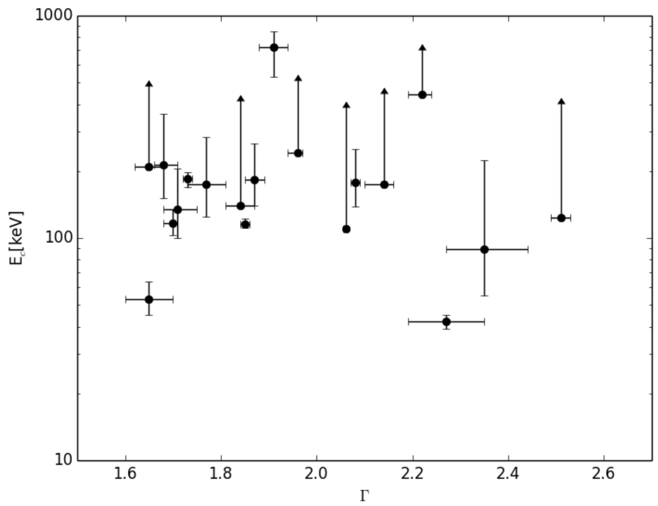

Figure 6.3: Plot of the high-energy cutoff vs the photon index of the sample.

for anti-correlation). In the fitting process also the "null hypothesis" is given. The null hypothesis, denoted by h_0, is the probability that sample observations result purely from chance. A small h_0 value indicates a significant correlation. The fits are made using the Interactive Data Language (IDL [1]) programming language. We fitted the parameters with a simple linear relation in logarithmic scale:

$$\log(y) = \mathbf{a}\log(x) + \mathbf{b} \tag{6.2}$$

The fits are made with a Monte Carlo method which repeated the fit procedure random sampling the values between a minimum value and a maximum value, which are identified respectively with the lower and the upper extreme of the errors of the measure, (**?**).

[1] www.harrisgeospatial.com/SoftwareTechnology/IDL.aspx

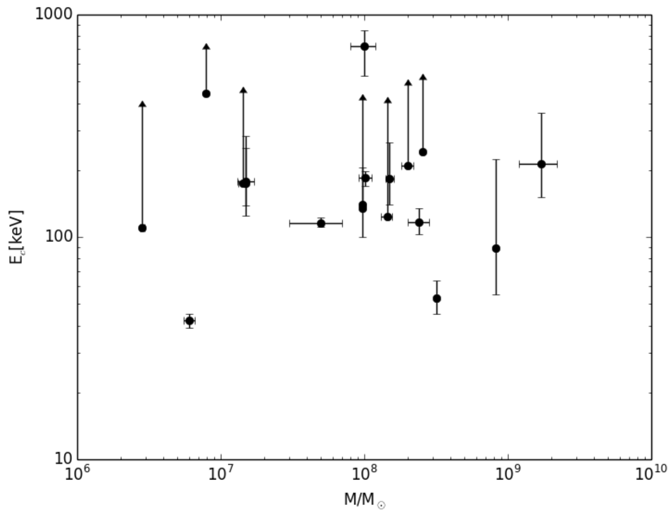

Figure 6.4: Plot of the high energy cutoff vs the black hole mass of the sample

6.2.1. SPECTRAL PARAMETERS

We started by looking for a correlation between the photon index Γ and the high-energy cutoff with the relation of Equation 6.2. As it can be seen in Figure 6.3, no statistically significant correlation is found between this parameters, in contrast with what was found by previous satellites (e.g., Perola et al. 2002; **?**). This is reassuring, suggesting that with *NuSTAR* with *NuSTAR*, and using a relatively large sample of well exposed sources with good measurements, the intrinsic degeneracy between these two parameters is significantly reduced.

The following step was to search for a linear correlation between the mass of the central black hole and the high energy cutoff and between the Eddington ratio and the value of the cutoff energy. All the values are reported in Table 6.1. The Spearman's ρ values, reported in Table 6.2, show that there is no significant correlation between the checked parameters.

6.2.2. PHYSICAL PARAMETERS

We consider the physical parameters that characterize the AGN coronae: the coronal temperature kT_e and the optical depth. The distribution of these two values in our sample is shown in Figure 6.6. It should be noted for some of the sources the optical depth parameter is not directly measured, since the model used (NTHCOMP in XSPEC) does not have the optical depth as free parameter. In these cases, the optical depth has been estimated using the relation from Beloborodov (1999):

$$\Gamma \approx \frac{9}{4} y^{-2/9} \tag{6.3}$$

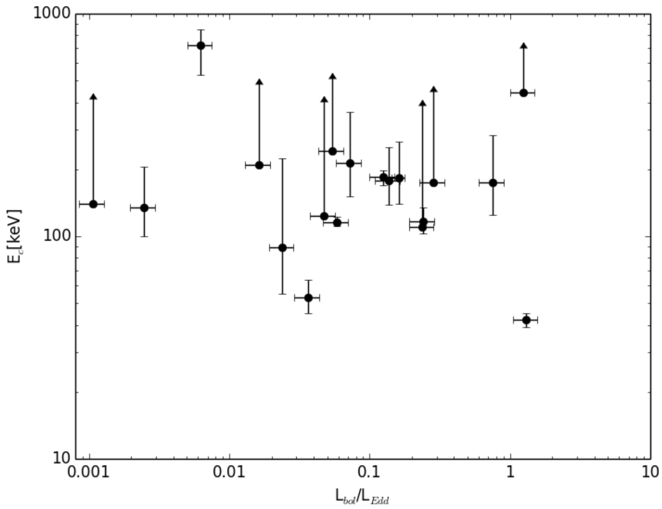

Figure 6.5: Plot of the high energy cutoff vs Eddington ratio of the sample

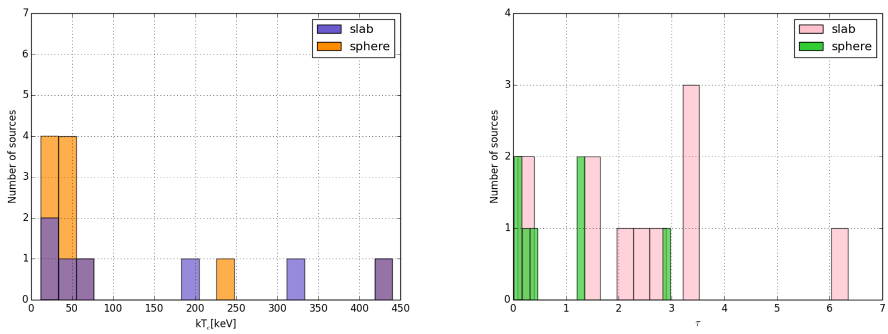

Figure 6.6: Left panel: the histogram of the distribution of the coronal temperature values for the sources of the sample that have coronal temperature measurements. Right panel: the histogram of the distribution of the optical depth values for the sources of the sample that have a direct or extrapolated measurements of this parameter. Both slab and sphere geometry of the corona are considered.

where Γ is the photon index of the spectrum between 2 and 10 keV. The dependence from the optical depth is in the relativistic y-parameter:

$$y = 4\left(\Theta_e + 4\Theta_e^2\right)\tau(\tau+1) \tag{6.4}$$

where Θ_e is the electron temperature normalized to the electron rest energy:

$$\Theta_e = \frac{kT_e}{m_e c^2} \tag{6.5}$$

We performed the fit for the two cases of slab and spherical geometry of the corona.

OPTICAL DEPTH VS CORONAL TEMPERATURE

The optical depth and coronal temperature appear to be extremely anti-correlated, the Spearman correlation factor for this fit is $\rho = -0.88/-0.63$ and the null hypothesis probability $h_0 = 0.004/0.03$, for the slab and spherical geometry respectively, see also Figure 6.7.

Using the equation 6.2 we found, in the case of a slab geometry, the following intercept and slope values for the fit:

$$\mathbf{a} = -0.7 \pm 0.1\ ;\ \mathbf{b} = 1.6 \pm 0.06 \tag{6.6}$$

The parameters of the linear regression in the case of the spherical geometry are:

$$\mathbf{a} = -0.7 \pm 0.2\ ;\ \mathbf{b} = 1.8 \pm 0.1 \tag{6.7}$$

This is a very interesting result, but the physical interpretation is not straightforward. We will discuss this correlation in the following section.

We also searched for correlations between the above parameters (coronal optical depth and coronal temperature) and the central black hole of the AGN, and the Eddington Ratio in both coronal geometries, slab and spherical. We do not found statistically significant correlation any of the analysed cases (see Table 6.2). It must be remarked that, in the case of the Eddington ratio vs the coronal temperature we found a trend which is similar to the modest anti-correlation between the Eddington ratio and the cutoff energy. This result is not surprising, giving the relation between the cutoff energy and the coronal temperature (Petrucci et al. 2000, 2001), but, as above, the anti-correlation is not statistically significant.

6.3. RE-ANALYSIS OF NGC 5506, GRS 1734-292 AND MCG -05-23-16

NGC 5506, GRS 1734-292 and MCG -05-23-16 have the most extreme values of coronal temperature of the sample. These values are obtained in literature using the COMPTT comptonization model (Titarchuk, 1994). We check the kT$_e$ and τ values in spherical geometry of the corona for the above sources by re-analysing the *NuSTAR* observations using the NTHCOMP model (Zdziarski et al. 1996 and Życki et al. 1999).

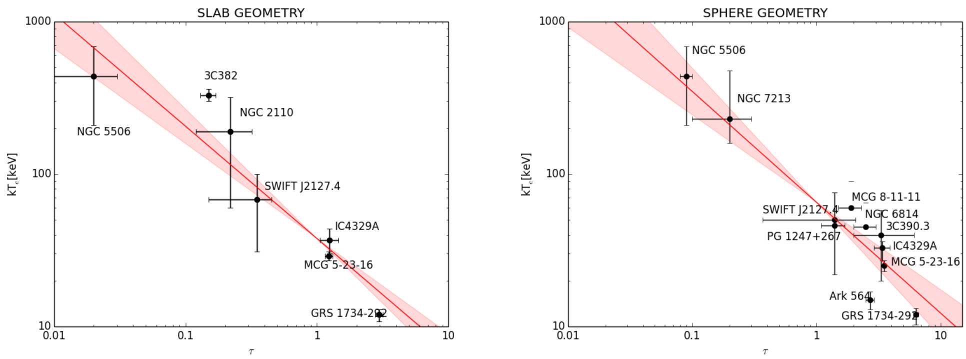

Figure 6.7: Fit and dispersion of the optical depth vs the electron coronal temperature in the case of a disc shape corona (top panel) and spherical corona (bottom panel).

NGC 5506 was observed with *NuSTAR* (OBSID 60061323) on 2014 April 1. The observation was coordinated with the *Swift* observatory (OBSID 00080413001), which observed the source, on 2012 April 2.In the re-analysis of NGC 5506, we fitted also the simultaneous *Swift*/XRT data, but we did not re-extract the *Swift*/XRT spectra.

GRS 1734-292 was observed by NuSTAR on 2014 September 16 (OBSID 60061279002), for a total elapsed time of 43 ks.

MCG -05-23-16 was observed on 2012 July 11–12 (OBSID 10002019), and on 2013 June 3–7 (OBSID 60001046). The first observation was conducted as a part of the *NuSTAR* calibration campaign. The second observation was a science observation carried out simultaneously with a long *Suzaku* observation. In our re-analysis we used only the *NuSTAR* science observation.

First we reduced again the old *NuSTAR* observations with the *NuSTAR* Data Analysis Software (NuSTARDAS) package (v. 1.6.0). Cleaned event files (level 2 data products) were produced and calibrated using standard filtering criteria with the NUPIPELINE task using the last new calibration files available from the *NuSTAR* calibration database (CALDB 20170120). The extraction radii of the circular region were 0.5 arcmin both for source and for background spectra, for all the sourced.

In their analysis of NGC 5506 Matt et al. (2015) found an X-ray spectrum composed by an absorbed power law (with $\Gamma \sim 1.9$) with an exponential high-energy cutoff ($E_c = 720^{+130}_{-190}$ keV), plus a moderately ionized reflection component, and ionized iron lines. They estimated the coronal parameters using the COMPTT comptonization model (Titarchuk, 1994), and the COMPPS model (Poutanen & Svensson, 1996b), founding, in the spherical geometry of the corona a coronal temperature of 440^{+230}_{-250} keV (~ 270 keV) and an optical depth of 0.09 (0.14) respectively.

Tortosa et al. (2017) found, for the *NuSTAR* spectra of GRS 1734-292, a spectral shape of an absorbed power-law with photon index of 1.65 and a very low exponential cutoff, 53^{+11}_{-8}keV. They found a reflection fraction of 0.48 ± 0.22 and no evidence of relativistic features. Using the COMPTT model and assuming a spherical geometry for the Comp-

Table 6.3: List of some parameters obtained from the re-analysis of NGC 5506, GRS 1734-292 and MCG -05-23-16.

Source	Γ	kT$_e$ (keV)	τ	χ^2/d.o.f.
NGC 5506	$1.73^{+0.09}_{-0.03}$	400 ± 200	0.21	1.1
GRS 1734-292	1.81 ± 0.04	16 ± 3	3.9	1.02
MCG -05-23-16	1.93 ± 0.01	41 ± 5	1.73	1.05

tonizing corona, they fond a coronal temperature of $12.1^{+1.8}_{-1.3}$ keV and an optical depth $\tau = 6.38^{+0.4}_{-0.5}$.

The analysis of the *NuSTAR* spectrum of MCG -05-23-16, made up by citetbalokovic15, showed a primary power-law with an exponential high energy cutoff at 116^{+6}_{-5}keV, a photon index of 1.85 ± 0.01 and the iron line with both narrow and broad component, the last one due to relativistic effects. COMPTT Comptonization model in the case of a spherical corona gives a coronal temperature kT$_e$ = 25 ± 2 keV and a coronal optical depth $\tau = 3.5 \pm 0.2$.

We used models similar to the ones of Matt et al. (2015), Tortosa et al. (2017) and Baloković et al. (2015) to fit the NGC 5506, GRS 1734-292 and MCG -05-23-16 data, but we used theRELXILLCP and XILLVER-COMP models (García & Kallman 2010; García et al. 2014 and Dauser et al. 2014) to model the relativistic or standard (respectively) reflection with the irradiation of the accretion by a power law with a NTHCOMP(Zdziarski et al. 1996 and Życki et al. 1999) Comptonization continuum.

The values obtained with the re-analysis are showed in Table 6.3. The coronal optical depth values are extrapolated using the relation from Beloborodov (1999). The values we found in our re-analysis are different from the literature values, especially the photon index Γ (and so the optical depth). However the error bars on the coronal temperature almost are still the same.

Even if the values we found are different from the literature ones, the τ-kT$_e$ pairs follow the relation found previously with the literature values (see Figure 6.8).

6.4. DISCUSSION

We found two relevant results from this analysis. The first one is the lack of correlation between the high-energy cutoff and the spectral photon index of the primary power law (see Figure 6.3). Perola et al. in 2002 found a correlation between the high-energy cutoff and the photon index of the primary power law with a correlation coefficient equal to 0.88, with E$_c$ increasing on average with Γ. The same correlation is found in the *Swift-BAT* sample, in which **?** found that fitting with a power-law model simulated *Swift*/BAT spectra varying the values of the high-energy cutoff, when the high energy cutoff decreases, the *Swift*/BAT photon index increase (see Figure 19 in their work).

Given that the two parameters are correlated in the fit procedure, this correlation may be an artifact due to any systematic error on one of the two parameters. Instead, we found no significant correlation between Γ and E$_c$. The lack of correlation between these parameters means that there are no large systematics in the *NuSTAR* measurements.

The second important result is the presence of a strong anticorrelation between the optical depth and the coronal temperature of the sample either in slab or spherical geometries.The interpretation of this anticorrelation is not trivial. Of course the values of the parameters are model dependent. We check the kT_e and τ values in spherical geometry of the corona for some of the sources of the sample, in particular GRS 1734-292, NGC 5506 and MCG -05-23-16, which have the most extreme values of temperature and optical depth, by re-analysing the *NuSTAR* observations. The coronal temperature and the optical depth of the three sources listed above are obtained in literature with the COMPTT model (Titarchuk, 1994). Instead we used the NTHCOMP model (Zdziarski et al. 1996 and Życki et al. 1999), see Section 6.3. We found different values for the two parameters of the three sources but even if the values are different, the τ-kT_e pairs follow the relation found with the literature values (see Figure 6.8). Although the values are different for the same source because they are obtained with different models, they still follow the anti-correlation.

Moreover, we note that the models used for the analysis of the different sources in the literature are not the same. This excludes the fact that the correlation could be an artefact due to the use of the same model for the analysis.

The τ-kT_e anti-correlation cannot be reconciled with a *fixed* disc-corona configuration in radiative balance. Indeed, such a configuration corresponds to a fixed cooling/heating ratio for the corona. In this case the corona temperature and optical depth have only to adjust themselves in order to ensure the constancy of this ratio. But there is no reason for kT_e and/or τ to change. In other words, if 1) the disc-corona configuration of all the Seyfert galaxies is the same and 2) is in radiative balance, we would expect kT_e and/or τ to cluster around the same values for all the objects of our sample.

The observed correlation indicate that one (or both) of these hypotheses is wrong. The invalidation of the former (same disc-corona configuration) implies a geometrical variation of the accretion flow. It could be the variations of the transition radius R_{tr} separating the inner corona and the outer disk or the variation of the height H of the corona above the disk, like in the lampost configuration. A smaller R_{tr}/H would imply a larger cooling from the disk and then a smaller temperature (assuming the heating is the same). In this case the observed anti-correlation would indicate that objects like NGC 5506 have a larger R_{tr}/H than objects like GRS 1734-292.

The invalidation of the radiative balance hypothesis, instead, could be due to, e.g., a variation of the intrinsic disk emission. Indeed, for a fixed disk-corona geometry, the radiative balance will change if the disk intrinsic emission varies, the larger the disk intrinsic emission, the larger the corona cooling and the smaller the temperature. In this case the observed anti-correlation would indicate that objects like NGC 5506 have lower disk intrinsic emission than objects like GRS 1734-292.

Note that for a pair-dominated corona, opposite behaviours are expected since an

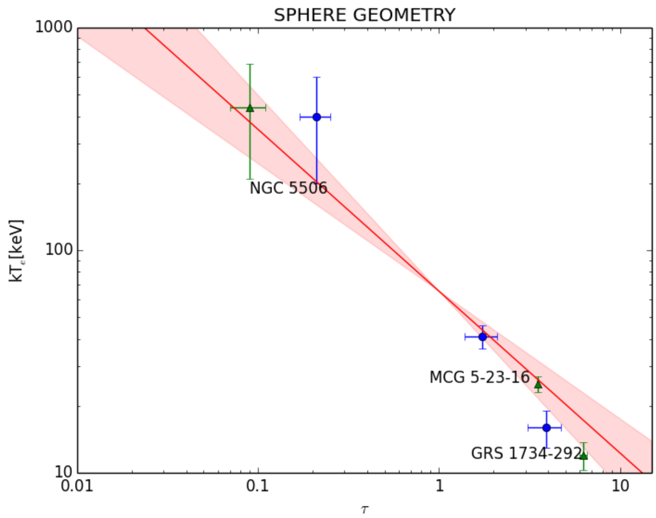

Figure 6.8: Fit and dispersion of the optical depth vs the electron coronal temperature in the case of a spherical corona, as in lower panel of Figure 6.7, with the superimposition of the literature values of optical depth and coronal temperature for GRS 1734-292, NGC 5506 and MCG -05-23-16 (blue circle) and the values obtained with our re-analysis (green triangle), see Section 6.3.

increase of the cooling (which is inversely proportional to the coronal optical depth, Haardt & Maraschi 1991) would correspond to an increase of the corona temperature and not a decrease (Ghisellini & Haardt, 1994). In consequence, to explain the observed $kT_e - \tau$ anti-correlation, objects with large corona temperatures would have a smaller R_{tr}(H) or a larger disk intrinsic emission than objects with low temperature.

6.5. CONCLUSIONS

We have presented and discussed the recent high-energy cutoff measurements in a sample of nineteen bright Seyfert galaxies observed by *NuSTAR* in collaboration with other X-ray observatories operating below 10 keV, such as *XMM-Newton, Suzaku* and *Swift*. The goal of the work is to look for correlation between spectral and physical parameters, to better understand the physics and the structure of AGN coronae.

This kind of analysis has been already done before the coming of *NuSTAR* using cutoff energy measurements made up by hard X-ray satellites like *Beppo-SAX* (Perola et al., 2002) and *INTEGRAL* (Malizia et al., 2014). Unlike *NuSTAR*, these instruments are non-focusing, and therefore background dominated for AGN observation.

We searched for correlations between the high-energy cutoff and the photon index of the primary power-law, the mass of the central black hole and the Eddington ratio, i.e. L_{bol}/L_{Edd}. We did not found any statistically significant correlation between there parameters. Sources with lower limits on the cutoff energy show very high coronal temperature, when Comptonization models are applied. Some of the objects show a very hot corona and a low accretion rate, indicating that in these sources a possible Compton cooling inefficiency may play a role. Anyway, the existence of a linear correlation between these parameters is not jet confirmed with high significance. We can not rule out the presence of a more complex relationship between these parameters, but to find it more data are needed.

Finally, we search for the correlation between the physical parameters which characterize the hot coronae of AGN: the temperature the optical depth of the plasma of relativistic electrons which compose the corona with the mass of the central black hole and the Eddington ratio. No significant statistical correlation is found between these parameters except for the case of the optical depth versus the coronal temperature fit, for which we underline the presence of a strong anti-correlation. We found an anti-correlation with a Spearman correlation coefficient $\rho = -0.88$ in the case of a slab geometry of the corona and -0.63 in the case of a spherical corona. The significance level for ρ deviating from zero is equal to 0.004 in the case of slab geometry and 0.02 for the sphere geometry. The observed anti-correlation suggests a disk-corona configuration in radiative equilibrium, but requires differences, from source to source, in either the disk-corona configuration or in the intrinsic disk emission.

6.6. FUTURE PERSPECTIVE

To increase our knowledge of the AGN corona further work is clearly needed. This is why we are planning to make a comparison between our results and theoretical models. This analysis will be done in collaboration with the Academy of Sciences of the Czech Republic where a new Monte Carlo code for Comptonization, called MoCa, is being developed. The aim of the project is to derive the physical parameters of the corona by systematically comparing the observed spectra with the simulated ones. With respect to the semi-analytical Comptonization models currently available, the Monte Carlo code has the advantage not to be limited to relatively small optical depths, as the observations seem to indicate a large spread of values for this parameter.

7

Concluding Remarks

"Everything is theoretically impossible,
until it is done."

Robert A. Heinlein

In this section, we summarize the works that have been presented throughout this thesis.

The project has been discussed in Chapter 4 - 6 and can be summarized as follows:

1. Chapter 4 discusses the broadband X-ray spectrum of GRS 1734-292 obtained from non-simultaneous *XMM-Newton* and *NuSTAR* observations, performed in 2009 and 2014, respectively. From the analysis carried out in this chapter it emerges that the spectral slope of the primary power law is different between the two observations, being very flat in the *XMM-Newton* observation ($\Gamma \sim$1.47) while it is more typical of a Seyfert galaxy in the *NuSTAR* observation ($\Gamma \sim$1.65), when the source was a factor of $\sim$ 1.3 brighter. The analysis shows a cutoff energy for the source of 53^{+11}_{-8} keV. This is the lowest value found so far by *NuSTAR* in a Seyfert galaxy together with Mrk 335 (Keek & Ballantyne, 2016); comparable or even lower values are found in stellar-mass accreting black holes (Miller et al. 2013; Miller et al. 2015). In the analysis we estimated the coronal parameters by fitting the *NuSTAR* data with Comptonization model, finding a coronal temperature of $kT_e = 12.1^{+1.8}_{-1.28}$ keV and an optical depth $\tau = 2.8^{+0.2}_{-0.3}$ assuming a slab geometry, or a similar temperature and $\tau = 6.38^{+0.4}_{-0.5}$ assuming a spherical geometry. Given the low coronal temperature, GRS 1734-292 is located far away from the region of pair production in the Θ_e - ℓ plane, and is also located well below the $e^- - e^-$ coupling line (i.e. the line below which the electron-electron coupling time scale is shorter than the Compton cooling time scale). This should ensure that the electron population is thermalized. It is instead located close to the $e^- - p$ coupling line, below which the electron-proton coupling time scale is shorter than the Compton cooling time scale. It is interesting to note that no sources among those analysed by Fabian et al. (2015) lie definitely below the $e^- - p$ line, while a number of them lie

around or just above (see Fig. 4 in their paper). This line, therefore, seems to set a physical boundary, which may be understood, at least qualitatively. If the electron population cools by Compton scattering and its temperature decreases until the electron-proton coupling becomes important, the transfer of energy from protons to electrons becomes effective. This is not a completely self-consistent picture, as the electron-proton coupling line was calculated assuming that the electron and proton temperatures (normalized to their mass), Θ_e and Θ_p, are the same (Fabian, 1994), which is unlikely when Compton cooling dominates. Moreover, the dependence of the coupling time on Θ_e is small as soon as the two temperatures are decoupled and the proton temperature is the largest. Time-dependent, detailed calculations with realistic heating and energy redistribution mechanisms are required to assess how effective this feedback may be. Only a few AGN in the Fabian et al. (2015) compilation have temperatures as low as that of GRS 1734-292, and none among those observed by *NuSTAR*. We note that the accretion rate of GRS 1734-292 is only a few percent of the Eddington limit, so the effectiveness of the cooling mechanism cannot be related to a particularly strong radiation field. It may, however, be at least partly related to the high value of the optical depth τ. A seed photon coming from the disc, in fact, will undergo more than one scattering before leaving the corona, thereby reducing the electron temperature. Indeed, models predict an anti-correlation between coronal temperature and optical depth (see e.g. Petrucci et al. 2001 for a calculation based on the two-phase model of Haardt & Maraschi (1993): note that values not too different from ours are predicted). The reason for the unusually large value of the optical depth is unclear (but see Keek & Ballantyne (2016) for evidence of an increase of the optical depth with decreasing Eddington ratio in Mrk 335), and difficult to assess given our poor knowledge of the processes which originate the corona and of the mechanisms which transfer the energy there. But with the increasing amount of high-quality spectra from *NuSTAR*, progressively populating this parameter space, it is at least possible to start seriously pondering these questions.

2. Chapter 5 discusses the *NuSTAR* observations of MGC +8-11-11 (100 ks) and of NGC 6814 (150 ks). Thanks to the *NuSTAR* sensitivity at high energies, it was possible to measure the high-energy cutoff value for both sources; in the work, we found 175^{+110}_{-50} keV and 155^{+70}_{-35} respectively for MCG +8-11-11 and NGC 6814. We found also a disc reflection component and we constrained the reflection fraction founding 0.25 ± 12 for MCG +8-11-11 and of $0.27^{+0.10}_{-0.12}$ for NGC 6814. Both sources showed a slightly broadened relativistic Fe Kα line plus a narrow component. The reflection component was modest and mostly associated with the broad line component. The low reflection fraction found in MCG +8-11-11 was consistent with the value found by Mantovani et al. (2016). During the analysis, we estimated the

coronal parameters by fitting the *NuSTAR* data with a model which takes into account both the relativistic and non-relativistic reflection when illuminated by a thermally Comptonized continuum. We found a coronal temperature of 60^{+110}_{-30} keV for MCG +8-11-11 and 45^{+100}_{-17} keV for NGC 6814. It is interesting to note that the coronal temperature of the two sources is very similar despite an order of magnitude difference in mass and Eddington ratio. We put MCG +8-11-11 and NGC 6814 in the compactness-temperature (Θ_e - ℓ) diagram (Fabian et al. 2015). Both sources are positioned under the Svensson pair runaway line for a spherical geometry (Svensson, 1984), above the $e^- - e^-$coupling line, like most of the sources among those analysed by Fabian et al. (2017). The pair runaway line in the Θ_e - ℓ diagram is a curve which determines a forbidden region in which the pair production exceeds the annihilation. The detailed shape of this line depends on the source of soft photons and on the radiation mechanism. Above the $e^- - e^-$coupling line the $e^- - e^-$ coupling time scale is longer than the Compton cooling time scale. The location of these sources within the Θ_e - ℓ plane fits well in the scenario in which the AGN spectral shape is controlled by pair production and annihilation.

3. In Chapter 6 we discussed the ongoing project whose aim is the analysis of a sample of AGN to derive the physical parameters of the corona and look for correlations between coronal temperature and other physical parameters. The fundamental parameters describing coronal spectrum of an AGN are the rollover energy and the slope of the primary power-law, so in this work we presented and discussed the recent high-energy cutoff measurements in a sample of nineteen bright Seyfert galaxies observed by *NuSTAR* in collaboration with other X-ray observatories operating below 10 keV, such as *XMM-Newton, Suzaku* and *Swift*. We found no significant correlation between the high-energy cutoff and the spectral photon index of the primary power law. The lack of correlation between these parameters means that there are no systematics in the measure of these parameters. We analysed also the presence of a correlation between the high-energy cutoff and the mass of the central black hole and the Eddington ratio, i.e. $L_{bol}Ł_{Edd}$. Sources with lower limits on the cutoff energy show very high coronal temperature, when Comptonization models are applied. Some of the objects show a very hot corona and a low accretion rate, indicating that in these sources a possible Compton cooling inefficiency may play a role.Anyway, the existence of a linear correlation between these parameters is not confirmed. We can not rule out the presence of a more complex relationship between these parameters, but to find it more data would be needed. Finally, we underline the presence of a strong anti-correlation between the physical parameters which characterize the hot coronae of AGN: the temperature the optical depth of the plasma of relativistic electrons which compose the corona. We found an anti-correlation with a Spearman correlation coefficient $\rho = -1.0$ in the

case of a slab geometry of the corona and -0.79 in the case of spherical corona. The significance level for ρ deviating from zero is comfortably lower and equal to 0.0 in the case of slab geometry and 0.0019 for the sphere geometry.

All the above results were obtained in order to constrain the coronal parameters and to have an overview of the physics and the structure of the hot corona of AGN. To increase our knowledge of the AGN corona further work is clearly needed. This is why we are planning to make a comparison between our results and theoretical models. This analysis will be done in collaboration with the Academy of Sciences of the Czech Republic where a new Monte Carlo code for Comptonization, called MoCa, is being developed. The aim of the project is to derive the physical parameters of the corona by systematically comparing the observed spectra with the simulated ones. With respect to the semi-analytical Comptonization models currently available, the Monte Carlo code has the advantage not to be limited to relatively small optical depths, as the observations seem to indicate a large spread of values for this parameter.

A

XSPEC: AN X-RAY FITTING PACKAGE

In this work I used the **XSPEC version: 12.9.0** for the analysis of *XMM-Newton*, *Swift* and *NuSTAR* spectra.

XSPEC (Arnaud, 1996) is a command-driven, interactive, X-ray spectral-fitting program, designed to be completely detector-independent so that it can be used for any spectrometer. XSPEC has been used to analyze data from *HEAO*-1 A2, *Einstein Observatory*, *EXOSAT*, *Ginga*, *ROSAT*, *BBXRT*, *ASCA*, *CGRO*, *IUE*, *RXTE*, *Chandra*, *XMM-Newton*, *Integral/SPI*, *Swift*, *Suzaku* and *NuSTAR*.

XSPEC is distributed and maintained under the aegis of the GSFC High Energy Astrophysics Science Archival Research Center (HEASARC).It can be downloaded as part of HEAsoft from `http://heasarc.gsfc.nasa.gov/docs/software/lheasoft/download.html`.

The first version of XSPEC was written in 1983 at the Institute of Astronomy, Cambridge, under VAX/VMS by Rick Shafer. It was written to perform spectral analysis of data from the ESA *EXOSAT X-ray observatory*, which was launched that year.

In XSPEC12, spectra can be fitted with more than one distinct model simultaneously, on condition that at each separate model components can be assigned distinct response functions, such as with coded aperture masks.

A.1. THE BASICS OF SPECTRAL FITTING

Although we use a spectrometer to try to find out the spectrum of a source, what the spectrometer obtains is not the actual spectrum, but rather photon counts (C) within specific instruments channels, (I). This observed spectrum is related to the spectrum of the source, $f(E)$, in this way:

$$C(I) = \int_0^\infty f(E)R(I,E)dE \tag{A.1}$$

where $R(I,E)$ is the instrumental response and it is proportional to the probability that an incoming photon of energy E will be detected in the channel I. Ideally, then, we would like to determine the actual spectrum of a source, $f(E)$, by inverting this equation, thus deriving $f(E)$ for a given set of $C(I)$. Regrettably, this is not possible in general, as such inversion tend to be non-unique and unstable to small changes in C(I).

Table A.1: Constants for calculating confidence regions, taken from Avni (1976).

Confidence	$\Delta\chi^2$		
	1	2	3
0.68	1.00	2.30	3.50
0.90	2.71	4.61	.25
0.99	6.63	9.21	11.30

The usual alternative is to try to choose a model spectrum, $f(E)$, that can be described in terms of few parameters, i.e., $f(E, p1, p2, ..)$, and match, or *fit* it to the data obtained by the spectrometer. For each $f(E)$, a predicted count spectrum, $C(p(I))$, is calculated and compared to the observed data, $C(I)$. Than a *fit statistic* is computed from the comparison, which enables one to judge whether the model spectrum *fits* the data obtained by the spectrometer.

The model parameters then are varied to find the parameter values that give the most desirable fit statistic. These values are referred to as the *best-fit parameters*. The model spectrum, $f_b(E)$,made up of the best-fit parameters is considered to be the best-fit model.

The most common fit statistic in use for determining the best-fit model is χ^2, defined as follows:

$$\chi^2 = \sum \frac{(C(I) - C_p(I))^2}{(\sigma(I))^2} \tag{A.2}$$

where $\sigma(I)$ is the error for channel I, if $C(I)$ are counts then $\sigma(I)$ is usually estimated by $\sqrt{C(I)}$.

Once a best-fit model is obtained, we have to investigate the level of confidence that the observed $C(I)$ is, being produced by the best-fit model $f_b(E)$. The χ^2 statistic provides a well-known-goodness-fit criterion for a given number of degrees of freedom (ν, which is calculated as the number of channels minus the number of model parameters) and for a given confidence level. If χ^2 exceeds a critical value (tabulated in many statistics text) one can conclude that $f_b(E)$ is not an adequate model for $C(I)$. As a general rule, one wants the *reduced* χ^2 (defined as: χ^2/ν) to be approximately equal to one ($\chi^2 \sim \nu$).

For a given best-fit parameter, p1, we determine the range of values within which one can be confident the true value of the parameter lies. We have to define the *confidence-interval* for the parameter.

The confidence interval for a given parameter is computed by varying the parameter value until the χ^2 increase by a particular amount above the minimum, or best-fit value. The amount that the χ^2 is allowed to increase (also referred to as the critical $\Delta\chi^2$) depends on the confidence level one requires, and on the number of parameters whose confidence space is being calculated. (See Table A.1).

A.2. THE XSPEC IMPLEMENTATION

To summarize the preceding section, the main components of spectral fitting are as follows:

- a set of one or more observed spectra $D(I)$ with background measurements $B(I)$ where available;
- the corresponding instrumental response $R(I,E)$;
- a set of model spectra $M(E)$.

These components are used as follows:

- a parametrized model is created assumed to represents the actual spectrum of the source;
- values to the model parameters are introduced;
- based on the parameters values given, one predicts the counts spectrum that would be detected by the spectrometer in a given channel for such a model;
- then, one compares the predicted spectrum to the spectrum actually obtained by the instrument;
- the values of the parameters of the model are manipulated until one finds the best fit between the theoretical model and the observed data.

To obtain each observed spectrum, $C(I)$, XSPEC uses two files: the data (spectrum) file, containing $D(I)$, and the background file, containing $B(I)$. The data file tells XSPEC how many total photon counts were detected by the instrument in a given channel. XSPEC then uses the background file to derive the set of background-subtracted spectra $C(I)$ in units of counts per second. The background-subtracted count rate is given by, for each spectrum:

$$C(I) = \frac{D(I)}{a_{D(I)}tD} - \frac{b_{D(I)}}{b_{B(I)}}\frac{B(I)}{a_{bI)}t_B} \tag{A.3}$$

where $D(I)$ and $B(I)$ are the counts in the data and background files; t_D and t_B are the exposure times in the data and background files; $b_{D(I)}$ and $b_{B(I)}$, $a_{D(I)}$ and $a_{B(I)}$ are the background and area scaling values from the spectrum and background respectively, which together refer the background flux to the same area as the observation as necessary. When this is done, XSPEC has an observed spectrum to which the model spectrum can be fit.

Before XSPEC can take a set of parameter values and predict the spectrum that would be detected by a given instrument, the specific characteristics of the instrument must be given. This information is known as the detector response. Recall that for each spectrum the response $R(I,E)$ is proportional to the probability that an incoming photon of energy E will be detected in channel I. As such, the response is a continuous function of E. This continuous function is converted to a discrete function by the creator of a response matrix who defines the energy ranges E_j such that:

$$R_D(I,J) = \frac{\int_{E_{J-1}}^{E_J} R(I,E)dE}{E_J - E_{J-1}} \tag{A.4}$$

XSPEC reads both the energy ranges, E_J, and the response matrix $R_D(I,J)$ from a response file in a compressed format that only stores non-zero elements. XSPEC also includes an option to use an auxiliary response file, which contains an array $A_D(J)$ that is multiplied into $R_D(I,J)$ as follows:

$$R_D(I,J) \to R_D(I,J) \times A_D(J) \tag{A.5}$$

This array is designed to represent the efficiency of the detector with the response file representing a normalized Redistribution Matrix Function, or RMF. Conventionally, the response is in units of cm^2.

The model spectrum, $M(E)$, is calculated within XSPEC using the energy ranges defined by the response file:

$$M_D(J) = \int_{E-J-1}^{E_J} M(E)dE \tag{A.6}$$

and is in units of photons/cm^2/s. XSPEC allows the construction of composite models consisting of additive components representing X-ray sources (e.g., power-laws, blackbodies, and so forth), multiplicative components, which modify additive components by an energy-dependent factor (e.g., photoelectric absorption, edges, ...). Convolution and mixing models can then perform sophisticated operations on the result. Models are defined in algebraic notation.

A.3. Fits and Confidence Intervals

Once data have been read in and a model defined, XSPEC uses a fitting algorithm to find the best-fit values of the model parameter. The default is a modified Levenberg-Marquardt algorithm (based on CURFIT from Bevington 1969). The algorithm used is local rather than global, so it is possible for the fitting process to get stuck in a local minimum and not find the global best-fit. The process also goes much faster (and is more likely to find the true minimum) if the initial model parameters are set to sensible values.

The Levenberg-Marquardt algorithm relies on XSPEC calculating the 2nd derivatives of the fit statistic with respect to the model parameters. By default these are calculated analytically, with the assumption that the 2nd derivatives of the model itself may be ignored.

At the end of a fit, XSPEC will write out the best-fit parameter values, along with estimated confidence intervals. These confidence intervals are one sigma and are calculated from the second derivatives of the fit statistic with respect to the model parameters at the best-fit. These confidence intervals are not reliable and should be used for indicative purposes only. XSPEC has a separate command (error or uncertain) to derive confidence intervals for one interesting parameter, which it does by fixing the parameter of interest at a particular value and fitting for all the other parameters. New values of the parameter of interest are chosen until the appropriate delta-statistic value is obtained. XSPEC uses a bracketing algorithm followed by an iterative cubic interpolation to find the parameter value at each end of the confidence interval.

To compute confidence regions for several parameters at a time, XSPEC can run a grid on these parameters. XSPEC also will display a contour plot of the confidence regions of any two parameters.

XSPEC is designed to support multiple input data formats. Support for the earlier SF and Einstein FITS formats are removed. Support for ASCII data is planned, which will allow XSPEC to analyze spectra from other wavelength regions (optical, radio) transparently to the user.

B

Data Processing

Here I describe the processing procedure applied for the observatories which are used in this thesis: *XMM*-Newton, *Swift/XRT* and *NuSTAR*. The spectral analysis of the spectral products obtained in the way described in this Appendix is performed with XSPEC version 12.9.0, described in Appendix A.

B.1. *XMM-Newton* Data Reduction

The *XMM-Newton* scientific data is organized in the Observation Data Files (ODF) and Slew Data Files (SDF), most of these files have a FITS format. The ODF/SDF files contain uncalibrated files. To perform scientific analysis of *XMM-Newton* data, specific *XMM-Newton* data reduction and analysis software are available.

The reduction of *XMM-Newton* spectra was performed by means of the Science Analysis System (SAS[1]) software package.

SAS is a collection of tasks, scripts, and libraries, specifically designed to reduce and analyze data collected by the *XMM-Newton* observatory. SAS is necessary to extract standard and/or customized science products, such as spectra, images, light curves. The version of SAS applied in this study is the SAS v.15.0.0.

The *XMM-Newton* data have been processed using the tasks `emchain` and `epchain` (for MOS and PN respectively) in order to obtain calibrated and concatenated event list.

XMM-Newton can also focus charged particles on the detection plane. Before the launch of the instrument, the capability of X-ray telescopes to focus electrons was already known, therefore they were equipped with magnetic diverters in order to deflect such electrons outside of the detection plane. In addition, the first observations of XMM-Newton revealed that the instrument is also able to focus soft protons, with $E \lesssim 300$ keV. These protons, of likely solar origin (e.g., Carter & Read 2007), lose energy for each interaction with the mirrors and are able to contaminate the higher energies ($E \gtrsim 10$ keV) of the detected spectrum, since they are almost undistinguishable from the actual X-rays, making it impossible to reject them a priori.

While the EPIC instruments are well protected by the magnetic diverters when the

[1] `https://www.cosmos.esa.int/web/xmm-newton/sas`

satellite crosses the radiation belt, in which the soft protons are obviously more common, this effect is also observed above the radiation belt limit, where the instruments are fully operative. The effect is seen as a sudden increase, known as *soft proton flare* (SPF), of the background level, that can prevail over the regular background by several orders of magnitude. Moreover, SPFs are unpredictable and the duration ranges from hundreds of seconds up to hours (De Luca & Molendi, 2004).

Since these background flares have a catastrophic effect on the detected X-ray spectrum of all three EPIC cameras aboard XMM-Newton, it is imperative to remove these events during the data reduction process.

This is done by using the command `evselect` which examine the count-rate of such events, by selecting all those single-pixel events (i.e., PATTERN==0) in the energy range that is sensitive to soft proton flares.

Lightcurves are generated running the command `lcurve`. The SPFs are then removed from the data with a manual inspection of the light curve, getting rid of all data in the time bins where the count rate exceeds the appropriate values counts/s; this value is estimated in such a way that the average count rate is all contained within that value. The selection is done by running the command `tabgtigen` that creates a Good Time Interval (GTI) event list for nonflaring events. A filtered event list is then created with the command `evselect`. With the adequate options, the command `evselect` generates an image of the X-ray observation, once the event list is appropriately cleaned of soft proton flaring events. The resulting image can be read by several software, e.g. **ds9**[2].

The next step is the selection of the appropriate area in which the source data is likely located, and the selection of the background area. Now we are able to extract a source and background spectrum from the image, by using again the command `evselect`.

At this point, we need to generate the Redistribution Matrix File (RMF). The convolution from energy space into detector space involves a spreading of the observed counts by the detector resolution, which is expressed by a matrix multiplication. While for gratings instruments, such as the two RGS cameras of *XMM-Newton*, this matrix is almost diagonal, it is not the case of CCD cameras, such as the three EPIC cameras. Therefore we must generate an RMF by using the command `rmfgen`.

Another fundamental tool to analyze the spectrum of a source is the Auxiliary Response File (ARF), that contains the combined areas of the telescope, filter and detector, the so-called *effective area*, and the quantum efficiency (QE) as a function of energy averaged over time. While the effective area is measured in cm^2, and the QE is measured in counts/photons, these two quantities are multiplied to create the ARF, which is then measured in cm^2 counts/photon. The ARF is generated with the command `arfgen`.

When the input spectrum is multiplied by the ARF, the result will be the distribution of counts as would be seen by a detector with ideal resolution in energy. Then, the RMF

[2] http://ds9.si.edu/site/Home.html

is needed, in order to produce the final spectrum. All these files can be compressed into a single file, easily readable by spectrum analysis program XSPEC (Arnaud, 1996), using the SAS tool `specgroup`, by which we can specify the number of photons for each bin with the `mincounts` option. If the number of counts is very high, we take the risk to oversample the instrument resolution, which is to be avoided, since we cannot have bins that are closer in energy than the energy resolution of the instrument. A minimum energy width of each bin can be forced by introducing the parameter oversample.

The output spectrum file takes into account the ARF, the RMF, and the background file, and it is readable by spectral analysis program XSPEC. The spectrum has also been grouped using the FTOOLS command `grppha` to a minimum of 30 counts per bin, to facilitate the use of the χ^2 minimization technique using XSPEC.

B.2. *Swift/XRT* DATA REDUCTION

Swift/XRT data are processed with the `xrtpipeline` tool along with HEASARC remote CALDB and standard filters. It produces the cleaned event-file and image. Image are extracted using XSELECT. XSELECT is a command line interface to the extractor and can be used to extract images, light-curves and spectra (among other things) from the event lists. Images are extracted within the full energy range of the XRT: about 0.2 – 10 keV. However, the data can be filtered to produce images over any energy band within this range, using the command `filter pha_ cutoff`, where the range must be given in terms of channels. For the XRT, 1 channel =10 eV.

Source and background regions should be defined within **ds9**; circular regions can be used. If `xrtpipeline` was run with `cleanup=no`, the region produced (a 20 pixel radius circle) can be used if the source is not piled-up.

The task `read event` is used to read the event file which will be filtered with the `fitered region` command. The `extract spectrum` is used to extract the filtered spectrum.

Exposure maps are used to correct for the loss of flux caused by some of the CCD pixels not being used to collect data. The Swift software allows the user to correct for the loss of flux which occurs when the source is positioned over a hot column. When running `xrtpipeline`, the command `createexpomap=yes` will produce an exposure map for each full event list.

Although the RMFs are obtained from the CALDB as ready-made files, ARFs need to be created for every extracted spectrum. To do this, the task called `xrtmkarf` is used. Generally, an exposure map should be used, corresponding to the same time interval as the spectrum. When an exposure map is included, the PSF correction must be active (i.e. `yes` as the input to the second `xrtmkarf` prompt); this ensures the ARF is corrected for hot columns, bad pixels and any loss of counts caused by using an annular extraction region (if the source is piled-up). If -1 is given at the prompts for the source coordinates, the position of the source is extracted from the header of the spectrum (and will, thus, correctly be the center of the extraction region used).

The spectrum, the background spectrum, the ancillary response function and the redistribution matrix files need to be linked together with the `grppha` task of FTOOLS.

PILE-UP

If the measured count rate is high (above about 0.6 count s-1 in photon counting mode is a rough guide), then the easiest way to avoid problems related to pile-up is to extract spectra using an annulus, thus eliminating the counts in the bright core, where pile-up will occur. To estimate the level of pile-up (i.e., how much of the core needs to be excluded), one needs to determine where the observed Point Spread Function (PSF) deviates from the known, un-piled-up PSF. In the absence of pile-up, the Swift PSF can be modeled by a King function:

$$PSF(r) = \left[1 + \left(\frac{r}{r_c}\right)^2\right]^{-\beta} \tag{B.1}$$

where, for *Swift*, $r_c \sim 5.8$ and $\beta \sim 1.55$ (Moretti et al., 2005).

A quick and simple method to estimate the size of the annulus required can be performed within XIMAGE running the `psf` command after extracting an image for the time period of interest. At this point, one should click first in the center of the object to be analysed, and then again at the outer edge of the object. This will bring up an interactive plot window, showing two plots: the encircled energy fraction and the PSF. The PSF profile can be fitted with the King function, as described above, but out in the wings, where pile-up will definitely not be an issue (see Figure B.1). Noticing all the data will then show where the points begin to lie beneath the extrapolation of the King function; this is the approximate radius which should be excluded to avoid the pile-up. Although

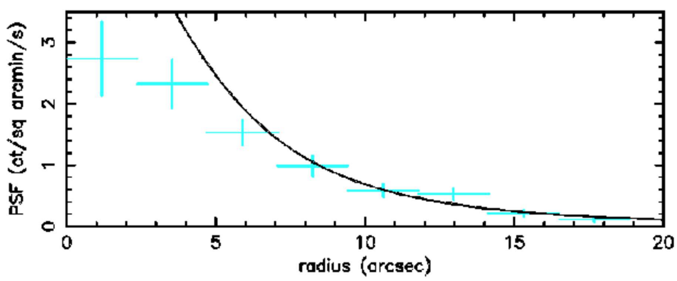

Figure B.1: An example of PSF profile (cyano) fitted with the King function (black).In this example, data within about 7 arcsec (1 XRT pixel = 2.36 arcsec) should be excluded when extracting spectra and light-curves.

the ARFs generated using `xrtmkarf` will correct the flux of the spectrum for the loss of counts caused by using an annulus, the correction for the actual count rate (and, hence, light-curve points) needs to be determined separately.

B.3. *NuSTAR* DATA REDUCTION

The starting point for the *NuSTAR* processing data is the level 1 data: telemetry data from the space satellite processed into the FITS format. To produce cleaned, calibrated event list files and standard high-level scientific products starting from level 1 FITS formatted telemetry data is used the NUSTARDAS command `nupipeline`[3] on the FPMA and FPMB *NuSTAR* Event Files. It runs in sequence the tasks for *NuSTAR* data processing. The `nupipeline` data processing is organized in three distinct stages for calibration, data screening and extraction of high-level scientific products:

- Data Calibration: processing of FITS formatted telemetry to produce calibrated event files.
- Data Screening: filtering of calibrated event files, by applying cleaning criteria on specified attitude/orbital/instrument parameters and event properties, to produce cleaned event files. Exposure maps are also generated.
- Products Extraction: extraction of high-level scientific products (light-curves, spectra, images, ARF and RMF files) from cleaned event files.

This task is broken down into two main sub-stages: (1) data calibration; and (2) data screening. Summarised below are the processing steps for the calibration stage, which make use of instrument calibration data from the calibration database (CALDB).

- Data from the on board laser metrology system are used to process information tracking temporal changes in the relative alignment of the optics and the focal plane detectors.
- Attitude data is processed, using information from the star trackers (the star tracker on the optics bench provides a pointing accuracy of $\pm 8''$).
- Known bad pixels and detected hot pixels are flagged, to be excluded at the screening stage.
- The events in the level 1 data each have a 3×3 nine-pixel signal pattern (the center of which is the pixel with the largest registered pulse height). For each event, pulse height amplitude (PHA; i.e., the charge in electronic units) information is processed, and a "grade" is assigned which characterizes the morphology of the 3×3 signal pattern (from grade 0 to grade 32). Grades $27-32$ are excluded at the screening stage (these particular four and five pixel patterns are less likely to be caused by real X-ray events).
- A gain correction (or energy correction) is performed for each event to convert from PHA to pulse invariant units (PI; i.e., the charge in physical energy units). The

[3] `https://heasarc.gsfc.nasa.gov/docs/nustar/analysis/`

conversion is dependent on the pixel, the grade, and the detector temperature. PI is related to photon energy (E; in units of keV) by the following:

$$PI = \frac{E - 1.6}{0.04} \tag{B.2}$$

- An "interaction depth" threshold is applied to flag internal background and cosmic ray events (to be excluded at the screening stage). $E < 60$ keV events from focused astrophysical sources have shallow interaction depths.

- The physical coordinates of each event are converted to sky coordinates (Harp et al. 2010 details the pointing reconstruction procedure). First focal plane bench frame coordinates (`DET1X`, `DET1Y`) are assigned probabilistically based on the grade and the detector pixel coordinates (`RAWX`, `RAWY`). Next the `DET1X` coordinates are converted to optics bench frame coordinates (`DET2X`, `DET2Y`) based on the mast aspect solution (from the laser metrology information; see above). The `DET1` and `DET2` coordinate systems use integer coordinates with effective pixel sizes which are finer by a factor of five than the raw detector pixels (meaning an effective pixel size of 12.3"/5 = 2.46" in the focal plane). Finally, the `DET2` coordinates are converted to celestial sky coordinates (X, Y) using attitude information (see above).

The above results in a calibrated event list, to which the screening stage is then applied. This involves excluding "bad" time intervals, including: when the Earth is in the FoV; when the telescope boresight is pointed $\leqslant 3°$ from the Earth's limb; when the observatory is passing through the South Atlantic Anomaly (SAA); when the attitude reconstruction is not from the optics bench star tracker, or its quality is low; when at least one of the mast-tracking laser spots is outside its associated position sensing detector grid; or when there is instrument dead time, due to the event-processing time of the focal plane module electronics or due to an anti-coincidence shield veto. Additionally, bad events are excluded: those associated with bad or hot pixels; those with grades $\geqslant 27$; those with large interaction depths; and those with PI values outside of the standard range. The above results in a cleaned and calibrated, level 2, event list.

Once individual *NuSTAR* sources have been identified in the imaging data, spectra can be extracted from the level 2 event file. To achieve this, source and background extraction regions are defined and the NuSTARDAS task `nuproducts` is run to extract a source spectrum, a background spectrum, an ancillary response function (ARF) and a redistribution matrix file (RMF). Source and background light curves are also produced.

TThe RMF file accounts for the discrete nature of the PI channels, describing how photons of a given energy will be redistributed into PI channels. The ARF file describes the spectral response (i.e., the effective area) as a function of photon energy (as a result of the optics, the detector efficiency, and additional factors). `nuproducts` produces the ARF by taking a CALDB ARF file and correcting for the effects of vignetting, the natural dither, and the detector gaps relevant for the given observation and source FoV position.

The overall response is the product of the ARF and RMF, which is used to translate between unfolded and folded spectra (i.e., the spectra before and after the effects of the telescope/instrumental response, respectively) when doing spectral modeling. For a given *NuSTAR* source, the spectra is extract for each available observation, with separate extractions for FPMA and FPMB, then, if more than one, the spectra needed to be are coadd across all observations (separately for FPMA and FPMB) using the task `addascaspec`.

The spectroscopic data are then fitted with physically motivated models using XSPEC to constrain the observed and intrinsic spectral properties of sources.

Bibliography

Antonucci R., 1993, Annual Review of Astronomy and Astrophysics, 31, 473

Antonucci R. R. J., Miller J. S., 1985, ApJ, 297, 621

Arnaud K. A., 1996, in Jacoby G. H., Barnes J., eds, Astronomical Society of the Pacific Conference Series Vol. 101, Astronomical Data Analysis Software and Systems V. p. 17

Arnaud K. A., et al., 1985, MNRAS, 217, 105

Avni Y., 1976, ApJ, 210, 642

B. Rybicki G., P. Lightman A., 1979, Radiative Processes in Astrophysics. Wiley

Ballantyne D. R., Ross R. R., Fabian A. C., 2001, MNRAS, 327, 10

Ballantyne D. R., et al., 2014, ApJ, 794, 62

Baloković M., et al., 2015, ApJ, 800, 62

Barthelmy S. D., et al., 2005, Space Science Reviews, 120, 143

Baumgartner W. H., Tueller J., Barthelmy S., Krimm H., Birsa F., Ryan L., 2001, in Inoue H., Kunieda H., eds, Astronomical Society of the Pacific Conference Series Vol. 251, New Century of X-ray Astronomy. p. 520

Beckmann V., Shrader C., 2013, Active Galactic Nuclei. Physics textbook, Wiley, `http://books.google.co.uk/books?id=QmwfxlZJM4sC`

Beloborodov A. M., 1999, in Poutanen J., Svensson R., eds, Astronomical Society of the Pacific Conference Series Vol. 161, High Energy Processes in Accreting Black Holes. p. 295 (`arXiv:astro-ph/9901108`)

Bentz M. C., Peterson B. M., Netzer H., Pogge R. W., Vestergaard M., 2009, ApJ, 697, 160

Bentz M. C., et al., 2010, ApJ, 716, 993

Bevington P. R., 1969, Data reduction and error analysis for the physical sciences

Bian W.-H., Zhao Y.-H., 2003a, PASJ, 55, 599

Bian W., Zhao Y., 2003b, MNRAS, 343, 164

Bianchi S., Matt G., Haardt F., Maraschi L., Nicastro F., Perola G. C., Petrucci P. O., Piro L., 2001, A&A, 376, 77

Bianchi S., Guainazzi M., Matt G., Fonseca Bonilla N., Ponti G., 2009, A&A, 495, 421

Bianchi S., de Angelis I., Matt G., La Parola V., de Rosa A., Grandi P., Jiménez Bailón E., Piconcelli E., 2010, A&A, 522, A64

Bianchi S., et al., 2012a, MNRAS, 426, 3225

Bianchi S., Maiolino R., Risaliti G., 2012b, Advances in Astronomy, 2012, 782030

Blackburn J. K., 1995, in Shaw R. A., Payne H. E., Hayes J. J. E., eds, Astronomical Society of the Pacific Conference Series Vol. 77, Astronomical Data Analysis Software and Systems IV. p. 367

Blandford R. D., McKee C. F., 1982, ApJ, 255, 419

Blandford R. D., Rees M. J., 1974, MNRAS, 169, 395

Boroson T. A., 2003, ApJ, 585, 647

Braito V., et al., 2007, ApJ, 670, 978

Brenneman L. W., et al., 2014, ApJ, 781, 83

Buisson D. J. K., Lohfink A. M., Alston W. N., Fabian A. C., 2017, MNRAS, 464, 3194

Burrows D. N., et al., 2005, Space Science Reviews, 120, 165

Caballero-Garcia M. D., Dovciak M., Papadakis I., Epitropakis A., Svoboda J., Kara E., Karas V., 2017, preprint, (arXiv:1701.03905)

Cappi M., et al., 2009, A&A, 504, 401

Carter J. A., Read A. M., 2007, A&A, 464, 1155

Cavaliere A., Morrison P., 1980, ApJ, 238, L63

Cirasuolo M., Magliocchetti M., Celotti A., Danese L., 2003, MNRAS, 341, 993

Clavel J., Wamsteker W., Glass I. S., 1989, ApJ, 337, 236

Crenshaw D. M., Kraemer S. B., 1999, ApJ, 521, 572

Dadina M., 2007, A&A, 461, 1209

Dauser T., Garcia J., Wilms J., Böck M., Brenneman L. W., Falanga M., Fukumura K., Reynolds C. S., 2013, MNRAS, 430, 1694

Dauser T., García J., Parker M. L., Fabian A. C., Wilms J., 2014, MNRAS, 444, L100

De Luca A., Molendi S., 2004, A&A, 419, 837

De Marco B., Ponti G., Cappi M., Dadina M., Uttley P., Cackett E. M., Fabian A. C., Miniutti G., 2013, MNRAS, 431, 2441

Den Herder J. W., et al., 2001, A&A, 365, L7

Done C., Gierliński M., Kubota A., 2007a, A&A Rev., 15, 1

Done C., Gierliński M., Sobolewska M., Schurch N., 2007b, in Ho L. C., Wang J.-W., eds, Astronomical Society of the Pacific Conference Series Vol. 373, The Central Engine of Active Galactic Nuclei. p. 121 (`arXiv:astro-ph/0703449`)

Dovciak M., Done C., 2015, in The Extremes of Black Hole Accretion. p. 26 (`arXiv:1507.05564`)

Dovčiak M., Done C., 2016, Astronomische Nachrichten, 337, 441

Eddington A. S., 1925, MNRAS, 85, 403

Elvis M., Maccacaro T., Wilson A. S., Ward M. J., Penston M. V., Fosbury R. A. E., Perola G. C., 1978, MNRAS, 183, 129

Elvis M., et al., 1994, ApJS, 95, 1

Emmanoulopoulos D., Papadakis I. E., Dovčiak M., McHardy I. M., 2014, MNRAS, 439, 3931

Fabian A. C., 1994, ApJS, 92, 555

Fabian A. C., Miniutti G., 2005, ArXiv Astrophysics e-prints,

Fabian A. C., Rees M. J., Stella L., White N. E., 1989, MNRAS, 238, 729

Fabian A. C., Iwasawa K., Reynolds C. S., Young A. J., 2000, PASP, 112, 1145

Fabian A. C., et al., 2002, MNRAS, 335, L1

Fabian A. C., et al., 2009, *Nature*, 459, 540

Fabian A. C., et al., 2012, MNRAS, 419, 116

Fabian A. C., Lohfink A., Kara E., Parker M. L., Vasudevan R., Reynolds C. S., 2015, MNRAS, 451, 4375

Fabian A. C., Lohfink A., Belmont R., Malzac J., Coppi P., 2017, MNRAS, 467, 2566

Fath E. A., 1909, Lick Observatory Bulletin, 5, 71

Ferland G. J., et al., 2013, Rev. Mexicana Astron. Astrofis., 49, 137

Filippenko A. V., Halpern J. P., 1984, ApJ, 285, 458

Gabriel C., et al., 2004, in Ochsenbein F., Allen M. G., Egret D., eds, Astronomical Society of the Pacific Conference Series Vol. 314, Astronomical Data Analysis Software and Systems (ADASS) XIII. p. 759

García J., Kallman T. R., 2010, ApJ, 718, 695

García J., Dauser T., Reynolds C. S., Kallman T. R., McClintock J. E., Wilms J., Eikmann W., 2013, ApJ, 768, 146

García J., et al., 2014, ApJ, 782, 76

Gehrels N., et al., 2004, ApJ, 611, 1005

Ghisellini G., 2013, Berlin Springer Verlag, 873

Ghisellini G., Haardt F., 1994, ApJ, 429, L53

Ghisellini G., Haardt F., Matt G., 1994, MNRAS, 267, 743

Giacconi R., Reidy W. P., Zehnpfennig T., Lindsay J. C., Muney W. S., 1965, ApJ, 142, 1274

Giacconi R., et al., 1979, ApJ, 230, 540

Gierliński M., Done C., 2004, MNRAS, 349, L7

Gliozzi M., Papadakis I. E., Eracleous M., Sambruna R. M., Ballantyne D. R., Braito V., Reeves J. N., 2009, ApJ, 703, 1021

González-Martín O., Vaughan S., 2012, A&A, 544, A80

Grandi P., Haardt F., Ghisellini G., Grove E. J., Maraschi L., Urry C. M., 1998, ApJ, 498, 220

Grier C. J., et al., 2012, ApJ, 744, L4

Guainazzi M., Bianchi S., de La Calle Pérez I., Dovčiak M., Longinotti A. L., 2011, A&A, 531, A131

Guilbert P. W., Rees M. J., 1988, MNRAS, 233, 475

Haardt F., Maraschi L., 1991, ApJ, 380, L51

Haardt F., Maraschi L., 1993, ApJ, 413, 507

Haardt F., Maraschi L., Ghisellini G., 1994, ApJ, 432, L95

Hailey C. J., et al., 2010, in Space Telescopes and Instrumentation 2010: Ultraviolet to Gamma Ray. p. 77320T, doi:10.1117/12.857654

Halpern J. P., 2006, The Astronomer's Telegram, 847

Harrison F. A., et al., 2010, in Space Telescopes and Instrumentation 2010: Ultraviolet to Gamma Ray. p. 77320S, doi:10.1117/12.858065

Harrison F. A., et al., 2013, ApJ, 770, 103

Heckman T. M., 1980, A&A, 87, 152

Henri G., Petrucci P. O., 1997, A&A, 326, 87

Hewett P. C., Foltz C. B., Chaffee F. H., 2001, AJ, 122, 518

Ho L. C., Filippenko A. V., Sargent W. L. W., 1994, in Courvoisier T., Blecha A., eds, IAU Symposium Vol. 159, Multi-Wavelength Continuum Emission of AGN. pp 275–278

Hönig S. F., Kishimoto M., 2010, A&A, 523, A27

Ishibashi W., Courvoisier T. J.-L., 2012, A&A, 540, L2

Ivezić Ž., et al., 2002, AJ, 124, 2364

Jones T. W., O'dell S. L., Stein W. A., 1974, ApJ, 188, 353

Kaastra J. S., Mewe R., Liedahl D. A., Komossa S., Brinkman A. C., 2000, A&A, 354, L83

Kalberla P. M. W., Burton W. B., Hartmann D., Arnal E. M., Bajaja E., Morras R., Pöppel W. G. L., 2005, A&A, 440, 775

Kara E., García J. A., Lohfink A., Fabian A. C., Reynolds C. S., Tombesi F., Wilkins D. R., 2017, MNRAS, 468, 3489

Keek L., Ballantyne D. R., 2016, MNRAS, 456, 2722

Khachikian E. Y., Weedman D. W., 1974, ApJ, 192, 581

Kotov O., Churazov E., Gilfanov M., 2001, MNRAS, 327, 799

Krongold Y., Nicastro F., Brickhouse N. S., Elvis M., Liedahl D. A., Mathur S., 2003, ApJ, 597, 832

La Franca F., et al., 2015, MNRAS, 449, 1526

Lanzuisi G., et al., 2016, A&A, 590, A77

Laor A., Behar E., 2008, MNRAS, 390, 847

Lawson A. J., Turner M. J. L., 1997, MNRAS, 288, 920

Liang E. P. T., 1979, ApJ, 231, L111

Lohfink A. M., et al., 2015, ApJ, 814, 24

Lohfink A. M., et al., 2016, ApJ, 821, 11

Lusso E., Risaliti G., 2017, preprint, (arXiv:1703.05299)

Lusso E., et al., 2010, A&A, 512, A34

Madsen K. K., et al., 2015, ApJS, 220, 8

Magdziarz P., Zdziarski A. A., 1995a, MNRAS, 273, 837

Magdziarz P., Zdziarski A. A., 1995b, MNRAS, 273, 837

Maiolino R., Marconi A., Salvati M., Risaliti G., Severgnini P., Oliva E., La Franca F., Vanzi L., 2001, A&A, 365, 28

Malizia A., et al., 2008, MNRAS, 389, 1360

Malizia A., Bassani L., Bazzano A., Bird A. J., Masetti N., Panessa F., Stephen J. B., Ubertini P., 2012, MNRAS, 426, 1750

Malizia A., Molina M., Bassani L., Stephen J. B., Bazzano A., Ubertini P., Bird A. J., 2014, ApJ, 782, L25

Malkan M. A., Sargent W. L. W., 1982, ApJ, 254, 22

Mantovani G., Nandra K., Ponti G., 2016, MNRAS, 458, 4198

Marconi A., Risaliti G., Gilli R., Hunt L. K., Maiolino R., Salvati M., 2004, MNRAS, 351, 169

Marinucci A., et al., 2014a, MNRAS, 440, 2347

Marinucci A., et al., 2014b, ApJ, 787, 83

Marinucci A., et al., 2015, MNRAS, 447, 160

Marinucci A., Tortosa A., NuSTAR AGN Physics Working Group 2016, Astronomische Nachrichten, 337, 490

Marti J., Mirabel I. F., Chaty S., Rodriguez L. F., 1998, A&A, 330, 72

Martocchia A., Matt G., 1996, MNRAS, 282, L53

Martocchia A., Karas V., Matt G., 2000, MNRAS, 312, 817

Martocchia A., Matt G., Karas V., 2002, A&A, 383, L23

Matt G., Perola G. C., Piro L., 1991, A&A, 247, 25

Matt G., Fabian A. C., Reynolds C. S., 1997, MNRAS, 289, 175

Matt G., Bianchi S., de Rosa A., Grandi P., Perola G. C., 2006, A&A, 445, 451

Matt G., et al., 2014, MNRAS, 439, 3016

Matt G., et al., 2015, MNRAS, 447, 3029

McHardy I. M., Papadakis I. E., Uttley P., Page M. J., Mason K. O., 2004, MNRAS, 348, 783

Miller L., Turner T. J., Reeves J. N., 2008, A&A, 483, 437

Miller J. M., et al., 2013, ApJ, 775, L45

Miller J. M., et al., 2015, ApJ, 799, L6

Miniutti G., Fabian A. C., 2004, MNRAS, 349, 1435

Miniutti G., et al., 2007, PASJ, 59, 315

Molina M., et al., 2009, MNRAS, 399, 1293

Molina M., Bassani L., Malizia A., Stephen J. B., Bird A. J., Bazzano A., Ubertini P., 2013, MNRAS, 433, 1687

Moran E. C., Barth A. J., Eracleous M., Kay L. E., 2007, ApJ, 668, L31

Moretti A., et al., 2005, in Siegmund O. H. W., ed., Proc. SPIEVol. 5898, UV, X-Ray, and Gamma-Ray Space Instrumentation for Astronomy XIV. pp 360–368, doi:10.1117/12.617164

Mukai K., Hellier C., Madejski G., Patterson J., Skillman D. R., 2003, ApJ, 597, 479

Murphy K. D., Yaqoob T., 2009, MNRAS, 397, 1549

Mushotzky R. F., Done C., Pounds K. A., 1993, Annual Review of Astronomy and Astrophysics, 31, 717

Nagar N. M., Oliva E., Marconi A., Maiolino R., 2002, A&A, 391, L21

Nandra K., Pounds K. A., 1994, MNRAS, 268, 405

Nandra K., George I. M., Mushotzky R. F., Turner T. J., Yaqoob T., 1997, ApJ, 476, 70

Nandra K., O'Neill P. M., George I. M., Reeves J. N., 2007, MNRAS, 382, 194

Nayakshin S., Kazanas D., Kallman T. R., 2000, in McConnell M. L., Ryan J. M., eds, American Institute of Physics Conference Series Vol. 510, American Institute of Physics Conference Series. pp 250–254, doi:10.1063/1.1303213

Nenkova M., Sirocky M. M., Nikutta R., Ivezić Ž., Elitzur M., 2008, ApJ, 685, 160

Netzer H., 2015, Annual Review of Astronomy and Astrophysics, 53, 365

Netzer H., Laor A., 1993, ApJ, 404, L51

Novikov I. D., Thorne K. S., 1973, in Dewitt C., Dewitt B. S., eds, Black Holes (Les Astres Occlus). pp 343–450

Oliva E., Origlia L., Maiolino R., Moorwood A. F. M., 1999, A&A, 350, 9

Onori F., et al., 2017, MNRAS, 468, L97

Padovani P., et al., 2017, A&A Rev., 25

Pancoast A., Brewer B. J., Treu T., Park D., Barth A. J., Bentz M. C., Woo J.-H., 2014, MNRAS, 445, 3073

Pancoast A., Brewer B. J., Treu T., Park D., Barth A. J., Bentz M. C., Woo J.-H., 2015, MNRAS, 448, 3070

Panessa F., et al., 2011, MNRAS, 417, 2426

Papadakis I. E., 2004, MNRAS, 348, 207

Papadakis I., 2011, in Ness J.-U., Ehle M., eds, The X-ray Universe 2011. p. 121

Papadakis I. E., Sobolewska M., Arevalo P., Markowitz A., McHardy I. M., Miller L., Reeves J. N., Turner T. J., 2009, A&A, 494, 905

Parker M. L., et al., 2014, MNRAS, 443, 1723

Pavlinsky M. N., Grebenev S. A., Sunyaev R. A., 1992, Soviet Astronomy Letters, 18, 88

Perola G. C., et al., 2000, A&A, 358, 117

Perola G. C., Matt G., Cappi M., Fiore F., Guainazzi M., Maraschi L., Petrucci P. O., Piro L., 2002, A&A, 389, 802

Peterson B. M., 1993, PASP, 105, 247

Peterson B. M., 1997, An Introduction to Active Galactic Nuclei

Peterson B. M., et al., 2004, ApJ, 613, 682

Petrucci P. O., Henri G., 1997, A&A, 326, 99

Petrucci P. O., et al., 2000, ApJ, 540, 131

Petrucci P. O., et al., 2001, ApJ, 556, 716

Piccinotti G., Mushotzky R. F., Boldt E. A., Holt S. S., Marshall F. E., Serlemitsos P. J., Shafer R. A., 1982, ApJ, 253, 485

Piconcelli E., Jimenez-Bailón E., Guainazzi M., Schartel N., Rodríguez-Pascual P. M., Santos-Lleó M., 2004, MNRAS, 351, 161

Piconcelli E., Jimenez-Bailón E., Guainazzi M., Schartel N., Rodríguez-Pascual P. M., Santos-Lleó M., 2005, A&A, 432, 15

Piro L., Matt G., Ricci R., 1997, A&A, 126

Ponti G., Papadakis I., Bianchi S., Guainazzi M., Matt G., Uttley P., Bonilla N. F., 2012, A&A, 542, A83

Porquet D., et al., 2017, preprint, (arXiv:1707.08907)

Pounds K., Reeves J., 2002, ArXiv Astrophysics e-prints,

Poutanen J., Svensson R., 1996a, ApJ, 470, 249

Poutanen J., Svensson R., 1996b, ApJ, 470, 249

Protassov R., van Dyk D. A., Connors A., Kashyap V. L., Siemiginowska A., 2002, ApJ, 571, 545

Reynolds C. S., 1996, PhD thesis, University of Cambridge

Reynolds C. S., 1997, MNRAS, 286, 513

Reynolds C. S., 2000, ApJ, 533, 811

Reynolds C. S., Nowak M. A., 2003, Phys. Rep., 377, 389

Ricci C., Ueda Y., Ichikawa K., Paltani S., Boissay R., Gandhi P., Stalevski M., Awaki H., 2014, A&A, 567, A142

Ricci F., La Franca F., Onori F., Bianchi S., 2017, A&A, 598, A51

Risaliti G., Nardini E., Salvati M., Elvis M., Fabbiano G., Maiolino R., Pietrini P., Torricelli-Ciamponi G., 2011, MNRAS, 410, 1027

Rivers E., et al., 2014, ApJ, 786, 126

Roming P. W. A., et al., 2005, Space Science Reviews, 120, 95

Sakano M., Koyama K., Murakami H., Maeda Y., Yamauchi S., 2002, ApJS, 138, 19

Sambruna R. M., et al., 2009, ApJ, 700, 1473

Sazonov S. Y., Revnivtsev M. G., Lutovinov A. A., Sunyaev R. A., Grebenev S. A., 2004, A&A, 421, L21

Schmidt M., 1963, *Nature*, 197, 1040

Seyfert C. K., 1943, ApJ, 97, 28

Shakura N. I., Sunyaev R. A., 1973, A&A, 24, 337

Shields G. A., 1978, *Nature*, 272, 706

Shuder J. M., Osterbrock D. E., 1981, ApJ, 250, 55

Sobolewska M. A., Papadakis I. E., 2009, MNRAS, 399, 1597

Soldi S., et al., 2014, A&A, 563, A57

Stern B. E., Poutanen J., Svensson R., Sikora M., Begelman M. C., 1995, ApJ, 449, L13

Strateva I. V., Brandt W. N., Schneider D. P., Vanden Berk D. G., Vignali C., 2005, AJ, 130, 387

Strüder L., et al., 2001, A&A, 365, L18

Svensson R., 1984, MNRAS, 209, 175

Takahashi T., et al., 2007, PASJ, 59, 35

Titarchuk L., 1994, ApJ, 434, 570

Tombesi F., Cappi M., Reeves J. N., Palumbo G. G. C., Yaqoob T., Braito V., Dadina M., 2010, A&A, 521, A57

Tombesi F., Cappi M., Reeves J. N., Nemmen R. S., Braito V., Gaspari M., Reynolds C. S., 2013, MNRAS, 430, 1102

Tortosa A., et al., 2017, MNRAS, 466, 4193

Tortosa A., Bianchi S., Marinucci A., Matt G., Petrucci P. O., 2018, preprint, (`arXiv:1801.04456`)

Trevese D., Perna M., Vagnetti F., Saturni F. G., Dadina M., 2014, ApJ, 795, 164

Turner M. J. L., et al., 2001, A&A, 365, L27

Ubertini P., et al., 2003, A&A, 411, L131

Urry C. M., Padovani P., 1995, PASP, 107, 803

Ursini F., et al., 2015, MNRAS, 452, 3266

Vagnetti F., Antonucci M., Trevese D., 2013, A&A, 550, A71

Vaughan S., Fabian A. C., Nandra K., 2003, MNRAS, 339, 1237

Veron P., Lindblad P. O., Zuiderwijk E. J., Veron M. P., Adam G., 1980, A&A, 87, 245

Vestergaard M., 2002, ApJ, 571, 733

Vestergaard M., Peterson B. M., 2006, ApJ, 641, 689

Walton D. J., et al., 2013, ApJ, 777, L23

Wang T., Mihara T., Otani C., Matsuoka M., Awaki H., 1999, ApJ, 515, 567

Wegner G., et al., 2003, AJ, 126, 2268

Weisskopf M. C., Tananbaum H. D., Van Speybroeck L. P., O'Dell S. L., 2000, in Truemper J. E., Aschenbach B., eds, Proc. SPIEVol. 4012, X-Ray Optics, Instruments, and Missions III. pp 2–16 (arXiv:astro-ph/0004127), doi:10.1117/12.391545

White R. L., et al., 2000, ApJS, 126, 133

Willmer C. N. A., Focardi P., Chan R., Pellegrini P. S., da Costa N. L., 1991, AJ, 101, 57

Winter L. M., Mushotzky R. F., Reynolds C. S., Tueller J., 2009, ApJ, 690, 1322

Winter L. M., Lewis K. T., Koss M., Veilleux S., Keeney B., Mushotzky R. F., 2010, ApJ, 710, 503

Woo J.-H., Urry C. M., 2002, ApJ, 579, 530

XMM Users Handbook 2010, XMM-Newton SOC website

Yamauchi M., Matsuoka M., Kawai N., Yoshida A., 1992, ApJ, 395, 453

Zdziarski A. A., Johnson W. N., Magdziarz P., 1996, MNRAS, 283, 193

Zhang L., Cheng K. S., 1997, ApJ, 488, 94

Zhang E.-P., Wang J.-M., 2006, ApJ, 653, 137

Zoghbi A., et al., 2015, ApJ, 799, L24

Życki P. T., 2004, MNRAS, 351, 1180

Życki P. T., Done C., Smith D. A., 1999, MNRAS, 309, 561

de La Calle Pérez I., et al., 2010, A&A, 524, A50

de Rosa A., et al., 2012, MNRAS, 420, 2087